

# DYNAMICS OF THE WEDDELL SEA BOUNDARY CURRENT SYSTEM (BCS) ON SEASONAL TIME-SCALES

(DYNAMIK DES WEDDELL MEER KÜSTENSTRÖMUNGEN SYSTEM AUF  
SAISONALEN ZEITSKALEN)

BY (VON)

NICOLAS LE PAIH

Supervised by: Prof. Dr. Torsten Kanzow, Dr. Olaf Boebel, Dr. Tore Hattermann

A Thesis submitted in partial fulfilment of the requirements for the degree of  
Doctor of natural sciences - Dr. rer. nat.  
(Dissertation zur Erlangung des akademischen Grades Doktor der Naturwissenschaften)  
(Fachbereich 1: Physik und Elektrotechnik)

Bremen University, March 2021

First reviewer: Prof. Dr. Torsten Kanzow  
Alfred Wegener Institut Helmholtz Centre  
for Polar and Marine Research  
and,  
Institute of Environmental Physics  
University of Bremen

Second reviewer: Prof. Dr. Monika Rhein  
Institute of Environmental Physics  
University of Bremen

Doctoral colloquium : 6<sup>th</sup> of July 2021

Rien n'est sérieux pour l'esprit, tout peut le devenir pour le coeur.

*Jean Rostand, 1959*

Nicolas Le Paih: *Dynamics of the Weddell Sea Boundary Current System (BCS) on seasonal time-scales*, Dynamik des Weddell Meer Küstenströmungen System auf saisonalen Zeitskalen, © March 2021



## ABSTRACT

---

The boundary current system in the Weddell Sea is composed of surface and gravity currents, which flow along the Antarctic margin's, south of the Atlantic basin. These currents are central for the meridional transfer of heat and biogeochemical properties between the Weddell Sea and the world ocean. They contribute to the transport of relatively warm water towards the Weddell Sea continental shelves, a major site where cold and dense shelf water forms, and the export of dense shelf water towards lower latitudes, feeding the lower branch of the meridional overturning circulation. Yet, the link between warm water inflow and export of dense shelf water still needs to be made on seasonal-time scales.

The goal of my PhD is to provide the first coherent description of the seasonal evolution of the boundary current system along the continental slope. Combining oceanographic data, I find a synchronised seasonality of the barotropic flow along the Weddell Sea's continental slope. The seasonal acceleration of the barotropic flow significantly contributes to the transport of dense shelf waters and correlates with the surface stress in the eastern side of the Weddell Sea. This finding suggests that the winds in the eastern Weddell Sea remotely contribute to the transport of dense shelf waters in the western Weddell Sea. However, the mechanisms controlling the relationship between the surface stress and the barotropic flow remains unclear.

Even though oceanographic data are generally insufficient to quantitatively compare the baroclinic variability along the continental slope, I observe a weakening of the baroclinic seasonality between the eastern and the western part of the continental slope. A conceptual model developed for this study supports an along-slope dampening of the baroclinic signals associated with (1) the presence of a density gradient between the dense shelf water on the south- and western continental shelves and the water masses on the continental slope and, (2) the widening of the continental slope between the eastern and southern Weddell Sea. The former implies the formation of eddies, which diffuses the seasonality along the continental shelf edge. The latter implies an along-slope decrease in flow strength, limiting the downstream advection of density

anomalies from the eastern Weddell Sea. In the end, my analysis suggests that the region in front of the Ronne/Larsen Ice shelves in the southern/western Weddell Sea is less sensitive to the downstream advection of seasonal anomalies from the eastern Weddell Sea than the region in front of the Filchner Ice shelf in the southeastern Weddell Sea. However, data overlapping in time need to be collected in front of the eastern and the south-western continental shelves to quantify the downstream propagation of the baroclinic signals and corroborate this result.

## LIST OF PUBLICATIONS

---

Le Pailh, N., Hattermann, T., Boebel, O., Kanzow, T., Lüpkes, C., Rohardt, G., et al. (2020). Coherent seasonal acceleration of the Weddell Sea boundary current system driven by upstream winds. *Journal of Geophysical Research: Oceans*, 125, e2020JC016316. <https://doi.org/10.1029/2020JC016316>



# CONTENTS

---

1	INTRODUCTION	1
1.1	The boundary currents in the Southern Ocean	1
1.2	The Weddell Sea boundary current system (BCS)	5
1.3	Scientific questions	8
2	METHODS	11
2.1	Historical dataset	11
2.2	Analysis of oceanographic data	13
2.2.1	Sections of hydrographic properties	14
2.2.2	Seasonal variations in temperature and speed	15
2.2.3	Seasonal variations in surface stress	17
2.2.4	Empirical orthogonal function analysis (EOF)	19
2.3	Two-layer cylindrical model	19
2.3.1	Basic assumptions	20
2.3.2	Strength and structure of the mean flow	22
2.3.3	Cross-slope density fluxes	23
2.3.4	Diagnose the modified Warm Deep Water layer's depth	24
3	BAROTROPIC AND BAROCLINIC VARIABILITY ALONG THE CONTINENTAL SLOPE	25
3.1	Along-slope changes in the BCS properties	25
3.1.1	Annual mean-state	25
3.1.2	Seasonal variability	28
3.2	Relation to the surface stress	32
3.3	Coherent seasonal acceleration of the barotropic flow along the continental slope	34
3.4	Correlation between the barotropic variability at the tip of the Antarctic Peninsula and the surface stress	35
3.5	Discussion	38
3.5.1	Annual mean shift in flow regime along-slope	38
3.5.2	Seasonal acceleration of the barotropic flow	39
3.5.3	Teleconnection between flow speed and eastern/north-eastern Weddell Sea winds	40

3.5.4	Baroclinic response to seasonal forcing	42
3.6	Summary	43
4	DRIVERS OF BAROCLINIC'S SEASONALITY ALONG THE CONTI- NENTAL SLOPE	45
4.1	Introduction	45
4.2	Hydrographic properties observed up- and downstream the dense shelf region	47
4.3	Two-layers cartesian model	49
4.3.1	General assumptions	49
4.3.2	Discretisation of the pycnocline slope	52
4.3.3	Parameterisation of the eddy fluxes	55
4.3.4	Prognostic equations for $h_1$ and $d_1$	57
4.3.5	Input parameters and boundary conditions	60
4.4	Model sensitivity	64
4.4.1	Sensitivity parameters	64
4.4.2	Set up reproducing the BCS properties	66
4.5	Mechanisms driving the pycnocline heights' seasonality	68
4.6	Discussion	71
4.6.1	Seasonal anomalies in pycnocline height along the conti- nental slope	71
4.6.2	Validity of the two-layer approximation	74
4.7	Summary	76
5	CONCLUSION AND OUTLOOK	79
A	APPENDIX	87
A.1	List of AWI moorings	87
A.2	Details on the optimal interpolation (OI)	89
A.3	Error associated with the vertical interpolation	90
A.4	Phase of the barotropic flow at KN	92
A.5	EOF analysis on the zonal stress	93
A.6	Two-month-lag-correlation between the barotropic flow and the surface stress	94
A.7	Off-shelf slope's sloping	95
A.8	From two-to three layers	96
	BIBLIOGRAPHY	97

## LIST OF FIGURES

---

Figure 1	Representation of the ocean circulation in the Southern Ocean. 2
Figure 2	Satellite images depicting eddies and meanders of the Gulf Stream and in the Antarctic Slope Current. 4
Figure 3	Map of the ocean circulation associated with the Weddell Sea boundary current system. 6
Figure 4	Fresh and dense shelf regime along the Weddell Sea's continental slope. 7
Figure 5	Spatial distribution of AWI moorings. 12
Figure 6	Spatial and seasonal distribution of ship, float and seal-borne CTD profiles. 13
Figure 7	Distribution of AWI moorings, CTD profiles at the three study sites. 14
Figure 8	T-S diagram of the data fed into the optimal interpolation. 14
Figure 9	Moored data available for seasonal analysis. 17
Figure 10	Schematic of the two-layer, semi-enclosed boundary current overturning model from Hattermann, 2018. 20
Figure 11	Map showing the surface stress field and the spatial distribution of the oceanographic data. 26
Figure 12	Climatologic sections of mean hydrographic properties and along-slope velocities at the three study sites. 27
Figure 13	Seasonal temperature estimated at three study sites along the 1000, 2000/2500, and 3000/3500 m isobaths. 29
Figure 14	Seasonal velocity estimated at three study sites along the 1000, 2000/2500, and 3000/3500 m isobaths. 31
Figure 15	Along-slope and seasonal variability in surface stress. 33
Figure 16	Comparison between the phase of the barotropic flow at the three study sites, the variability in sea-level anomalies and the variability in zonal surface stress. 35

- Figure 17 Zero-lag correlation between the monthly velocity observed between 2005 and 2015 at AP<sub>2500</sub> and the different components of surface stress. 36
- Figure 18 Zero-lag correlation between the deseasoned velocity observed between 2005 and 2015 at AP<sub>2500</sub> and the different components of surface stress. 41
- Figure 19 Potential density distribution at AP, KN and PM 48
- Figure 20 Along-slope velocities measured by moored current meters at the AP, KN and PM. 49
- Figure 21 2D schematic of the two-layer cartesian model used to simulate the pycnocline evolution (i.e. mWDW layer depth) along the continental slope between 30°E to the AP. 50
- Figure 22 Cross-section summarising the processes involved in the two-layer cartesian model's density transport. 51
- Figure 23 Representation of the model's pycnocline slope within the fresh shelf region. 53
- Figure 24 Representation of the model's pycnocline slope within the dense shelf region. 54
- Figure 25 Eddy fluxes across the BCS boundaries in the fresh shelf and dense shelf regions. 57
- Figure 26 Model forcings in the two-layer cartesian model. 61
- Figure 27 Sensitivity analysis of the relationship between  $\Delta h_1$ ,  $d_1$ ,  $Q^*$  and  $c_W^*$ .  $Q^* = Q_{tot}/\Delta\rho$  is the dense water formation rate.  $c_W^* = c_W g \Delta\rho / (fW_h \rho_0)$  is the eddy growth rate at the CS/BCS boundary. 66
- Figure 28 Sensitivity analysis on the along-slope change in pycnocline height for experiments representative of the along-slope shift in density regime. 67
- Figure 29 Fraction of the along-slope change in pycnocline height associated with the export of dense water from the CS to the BCS. 69
- Figure 30 Hovmüller diagrams illustrating the pycnocline height's seasonal anomalies within the BCS. 70
- Figure 31 Across-isobath distribution of the seasonal variability in pycnocline depth based on individual CTD profiles. 73

Figure 32	Map summarising the main findings	82
Figure 33	Comparison between four schemes of vertical interpolation used to estimate the error on the depth-averaged flow strength.	91
Figure 34	Phase of the barotropic flow (ubt) estimated over the 2500 isobath at Kapp Norvegia for different years from different mooring arrays.	92
Figure 35	Comparison between the phase of the barotropic flow (ubt) estimated along the 2000-2500 m isobath and the two first modes of zonal stress.	93
Figure 36	Two-months lag correlation between the monthly velocity observed between 2005 and 2015 at AP <sub>2500</sub> and the different components of surface stress.	94
Figure 37	Schematic of the off-shelf-slope's sloping for an ocean at rest and for an ocean with coastal downwelling	95
Figure 38	Schematic representing the water ocean stratification (left panels) and the processes controlling the cross-slope density transfer (right panels) in a theoretical, two-layer and three-layer world.	96

## LIST OF TABLES

---

Table 1	Model constants, parameters and variables	63
Table 2	AWI moorings deployed in the Weddell Sea between 1987 and 2017.	88



## ACRONYMS

---

ACoC	Antarctic Cosastal Current
ASC	Antarctic Slope Current
DML	Dronning Maud Land
FRIS	Filchner-Ronne Ice Shelf
LIS	Larsen Ice Shelf
PM	Prime Meridian
KN	Kapp Norvegia
AP	Tip of the Antarctic Peninsula
CDW	Circumpolar Deep Water
mWDW	modified Warm Deep Water
WSDW	Weddell Sea Deep Water
WSBW	Weddell Sea Bottom Water
AABW	Antarctic Bottom Water
HSSW	High Salinity Shelf Water
CTD	Conductivity, temperature and pressure sensor
FESOM	Finite-Element/volumE Sea ice-Ocean Model
$\tau_w$	Surface stress weighted as a function of the wind-speed
$\tau_{wic}$	Surface stress weighted as a function the wind-speed and the sea-ice concentration
$\tau_{wicv}$	Surface stress weighted as a function the wind-speed, the sea-ice concentration and the sea-ice velocity
$\tau_{model}$	Surface stress obtained from FESOM output
EOF	Empirical Orthogonal Function Analysis
PPV	Planetary Potential Vorticity
SLA	Sea-level anomaly
BCS	WeddellSea's Boundary current system
CS	Wide continental shelves in the south-western Weddell Sea, including FRIS and LIS
IG	Interior Gyre



## INTRODUCTION

---

### 1.1 THE BOUNDARY CURRENTS IN THE SOUTHERN OCEAN

Ocean boundary currents control the exchange of water properties between the open ocean and the coastal seas. They play a large role in redistributing heat, carbon and nutrients in the global ocean (Todd et al., 2019). These currents split into two categories: eastern and western boundary currents (EBCs and WBCs, respectively). EBCs and WBCs are surface currents, which flow along the eastern and western margins of the oceans, respectively. They result from the wind-driven circulation (Munk, 1950; Stommel, 1948), which is anti-cyclonic over the subtropical gyres and cyclonic over subpolar gyres. In the subtropics, EBCs are wide, shallow and relatively slow currents, which transport cold water towards the equator at the eastern margin of the oceans (Hartmann, 2016). WBCs are narrow, deep-reaching and energetic currents, which transport warm waters towards the poles at the western margin of the oceans (Hogg and Johns, 1995). In the subpolar regions, the ocean circulation is reversed because easterly winds prevail at high-latitudes. In turn, EBCs transports cold waters towards the poles while WBCs transport warm waters towards the lower latitudes (Talley et al., 2011). Also, the difference in density between surface and bottom waters is weak compared to the subtropics. As a result, the subpolar boundary currents extend further down in the water column, transporting water masses at depth and occasionally interacting with the density-driven circulation at the bottom (Brink and Lentz, 2010a,b).

The Southern Ocean is the only ocean, which lacks a meridional boundary, i.e. is zonally unrestricted. It surrounds the Antarctic continent and regulates the meridional exchange of water between the Atlantic, Pacific Ocean and Indian Oceans (Lumpkin and Speer, 2007). Along with diapycnal mixing, the westerly winds that continuously blow around Antarctica drive the upwelling branch of the world-ocean (meridional) circulation (Lumpkin and Speer, 2007; Marshall and Speer, 2012). This meridional overturning circula-

tion (MOC), splits into two overturning cells. The upper cell consists of the ventilation of the North Atlantic Deep Water, mostly formed in the Nordic Seas and the Labrador Sea (Lumpkin and Speer, 2007; Orsi et al., 1995). This thesis focuses on the lower cell, which consists of the transformation of relatively light circumpolar deep water (CDW) into dense Antarctic Bottom Water (AABW) through air-sea fluxes. Significant densification occurs on the Weddell Sea’s and Ross Sea’s continental shelves (Fig. 1) through atmospheric heat loss and brine rejection (Fahrbach et al., 2011; Gill, 1973; Jacobs et al., 1970a; Nicholls et al., 2009). The katabatic winds, which steadily push the ice off-

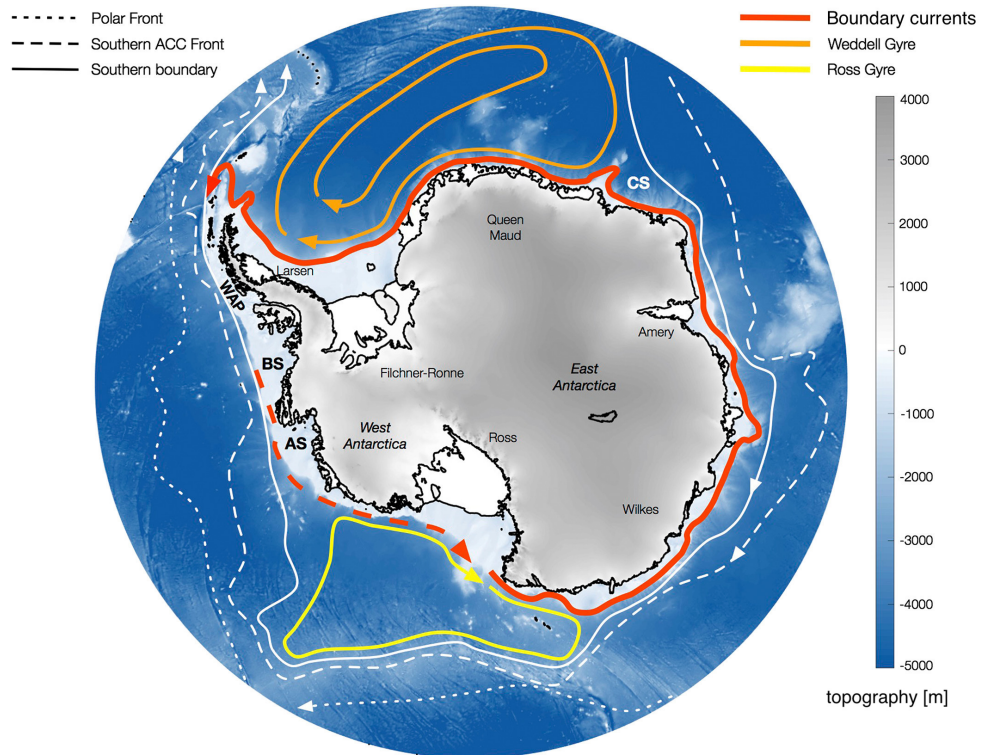


Figure 1: Representation of the ocean circulation in the Southern Ocean given in Thompson et al. (2018). The circulation associated with the Antarctic Circumpolar Current (ACC) is in white. The circulation associated with the boundary currents is in red. The dashed line represents the uncertainty on the extension of the boundary currents. The Weddell and Ross gyre are in orange and yellow, respectively. Western Antarctic Peninsula, WAP. Bellingshausen Sea, BS. Amundsen Seas, AS. Cosmonauts Sea, CS

shore, create quasi-permanent polynyas through which the ocean loses heat to the atmosphere (Holland, 2013; Tamura et al., 2016; Timmermann and Hellmer, 2013). Thereby, a thin layer of water crystallizes into sea-ice, rejecting salt/brine into the ocean surface layer, and creating a deep convection cell where the newly formed salt-enriched surface water, so called High Salinity Shelf Water (HSSW), sinks whereas deeper water gains relative buoyancy and rises to

the surface. The formation of HSSW determines both the circulation in the ice-shelf cavities and on the continental slope (Nicholls et al., 2009; Thompson et al., 2018). The sinking of HSSW, which has a temperature close to the near-surface freezing point can cause the melting of the ice-shelf base under increased pressure (Foldvik et al., 2004; Huhn et al., 2018; Jacobs et al., 1970b; Nicholls et al., 2009), resulting in an outflow of relatively colder and fresher Ice Shelf Water (ISW) from the ice-shelf cavities. Following the bathymetry, ISW and HSSW cascade down the continental slope and mix up with the ambient CDW to produce AABW (Gordon et al., 2009; Huhn et al., 2008a; Orsi et al., 1999). AABW is then exported towards the Atlantic, Pacific and Indian Ocean (Carmack and Foster, 1975), contributing to the meridional exchange of heat, freshwater and other biochemical properties, such as anthropogenic (human-induced) carbon, between the atmosphere and the abyss of the ocean (Carmack and Foster, 1975; Huhn et al., 2013; Meredith et al., 2000; Orsi et al., 1999; Vernet et al., 2019).

Due to the lack of western boundaries, the boundary currents in the Southern Ocean are almost circumpolar features (Thompson et al., 2018; Whitworth T. et al., 1985). They flow westward around the Antarctic continent from the Bellingshausen and Amundsen Seas (BS and AS) to the tip of the Antarctic Peninsula (AP) (Fig. 1), where a significant part of AABW is exported towards lower latitudes (Castagno et al., 2019; Fahrback et al., 1992; Meijers et al., 2016; Naveira Garabato et al., 2002). Flowing along Antarctica's margin, they control the global exchange of heat between the deep ocean and the continental shelves (Hellmer et al., 2012; Nicholls et al., 2009; Ryan et al., 2016; Årthun et al., 2012). Much like the WBCs, the Southern Ocean boundary currents are meandering and turbulent flows (Fig. 2), which shed eddies of different sizes. These eddies control the exchange of water masses across the continental slope, reducing the density difference between the regions on either side of the current. The stratification and the Coriolis force, which vary as a function of the latitude, determines the Rossby radius of deformation. In turn, they determine the size of the eddies and meanders by governing the scale of the baroclinic instability (Cushman-Roisin and Jean-Marie, 2011; Foster and Carmack, 1976; Gill, 1973; Orlanski and Cox, 1973). In subtropical gyres, the scale of the baroclinic instability ranges between 50 and 100 km. At higher latitudes, in the Southern Ocean, the temperature difference between sea-surface and

the bottom is small, i.e. the stratification is weak, reducing the size of the meanders from few kilometres on the continental shelves around Antarctica to  $O(10\text{ km})$  offshore of the continental slope (Thompson et al., 2018). Additionally, the cross-slope mixing of water masses occurs through diapycnal mixing associated with tides, internal waves, shear instability and sea-air interactions (Churchill et al., 1993; Gregg et al., 2018; Heywood et al., 2012).

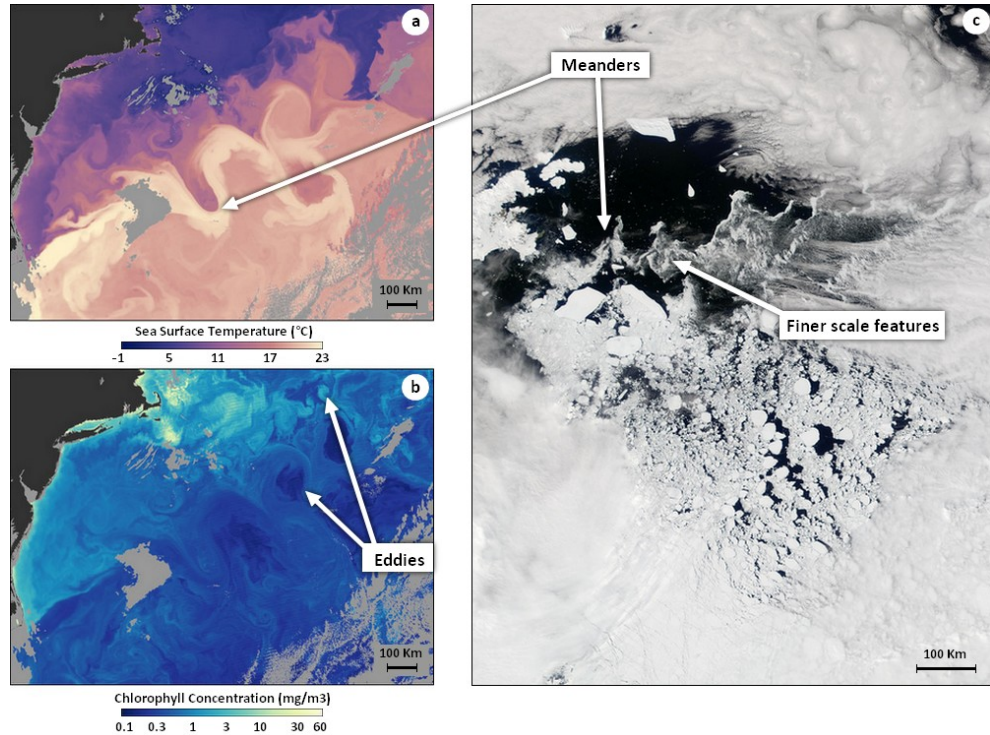


Figure 2: Satellite images depicting eddies and meanders of the Gulf Stream (Northwestern Sargasso Sea) and in the Antarctic Slope Current (near the tip of the Antarctic Peninsula). Panels a and b show the sea surface temperature and the chlorophyll concentration in the Northwestern Sargasso Sea. Panel c shows a picture of sea ice (white) and clouds (light grey) at the tip of the Antarctic Peninsula. Clouds linger in the periphery of the image. Images were obtained from the <https://earthobservatory.nasa.gov> website.

It is crucial to understand the cross-slope exchange between the deep ocean and the continental shelves to assess Antarctica's ice shelves melt rates and predict the possible change in the global heat, freshwater and biogeochemical cycles associated with the MOC (Church et al., 2013; Hellmer et al., 2012; Rignot et al., 2011; Thompson et al., 2018; Whitworth T. et al., 1985). Nevertheless, observing the cross-slope exchange of water masses is challenging as much of the area is covered by sea-ice most of the year and hard to access by ship (Eayrs et al., 2019a; Kottmeier et al., 2003). Also, the scale of variability is small compared to the data resolution. Yet, extensive efforts have been made

to gather data under the ice. In the Weddell Sea, data has been collected by oceanographic moorings for the past two decades. Under-ice tracking of Argo floats, and the tagging of seals allow now to gather data in front of the continental shelves (Klatt et al., 2007; Reeve et al., 2016; Reeve et al., 2019; Treasure et al., 2017). The challenge at hand is now to combine these data to gain more insights on the dynamics of the coastal flow and to identify the regions where future monitoring of cross-slope exchanges should best occur.

## 1.2 THE WEDDELL SEA BOUNDARY CURRENT SYSTEM (BCS)

*(Section adapted from Le Pailh et al., 2020)*

The boundary current system (BCS) in the Weddell Sea is composed of the Antarctic Coastal Current (ACoC), the Antarctic Slope Current (ASC) and the dense water outflow confined along the Antarctic Peninsula eastern's shelf break (Fig. 3). The ACoC and the ASC follow the ice shelf edge and the continental shelf break, respectively. They transport a mix of water masses originating from the continental shelves and the open ocean. The former are the fresh waters formed on the narrow continental shelf offshore the Dronning Maud Land (DML at 0°E) and the dense shelf waters formed offshore the Filchner Ronne Ice Shelf (FRIS at 50°W) and the Larsen Ice Shelf (LIS at 60°W). The latter are mainly the Circumpolar Deep Water (CDW) emerging from the upwelling branch of the global overturning circulation. CDW enters the Weddell gyre around 30°E via the Southern Indian Ridge. The ridge deflects the Antarctic Circumpolar Current southward and generates a residual circulation, which supplies the Weddell Sea with relatively warm, salty waters (Leach et al., 2011; Park et al., 2001; Ryan et al., 2016). Once embedded within the boundary currents, the shelf and open ocean waters are transported westward, mix between each other, and gradually transform into modified Warm Deep Water (mWDW), Weddell Sea Deep Water (WSDW) and Weddell Sea Bottom Water (WSBW) (Gill, 1973; Huhn et al., 2008a; Orsi et al., 1999), the latter being a precursor of AABW. Upstream of the dense water formation regions, the BCS can be approximated as a two-layer system, with the pycnocline sloping down towards the coast (Heywood et al., 1998; Riboni and Fahrback, 2009). Farther downstream, the pycnocline forms a v-shaped front across the continental shelf break and the BCS shifts from a two-layer to a three-layer

system due to the downslope cascade of WSBW as its bottom layer (Gill, 1973; Thompson and Heywood, 2008). This along-slope change in density regimes, i.e. the shifting from fresh shelf to a dense shelf (Thompson et al., 2018, Fig. 4), determines the structure of the baroclinic flow and the strength of the dense water outflow at the tip of the Antarctic Peninsula (AP), which contributes to the lower cell of the global overturning circulation (Jullion et al., 2014).

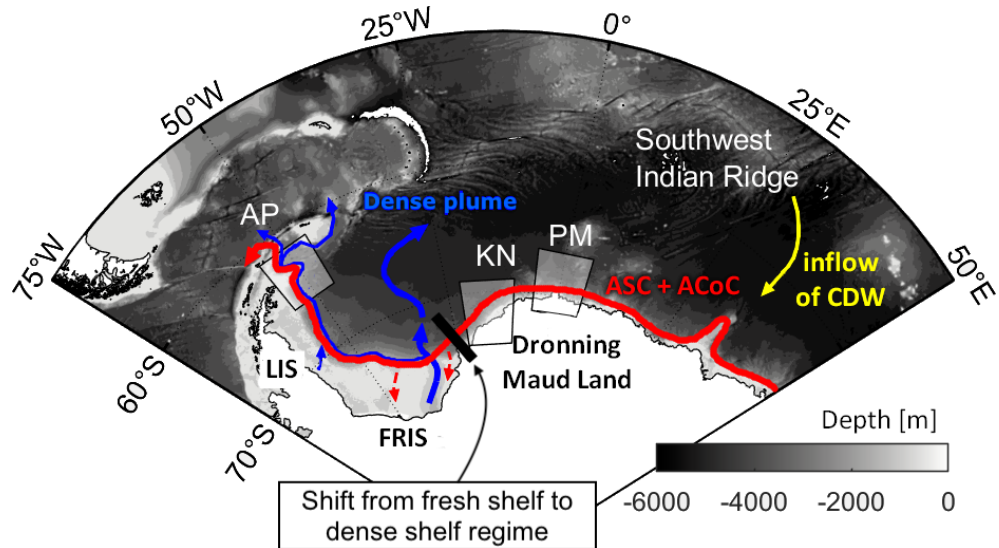


Figure 3: Map of the ocean circulation associated with the Weddell Sea boundary current system based on Ryan 2017 and Thompson et al. 2018. The following locations and currents are indicated: Tip of the Antarctic Peninsula (AP), Kapp Norvegia (KN), Prime Meridian (PM), Antarctic Slope Current (ASC) and Antarctic Coastal Current (ACoC). The Antarctic Circumpolar Current's branch of the gyre circulation has been omitted for reasons of clarity.

The export of shelf waters from the Weddell Sea and the inflow of mWDW onto the southern Weddell Sea continental shelf are governed by the seasonal changes of the BCS strength and structure (Meijers et al., 2016; Ryan et al., 2017; Årthun et al., 2012). Earlier studies have investigated, independently of each other, the seasonality of the BCS upstream and downstream of the dense water formation regions in the Weddell Sea (see regions in Fig. 3). Analyses of moored current meters at the Prime Meridian (PM) (Riboni and Fahrbach, 2009) and Kapp Norvegia (KN) (Graham et al., 2013) have revealed a maximum (minimum) depth-averaged flow strength in autumn (early summer). At both sites, the variability was associated with the seasonal cycle of local winds and modulated both by the sea-ice concentration and the thermohaline properties of surface waters. The along-slope component of the surface stress acting on the ocean surface either by the wind or the sea-ice, controls the on-

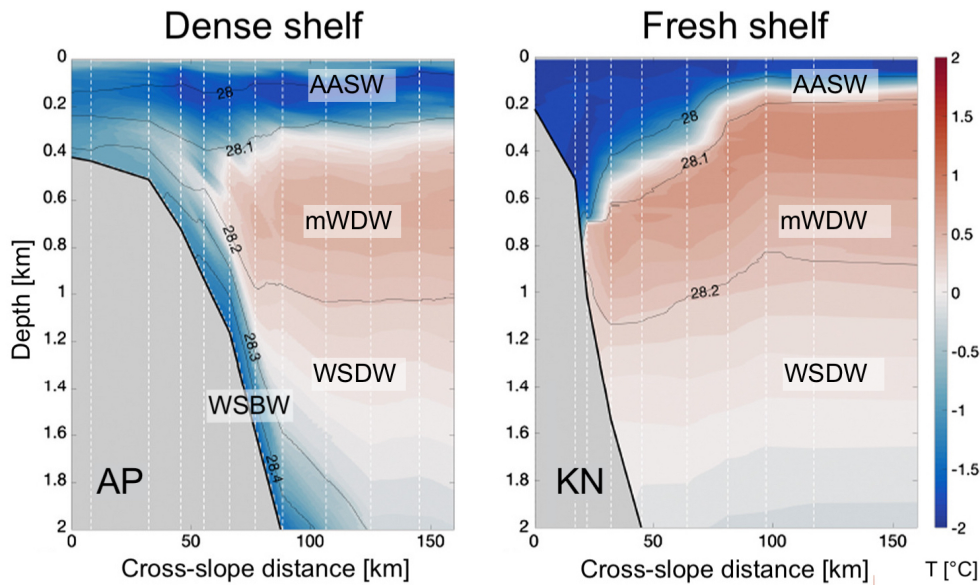


Figure 4: Cross-slope sections of conservative temperature (colors) and neutral density (black contours) at tip of the Antarctic Peninsula (AP) and Kapp Norvegia (KN), representing the dense and fresh shelf regime, respectively (Fig. adapted from Thompson et al., 2018). Section locations are shown in Figure 3. The following water masses are indicated: Antarctic Surface Water (AASW), modified Warm Deep Water (mWDW), Weddell Sea Deep Water (WSDW) and Weddell Sea Bottom Water (WSBW).

shore convergence of water masses via Ekman transport while the variability in surface water properties controls the stratification. The combination of both processes determines the cross-slope surface elevation and the density gradient across the continental slope, setting the strength of the barotropic current and the baroclinic structure of the flow (Hattermann, 2018; Nøst et al., 2011). The downstream advection of density anomalies also contributes to the baroclinic structure of the flow (Graham et al., 2013). Fahrbach et al. (2001) and Gordon et al. (2010) separately focused on the seasonal cycle of dense water outflow at AP, using one-year-long time series. A synthesis of both studies reveals a maximum (minimum) transport in early winter (summer) associated with a cold pulse of dense waters in autumn and a warm one in spring. Gordon et al. (2010) argued that these seasonal fluctuations could be related to the summer release of shelf waters formed on the western margin due to the weakening of the along-slope wind. However, this mechanism cannot be confirmed on seasonal time-scales (Darelius et al., 2014). Daae et al. (2018) highlighted the correlation between the variability in surface stress and the variability in Filchner Trough overflow on shorter time-scales. They argue that the outflow of dense water in front of FRIS is partly controlled by the circulation associ-

ated with the along-slope winds. Yet, a coherent understanding of the seasonal variability along the continental slope and specifically, in front of the western continental shelves, is missing.

### 1.3 SCIENTIFIC QUESTIONS

Understanding the seasonality of the BCS along the Weddell Sea continental slope is critical for predicting the heat transport toward the ice shelf cavities (Hellmer et al., 2012, 2017), the rate of dense water formation (Nicholls et al., 2009; Thompson et al., 2018) and the contribution of the Weddell Sea to the meridional overturning circulation (Meijers et al., 2016). Even though the local surface stress is believed to be the primary driver of variability, a coherent synoptic view of the flow structure, its evolution along the continental slope and connection to the large scale forcing has been lacking. In addressing this issue, this thesis aims to provide a coherent description of the barotropic and baroclinic seasonality of the BCS along and across the continental slope (from PM to AP, i.e. near the dense water's export region, Fig. 3), using both in situ data and numerical modelling. Specifically, the two following questions will be addressed.

**Research question 1:** How does the along-slope shift in density regime affect the seasonal variability in temperature and velocity along the continental slope? How do the seasonal variations in temperature and velocity relate to the variability in the large-scale wind-field?

**Research question 2:** What drives the baroclinic variability along the continental slope on seasonal time-scales ?

Research 1 is addressed, using more than twenty years of in situ observations collected upstream and downstream of the dense water formation region, namely at PM/KN and at AP. A model is used to address Research question 2 because in situ data are lacking on/in front of the western continental shelves (specifically between FRIS and LIS, Fig. 3). Chapter 2 presents the methods, including a description of the dataset used for this thesis. Chapter 3 provides a coherent analysis of the existing data collected at the three study locations along the continental slope (accepted in JGR-O, Le Paih et al., 2020). Chap-

ter 4 investigates the annual-mean and seasonal change in pycnocline height along the continental slope, including a presentation of the two-layers cartesian model developed to estimate the flux of density between the interior gyre, the BCS and the continental shelves in the dense shelf region (from  $30^{\circ}W$  to AP, Fig. 3). The conclusions and outlook are finally given in Chapter 5.



## METHODS

---

Dynamics such as deep convection, diapycnal mixing, wave propagation, eddy instability and tides are critical to understanding the ocean circulation in the Weddell Sea. However, the area is difficult to access all year-long due to the presence of sea-ice and winter data are sparse. This thesis combines data with conceptual models to provide an annual-mean and seasonal description of the boundary current system, with a focus on its large-scale variability. This Chapter presents the historical dataset used to describe the oceanic variability in Section 2.1, the methods used to analyse the oceanographic data and to estimate the surface stress in Section 2.2 and the model used by Hattermann (2018) to investigate seasonal variability in density along the continental slope of the eastern Weddell Sea in Section 2.3. The model formulation is modified in Chapter 4 to investigate the change in density along the southern-western Weddell Sea’s continental slope.

### 2.1 HISTORICAL DATASET

A total of sixteen moorings had been deployed and recovered on the continental shelf break between 1987 and 2017 at three locations: the Prime Meridian (PM), Kapp Norvegia (KN) and the tip of the Antarctic Peninsula (AP) (Fig. 5). The data are irregularly distributed in time and space. Indeed, the deployment plans varied from one cruise to another depending on climate conditions and scientific interests. Mooring locations featuring cumulative velocity record longer than a year and at three different depths (including surface and bottom measurements) are selected for seasonal analysis<sup>1</sup>. At the Prime Meridian, two positions matched these requirements<sup>2</sup> (PM<sub>2000</sub> and PM<sub>3500</sub>), three at Kap Norvegia (KN<sub>1000</sub>, KN<sub>2500</sub> and KN<sub>3000</sub>) and three at the tip of the Antarc-

<sup>1</sup> AWI206, AWI207, AWI216, AWI233, AWI232, AWI211, AWI212 and AWI226 (Table 2, Appendix A.1)

<sup>2</sup> Nomenclature of mooring locations: XX<sub>DDDD</sub>: with XX either PM (Prime Meridian), KN (Kapp Norvegia) or AP (Antarctic Peninsula) and DDDD indicating the nominal isobath depth at which the mooring was moored.

tic Peninsula ( $AP_{1000}$ ,  $AP_{2500}$  and  $AP_{3500}$ ). Four of these ( $PM_{2000}$ ,  $PM_{3500}$ ,  $AP_{1000}$  and  $AP_{2500}$ ) featured velocity time series longer than four years at all depths.  $PM_{2000}$  and  $AP_{2500}$  are the only positions overlapping in time along-slope, the overlap existing between 2005 and 2010 at three depths below the thermocline. At Kapp Norvegia, most of the instruments were deployed between 1990 and 1992 only, which is not enough to filter out the sub-seasonal and interannual variability. To overcome this, a mooring array deployed between 2009 and 2010 (Heywood et al., 2012), 350 km downstream of the AWI array, is used to assess the robustness of the results.

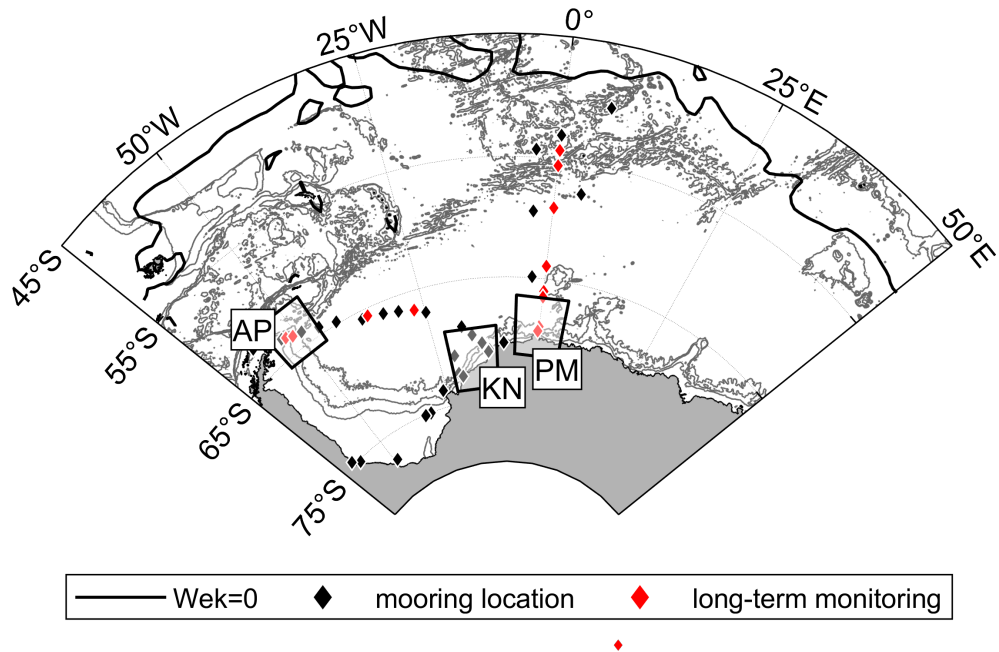


Figure 5: Spatial distribution of AWI moorings (black rhombs). Positions with velocity records longer than three years at three different depths are marked red (long-term monitoring). The black line near the map’s northern boundary shows the position where annual-mean Ekman pumping vanishes. This position is used as a proxy to define the northern limit of the Weddell Sea.

In addition to the mooring data, a large amount of ship-based CTD data, Argo float data and seal data are also included in this study<sup>3</sup> (Fig. 6). The spatial resolution varies for each method. Ship-borne CTD profiles describe the hydrographic properties down to the seafloor but at a spatial coverage confined to the ship tracks. The maximum depth of profiles from Argo floats limits to 2000 m depth, yet the spatial coverage is more extensive than the ship’s CTDs. Seals tagging allows to gather data on the continental shelves, but the quality

<sup>3</sup> The seal-borne CTD profiles shown on Figure 6 are not exclusive to AWI cruises. Also, ship-borne CTD profiles conducted by the Norwegian Polar Institute cruises are added to the dataset at Kapp Norvegia.

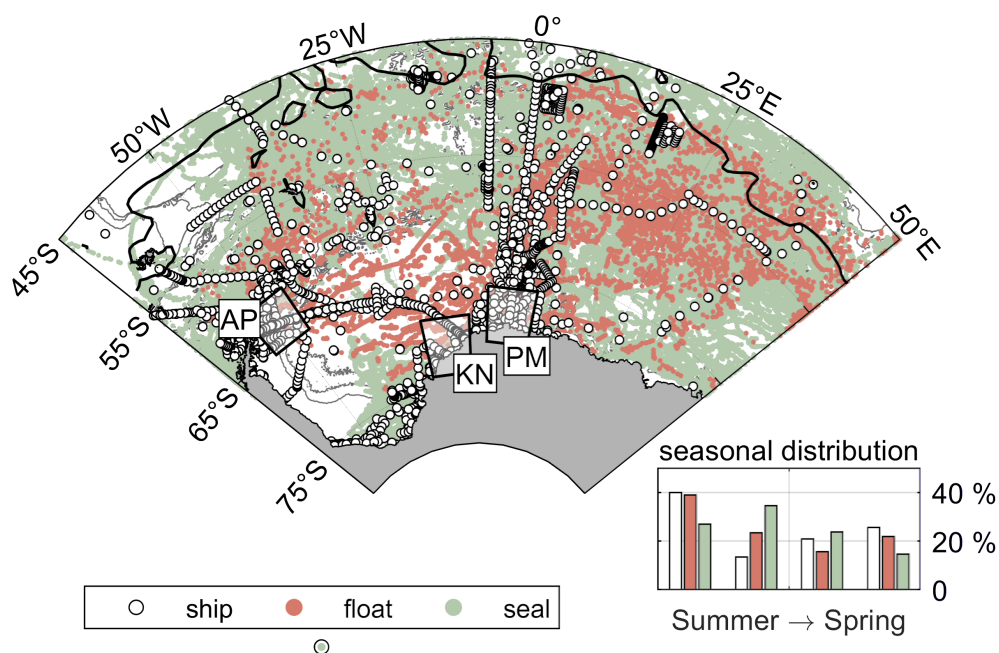


Figure 6: Spatial and seasonal distribution of ship, float and seal-borne CTD profiles. The dark line defines the northern limit of the Weddell Sea where the annual-mean Ekman pumping vanishes.

of the data is limited, especially for the salinity. The seasonal distribution of the data is also characteristic of each method. Research ice breaker can only access areas with sea-ice thicknesses  $< 3\text{m}$  (without having to ram) rendering ship-borne CTD profiles almost nonexistent on the continental shelf break in winter. Argo floats are capable of measuring data points below the sea-ice, but they need ice-free zones to surface and relay their data. Data transmission might be incomplete when the float fails to surface long enough or when its battery fails before reaching an ice-free zone, explaining the decrease in data points over the year (lower left panel, Fig. 6). This decrease in data points is also true for seal-borne CTD profiles because the lifetime of a tagged sensor is limited to a year. Even though a large data gap remains in the western Weddell Sea (map, Fig. 6), combining the different methods aids to understand the temporal and spatial variability along the Weddell Sea's continental slope. Thus, ship-, Argo- and seal-borne CTD profiles are selected in the vicinity of the mooring array to complete the dataset at the three study locations (Fig. 7).

## 2.2 ANALYSIS OF OCEANOGRAPHIC DATA

(Section adapted from Le paih et al. 2020)

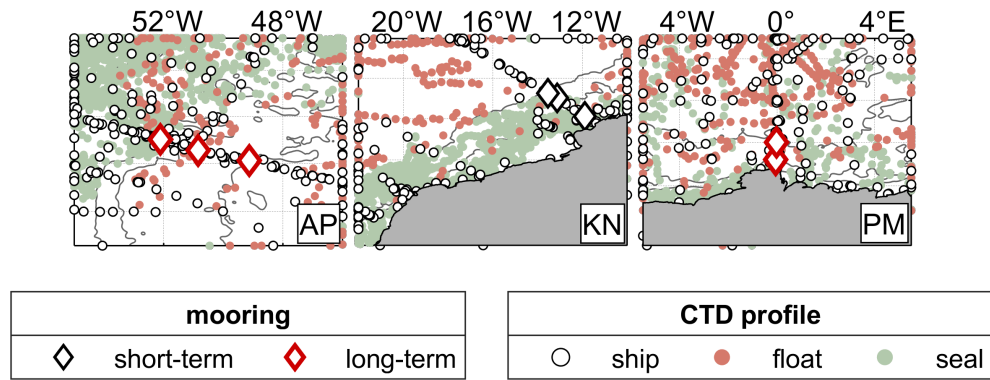


Figure 7: Distribution of AWI moorings (rhombs), ship (open circles), float (red dots) and seal-borne (green dots) CTD profiles at the three study sites: the tip of the Antarctic Peninsula (AP), Kapp Norvegia (KN) and the Prime Meridian (PM).

### 2.2.1 Sections of hydrographic properties

The ship-based CTD data available for the cross-slope transects of PM, KN and AP, is combined with all available ARGO and seal-borne CTD profiles located within the vicinity of each cross-section (Argo, 2017; Driemel et al., 2017; Treasure et al., 2017). Optimal interpolation (OI) is applied to temperature and salinity of the collected datasets in the planetary potential vorticity (PPV= $f/h$ ) versus depth ( $Z$ ) space (the data points used for the OI are given in Figure 8).

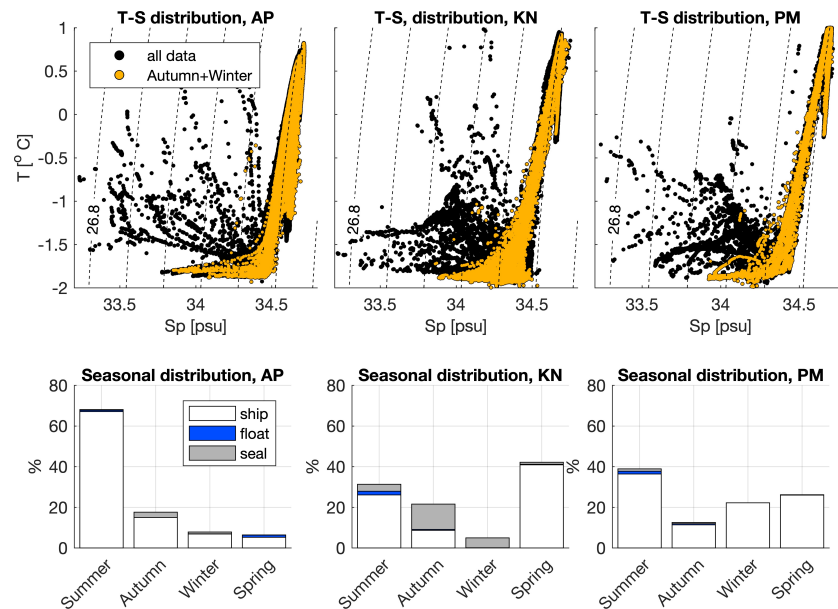


Figure 8: T-S diagram of the data fed into the optimal interpolation (OI) at PM, KN and AP. The seasonal distribution of the data observed above 1000 m depth and used for the OI is indicated below the T-S diagrams.

This technique is normally used to produce accurate maps of temperature and salinity from sparse, irregularly sampled data of different accuracy, assuming a given expression of the spatial autocorrelation function (Böhme and Send, 2005; Gandin, 1965; Reeve et al., 2016). Applying the method in the PPV-Z space ensures an optimal remapping of the data in the cross-shelf direction, for a particular transect. CTD-profiles are weighted equally as a function of time to include enough data. Inclusion of all available profiles results in a summer bias of the interpolation when data is sparse in winter. This bias is discussed in Section 3.1.1. We assume the observed water-mass to be advected from the transect to its observed position (or vice versa) by a geostrophically balanced flow that follows isopleths of PPV. Thus, the data is weighted equally along the PPV contour. In the Weddell Sea, along-slope diabatic changes can only be neglected locally (Reeve et al., 2016). Assuming a typical barotropic flow of  $10 \text{ cm s}^{-1}$  and diabatic changes occurring at the seasonal time scale ( $\tau = 80$  days), we considered all data within 350 km of each transect to be valid. Temperature and salinity sections are first estimated in PPV-depth space at each location. Since the vertical resolution of the ship-based profiles is too high to assimilate all the data at once, the dataset is split into sub-datasets corresponding to subdomains. The sub-datasets are selected within constant vertical depth-layers at PM and KN and terrain-following depth-layers at the tip of the AP, considering a vertically stratified ocean. While the former coordinates provided better results in the vicinity of the thermocline depth, the latter proved to be more performant in mapping the dense bottom layer at AP. Finally, PPV-depth estimates are remapped on to cross-slope Distance-Z space to calculate the geostrophic velocities (sections given in Figure 11). These velocities are defined as the depth-integral of the thermal wind balance equation. The reference level is defined by the lowest speed recorded by the current meters across the slope, i.e. at the bottom at PM/KN and at 200 m depth at AP. Further details on the OI are given in the Appendix A.2.

### 2.2.2 *Seasonal variations in temperature and speed*

Moored current meter data collected between 1989 and 2017 are compiled at the three different study locations to compare the seasonal variations of temperature and velocity upstream and downstream of the dense water formation

regions (data coverage given in Fig. 9). At each study location, data from instruments located at different depths in the water column have been compiled separately for each mooring that were deployed across the BCS, over the 1000, 2000-2500 and 3000/3500 m isobaths. Records collected at the same position and within the same depth range are compiled to obtain multi-year time series divided into uniformly sampled interval periods. 3-hourly records are resampled at 2-hourly intervals, gaps associated with the turn-around of the moorings are interpolated and, a 5<sup>th</sup> order low-pass Butterworth filter is applied on the interval periods to filter out frequencies higher than 1/30 days. Note that the data recorded between 1990 and 1994 at AP is discarded because the mooring were then located at a slightly different position than for the rest of the record, leading to differences in velocity regimes (bottom panel, Fig. 9). The multi-year time series are averaged monthly for all available years to deduce the seasonal cycle of temperature and velocity at each depth. The standard error associated with the multi-year average of monthly means is defined for each month as,

$$\sigma_{\text{err}}(m) = \frac{\sigma(m)}{\sqrt{N}} \quad (1)$$

where,  $m$  is the month.  $\sigma$  is the monthly standard deviation of the multi-year averages and  $N$  is the effective number of degrees of freedom. Since the decorrelation time-scales ( $d_\tau$ ) range between twenty days and six months,  $N$  is also the number of years used to calculate the seasonal cycles because no two (or more) independent values exist within a given month of any year. Note that salinity measurements are too sparse to perform a seasonal analysis. Finally, a piecewise cubic hermite interpolating polynomial is used to infer a continuous vertical velocity profile between the instrument depths. Multi-year averages of monthly velocity profiles are depth-averaged to estimate the seasonal cycle of barotropic velocity. The seasonal cycle of barotropic velocity is subtracted from the multi-year average of monthly velocities at the surface and at the bottom to estimate the remaining baroclinic seasonal cycle. Hereinafter,  $u$  refers to the velocity projected onto the interannual-mean barotropic direction while the velocity normal to this direction is not considered in this study. The error associated with the vertical average is defined in Appendix A.3.

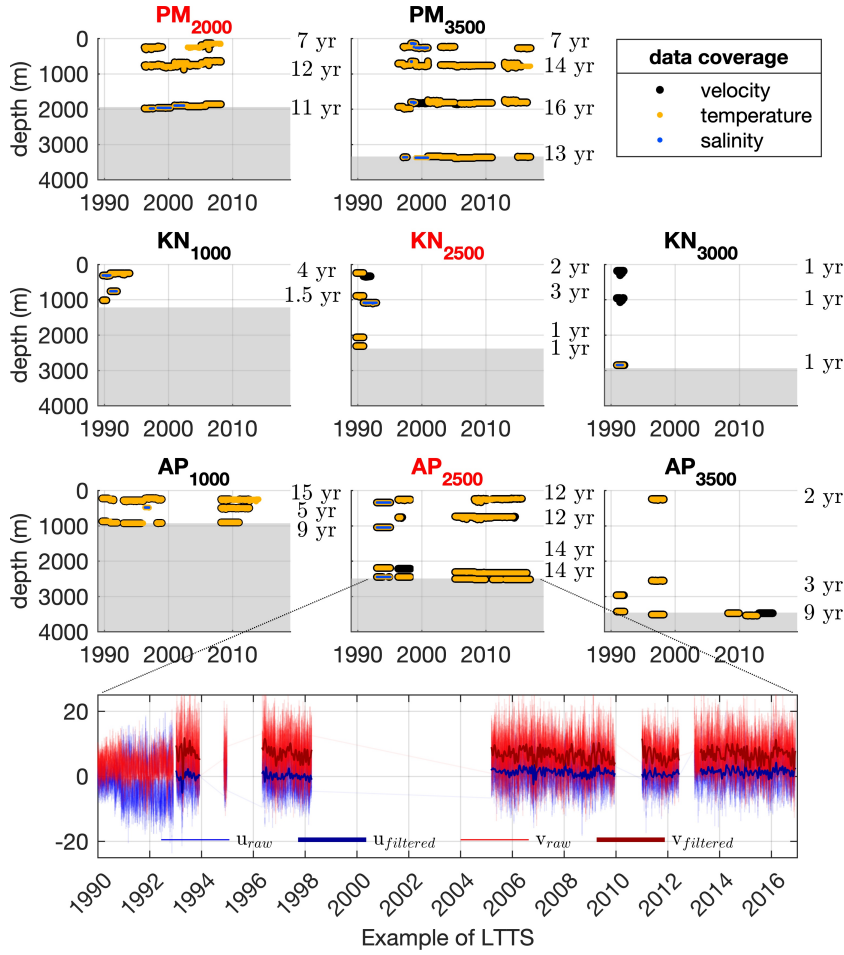


Figure 9: Moored data available for seasonal analysis. Velocity, temperature and salinity data points are plotted on top of each other to highlight the overlapping data. The length of the velocity record is given in years (yr) at each level. The moorings labelled red are used to estimate the barotropic seasonality along the 2000-2500 m isobaths. The bottom panel shows an example of a multi-year time series of zonal and meridional velocity constructed from the moored current meters at the bottom of AP<sub>2500</sub>.

### 2.2.3 Seasonal variations in surface stress

Seasonal maps of surface stress are constructed to estimate the momentum transfer into the ocean. Following Dotto et al. (2018), the surface stress is weighted as a function of the wind velocity at 10 m above sea level ( $u_{air}$ ), the sea-ice concentration ( $\alpha$ ) and the sea-ice velocity ( $u_{ice}$ ):

$$\vec{\tau}_{wicv} = \alpha \vec{\tau}_{ice-ocean} + (1 - \alpha) \vec{\tau}_{air-ocean} \quad (2)$$

where

$$\vec{\tau}_{ice-ocean} = \rho_o C_{io} |\vec{u}_{ice}| \vec{u}_{ice} \quad (3)$$

$$\vec{\tau}_{air-ocean} = \rho_a C_{ao} |\vec{u}_{air}| \vec{u}_{air} \quad (4)$$

$\rho_a$  and  $\rho_o$  are the air and the ocean density set to 1.25 and 1027 kg m<sup>-3</sup>, respectively.  $C_{ao}$  and  $C_{io}$  are the air-ocean and ice-ocean drag coefficient set to  $1.25 \times 10^{-3}$  and  $5.5 \times 10^{-3}$ , respectively. This formulation assumes an ocean at rest, neglecting the stress applied by the surface currents onto the ice floes, which might create a bias in the estimation of the surface stress in the vicinity of the BCS (Stewart et al., 2019). To check the robustness of our results and relate them to previous studies, results obtained using the formulation of Dotto et al. (2018) are compared with results from three additional methods of calculating surface stresses: one assuming a constant drag coefficient set to  $1.5 \times 10^{-3}$  ( $\tau_w$ ) (Armitage et al., 2018), the second accounting for the sea-ice concentration and distinguishing between skin drag over smooth floes and form drag over floe edges ( $\tau_{wic}$ ) (Lüpkes and Gryanik, 2015; Lüpkes et al., 2012); and the last using surface stress output from a locally high-resolution configuration of the FESOM model ( $\tau_{model}$ ) (Timmermann et al., 2012). Multi-year time series of surface stress is constructed using daily outputs of wind velocity from ERA-interim (Dee et al., 2011) and daily satellite observations of sea-ice concentration and velocity (Cavaliere et al., 1996; Tschudi et al., 2019). These time series are filtered with a 30-day low-pass filter and averaged monthly between 1989 and 2017 to produce seasonal maps of surface stress. The standard error associated with the calculation of the mean is given by Equation 1 (Section 2.2.2). Zonal and meridional components are projected onto the along-slope direction and averaged over the continental slope width to estimate the along-slope surface stress and relate it to the coastal convergence of water masses via Ekman transport (Ekman, 1905). Finally, the Ekman pumping ( $w_{EK}$ ) is used to locate the upwelling and downwelling areas,

$$w_{EK} = \vec{\nabla} \times \left( \frac{\vec{\tau}}{\rho_o f} \right) \quad (5)$$

where  $f$  is the Coriolis force and  $\vec{\tau}$  is the surface stress, which varies with the method used.

#### 2.2.4 Empirical orthogonal function analysis (EOF)

An empirical orthogonal function analysis (EOF) is performed on monthly-mean maps of sea-level anomalies (SLA) (Armitage et al., 2018) and surface stress to assess the dominant mode of seasonal variability at the surface. The modal decomposition is defined such that the modes are statistically independent of each other (Emery and Thomson, 2001),

$$\text{Map}(x, y, t) = \text{PC}_1(t) \times m_1(x, y) + \text{PC}_2(t) \times m_2(x, y) + \epsilon(x, y, t) \quad (6)$$

where PC and  $m$  represent the monthly-varying principal component and the spatial distribution of the two first modes, respectively.  $\epsilon$  represents the variability explained by higher modes. The domain used to perform the EOF extends zonally from 65°W to 60°E and meridionally from the edge of the ice shelf to the northern limit where the Ekman pumping vanishes.

### 2.3 TWO-LAYER CYLINDRICAL MODEL

A conceptual model is used to investigate the ocean's baroclinic response to the seasonal forcing. Such a model has first been developed by Straneo (2006) for the Labrador Sea to explore the densification of the boundary current associated with the formation of dense water in the interior sea, showing the importance of the horizontal circulation in transporting heat poleward. The model has been adapted by Hattermann (2018) to investigate the pycnocline evolution in the narrow shelf region of the eastern Weddell (between 30°E and 30°W, Fig. 3). This thesis combines both model versions to focus on three key processes: the Ekman transport, the cross-slope transport of density through baroclinic instability, and dense shelf water formation. This section describes the model used in Hattermann (2018), which represents a fresh shelf regime where the growth of baroclinic instability balances the coastal downwelling of relatively fresh water associated with the predominance of along-slope winds.

## 2.3.1 Basic assumptions

The model in Hattermann (2018) represents a boundary current that flows cyclonically at the periphery of a closed interior basin on the  $f$ -plane (Fig. 10). A

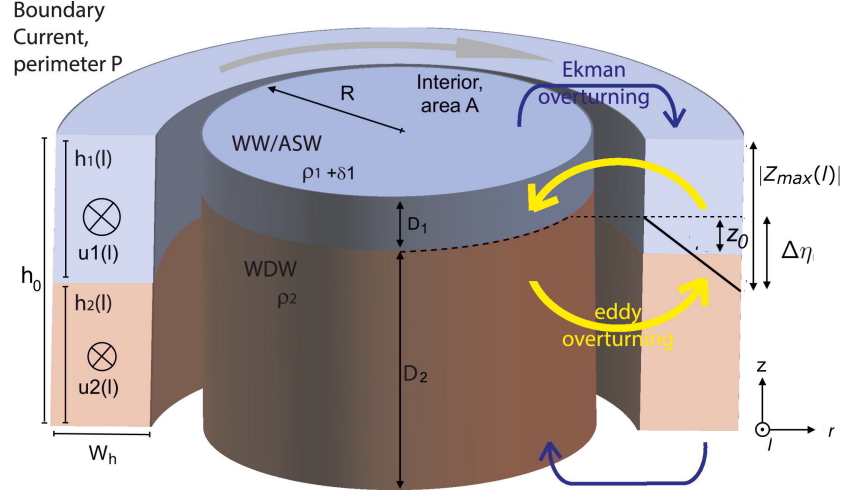


Figure 10: Schematic of the two-layer, semi-enclosed boundary current overturning model, simulating the along-slope evolution of the pycnocline (i.e. mWDW layer depth) in the narrow shelf region. The blue shaded area represents the upper layer. The red shaded area represents the lower layer. The black thick line represents the pycnocline slope (Figure adapted from Hattermann, 2018).

mean flow is prescribed in the boundary current, while the interior is assumed to be a density reservoir of negligible velocity. The boundary current region is an open channel where the stratification varies along-slope to represent the pycnocline evolution along the continental slope. Because spatial density gradients are more significant in the boundary current than in the interior (Fahrbach et al., 1994), the stratification is uniform in the latter (zero horizontal density gradient).

The model accounts for the density exchanges between the interior and the boundary current regions based on the conservation of density. The density variations depend both on the net transport of mass and on the mass input such that,

$$\partial_t \rho + \vec{\nabla} \cdot \rho \vec{u} = Q \quad (7)$$

where  $\rho$  is the density,  $\vec{u}$  is the velocity and  $Q$  is the surface density flux. The along-slope transport of mass is determined by the strength of the flow and the layers' thickness. The cross-slope transport of mass is determined by the

Ekman and the eddy overturning (blue and yellow arrows, Fig. 10). The Ekman overturning consists of the transport of surface waters from the interior into boundary current that is compensated by a return flow at depth. This circulation is controlled by the along-slope surface stress, which determines the surface and bottom Ekman transport. The eddy overturning forms a counter circulation that tends to cancel the cross-slope density gradient through baroclinic instability. Ekman and eddy overturning are both modulated by the difference in density between the layers. It represents the summer freshening of the surface layer associated sea-ice melting and diapycnal mixing (Hattermann, 2018). Because the model does not resolve the latter, the seasonal variations upper layer are considered indirect forcing, i.e. they are directly prescribed. The mass input associated with the transformation of surface and deep water into bottom water is negligible in the narrow shelf region such that the surface density flux is assumed to be null ( $Q=0$ ).

Since cross-slope density exchanges are assumed to be driven by the winds and counteracted by eddies, Equation 7 can be decomposed into a mean and a perturbed field such that  $\rho = \bar{\rho} + \rho'$ ,  $u = \bar{u} + u'$  and  $v = \bar{v} + v'$ , the bars corresponding to the geostrophic field and the prim corresponding to the eddy field. Eddies mainly participates to the cross-slope transport of density (Thompson et al., 2018) such that  $u'$  is negligible. Averaging Equation 7 over the eddy time-scale finally gives the density balance used to estimate the pycnocline evolution within the different regions,

$$\partial_t \bar{\rho} + \partial_x (\bar{\rho} \bar{u}) + \partial_y (\bar{\rho} \bar{v}_e) + \partial_y (\bar{\rho}' v') = 0 \quad (8)$$

1.                    2.                    3.                    4.

1. Density variations
2. Along-slope density transport by the mean flow
3. Cross-slope density transport through Ekman overturning
4. Cross-slope density transport through eddy overturning

where  $l$  and  $r$  are the along-slope and cross-slope coordinates, respectively (Fig. 10).

### 2.3.2 Strength and structure of the mean flow

The along-slope density transport (second term in Equation 8) depends on the strength and the structure of the flow (grey arrow, Fig. 10). The two-layer-depth-averaged flow strength is defined as,

$$U_{bt} = \frac{u_1 h_1 + u_2 h_2}{h_0} = \frac{T_S}{h_0 W_h} \quad (9)$$

where  $h_0$  is the boundary current depth,  $W_h$  is the boundary current width,  $u_1$  and  $u_2$  ( $h_1$  and  $h_2$ ) are the boundary current upper- and lower layer velocities (layer thickness), respectively.  $U_{bt}$  depends on the seasonally varying volume transport,  $T_S$  (right hand side of equation 9). This transport varies proportionally to the surface stress to represent a fast barotropic response to changes in the wind-field such that,

$$T_S(t) = T_0 \frac{\tau_S}{\tau_0} \quad (10)$$

where  $\tau_S$  is the seasonally varying surface stress, which is uniform along the continental slope (this term varies spatially in Chapter 4).  $T_0$  and  $\tau_0$  are the annual-mean volume transport and surface stress, respectively.

The flow is assumed to be in geostrophic equilibrium so, the difference in layer thickness between the interior gyre and the boundary current determines the baroclinic structure of the flow,

$$U_{bc} = u_1 - u_2 = \frac{g'}{f} \frac{\Delta\eta}{W_h} \quad (11)$$

where  $\Delta\eta = 2(h_1 - D_1)$ ,  $D_1$  and  $h_1$  being the upper layer thickness in the interior and in the boundary current, respectively.  $f$  is the Coriolis force.  $\Delta\eta/W_h = 2(h_1 - D_1)/W_h$  represents the sloping of the pycnocline between the interior gyre and the boundary current (Fig. 10).  $g' = g\Delta\rho/\rho_0$  is the reduced gravity, where  $\Delta\rho$  is the difference in layer density between the layers such that,

$$\Delta\rho = \Delta_{21} - \delta_1 \quad (12)$$

where  $\Delta_{21}$  is the annual-mean density difference between layer 2 and 1.  $\delta_1$  is the seasonal density anomalies in layer 1 ( $\delta_1$ ), representing the summer freshening of the surface layer associated with the mixing of ice melt-derived fresh

water. Combining Equations 9 and 11 finally gives the downstream velocities in the boundary current layers as a function of the volume transport and the cross-slope pycnocline slope,

$$u_1 = \frac{T_s}{h_0} + \frac{(h_0 - h_1)}{h_0} \frac{g' \Delta \eta}{f W_h} \quad \text{and} \quad u_2 = \frac{T_s}{h_0} - \frac{h_1}{h_0} \frac{g' \Delta \eta}{f W_h} \quad (13)$$

### 2.3.3 Cross-slope density fluxes

The density transport between the interior gyre and the boundary current is determined by the balance between Ekman and eddy overturning. The Ekman overturning comprises the on-shelf transport of surface waters through a surface Ekman layer and the off-shelf transport of deep water through a bottom Ekman layer (blue arrows, Fig. 10). Surface and bottom transports are in balance such that the net density flux across the boundary current/interior basin boundary associated with the Ekman transports (so-called Ekman overturning) is defined as,

$$\int_{h_0}^0 \overline{\rho v_e} dz = \begin{cases} \Delta \rho \frac{\tau_s}{\rho_0 f} & \text{at } r = R \\ 0 & \text{otherwise} \end{cases} \quad (14)$$

where  $\tau_s/(\rho_0 f)$  is the seasonally varying Ekman transport. The eddy overturning forms a counter circulation that tends to cancel the cross-slope density gradient (caused by the Ekman overturning) through baroclinic instability (yellow arrows, Fig. 10). Following the definition of Spall and Chapman (1998) and Straneo (2006), the eddy fluxes are proportional to the cross-slope pycnocline slope ( $\Delta \eta/W_h$ ) such that,

$$\overline{\rho' v'} = c \delta \rho(z) g' \frac{\Delta \eta}{f W_h} \quad (15)$$

where  $c$  is the efficiency coefficient and  $\delta \rho(z)$  is the density difference between the boundary current and the interior gyre. Vertically integrating Equation 15 gives the net density transport across the boundary current/interior basin boundary, so-called eddy overturning,

$$\int_{h_0}^0 \overline{\rho' v'} dz = \begin{cases} c \Delta \rho \frac{g'}{f} \frac{\Delta \eta}{W_h} z_0 & \text{at } r = R \\ 0 & \text{otherwise} \end{cases} \quad (16)$$

where  $z_0 = h_1 - D_1 = \Delta\eta/2$  is the vertical distance where the cross-shore density gradient differs from 0 ( $\delta\rho(z) = \Delta\rho$  for  $-D_1 > z > -2h_1 - D_1$  and 0 otherwise, Fig. 10). Consistent with eddies' formation through baroclinic instability, the pycnocline slope determines the amplitude of the cross-slope density flux: the steeper the slope is, the more eddies form to reduce the cross-slope density gradient. In the end, the net transport of density between the interior gyre and the boundary current is given by the sum of Equation 14 and 16.

#### 2.3.4 Diagnose the modified Warm Deep Water layer's depth

Equations 8, 13, 14, and 16 can be combined to find a set of prognostic equations for the mean layer thickness in the interior gyre and the downstream change in layer thickness in the boundary current. Knowing the layer thickness, one can diagnose the seasonal variability in pycnocline height, indicating the modified Warm Deep Water's depth. These prognostic equations will later be presented in Chapter 4 for the sake of conciseness. In fact, the model in Hattermann (2018) represents the variability in pycnocline height driven by the along-slope surface stress transport and the growth of baroclinic instability, both modulated by the seasonal change in density above the pycnocline. This balance is valid along the eastern Weddell Sea's continental slope, but the interaction between boundary current and dense shelf waters must also be considered in the southern-western Weddell Sea. One of this thesis's purposes is to modify the version of Hattermann (2018) to include the formation of dense shelf waters in the western-southern Weddell Sea (keeping the balance between surface stress, eddies, upper layer density modulation for the eastern Weddell Sea). Therefore, the modified version is presented in Chapter 4 and the new set of prognostic equations.

## BAROTROPIC AND BAROCLINIC VARIABILITY ALONG THE CONTINENTAL SLOPE

*(Identical to Le Pailh et al. 2020)*

---

Aiming for a comprehensive description of the evolution of the BCS along the Weddell Sea's continental slope, this Chapter combines historical observations from PM, KN and AP to provide an overview and first consistent analysis of the existing data (Fig. 11). Ship-based, Argo float and seal-borne CTD profiles are used to objectively map across-shore sections at the three study locations and compare the changes in ocean properties between the region upstream and downstream of the dense water formation regions. Multi-year mooring-based time series are combined to consistently explore the seasonality across the continental slope at the three study sites, relating it to the along-slope shift in density regime. Finally, changes in the ocean are linked to the spatial and temporal variability in surface stress. Section 3.1.1, 3.1.2 and 3.2 present climatological averages and seasonal variations of ocean velocity, hydrographic properties and surface stress. Section 3.5 discusses the annual mean changes along the continental slope, the seasonality of the depth-averaged flow strength and the seasonal variations in the baroclinic structure of the flow. Conclusions are given in Section 3.6.

### 3.1 ALONG-SLOPE CHANGES IN THE BCS PROPERTIES

#### 3.1.1 *Annual mean-state*

Our reconstructed cross-slope transects show the along-slope densification of the water masses that is consistent with previous findings (Fahrbach et al., 1994; Gill, 1973; Orsi et al., 1999). The stratification shifts from a two-layer system upstream of the dense water formation regions to a three-layer system downstream (Fig. 12). To delimit the layer interfaces, we here choose the 28.1 and 28.4 neutral density contours. At PM and KN, a subsurface density front, roughly located between 200 m and 800 m over the continental slope, separates

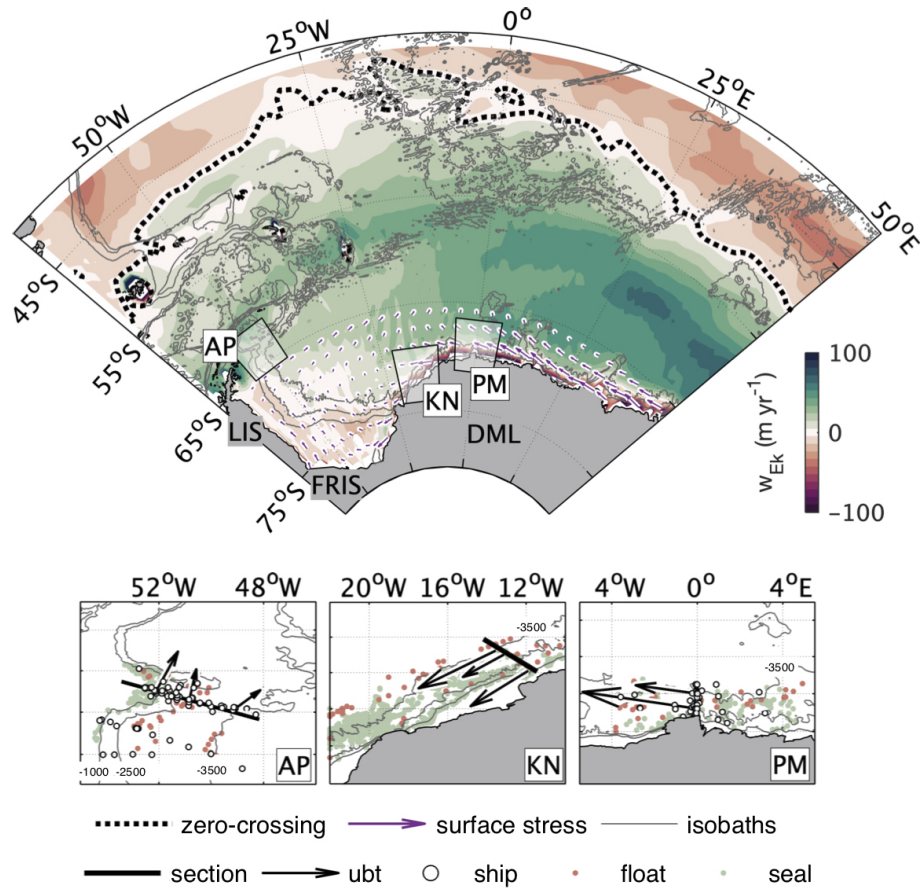


Figure 11: Top: Interannual-mean Ekman pumping,  $\overline{w_{EK}}$  (colormap spaced by  $10 \text{ m yr}^{-1}$ ). The black dotted line marks the northern zero-crossing of  $\overline{w_{EK}}$ . The purple arrows represent the surface stress. Larsen C Ice Shelf (LIS), Filchner Ronne Ice Shelf (FRIS) and Dronning Maud Land (DML) are indicated. Bottom: Zoom of study areas, indicating the tip of the Antarctic Peninsula (AP), Kapp Norvegia (KN) and the Prime Meridian (PM). Thick lines mark the nominal positions of the mapped sections, thin lines the positions of the 1000, 2000, and 3500 m isobaths. Black arrows represent the direction and strength of the mean barotropic flow (ubt) scaled to  $5 \text{ cm s}^{-1}$  (c.f. legend). Positions of CTD, Argo float and seal borne profiles are given by circles, red and green dots, respectively.

cold and fresh waters onshore from the warm and salty waters offshore (Fig. 12.a and 12.b). At AP, waters located onshore (offshore) of the continental slope are warmer and saltier (colder and fresher) than at PM/KN, which results in a weaker density front. This can be observed from the shape of the 28.1 neutral density contour, which ascends from an averaged depth (offshore depth) of 450 (200 m) at PM and KN to an averaged depth (offshore depth) of 300 m (150 m) at AP. A third layer of dense water, not present at PM and KN, also appears in the vicinity of the seafloor at AP (Fig. 12.c, neutral density contour 28.4). Accordingly, the cross-slope density gradient is reversed in the vicinity of the seafloor at AP.

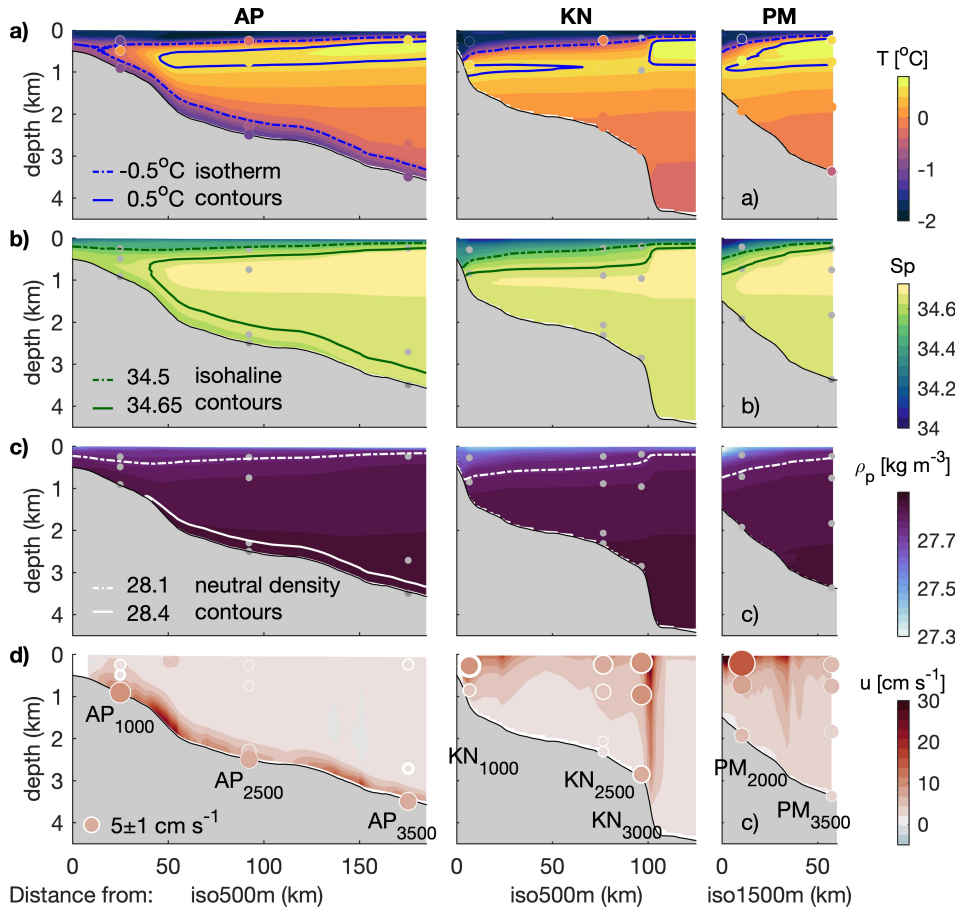


Figure 12: Climatologic sections of the mean (a) in situ temperature, (b) practical salinity, (c) potential density, and (d) along-slope baroclinic velocities derived from the thermal-wind relation at AP, KN and PM. The thermal-wind derived velocities are referenced at the bottom at PM and KN and at 200 m depth at AP. The sections are biased towards summer at the AP (Fig. 8). The mean properties measured by the current meters are plotted on top of the sections. Grey dots: positions of the moored current meters. Coloured circles: interannual-mean temperature and along-slope velocity measured by the moored current meters. The area of the latter is proportional to the amplitude of the velocity.

In agreement with the thermal wind balance, these changes in hydrographic properties are accompanied by changes in the vertical structure of the flow (Figure 12.d). The along-slope weakening in the subsurface density gradient and its reversal at the bottom leads to a shift in the baroclinic structure of the flow from being surface to bottom intensified. At PM and KN, the multi-year-mean speeds recorded by the current meters ranges from 5 to 15  $\text{cm s}^{-1}$  at 200 m depth, across the continental slope, and from 2 to 6  $\text{cm s}^{-1}$  near the bottom. At AP, the average current velocity is as low as 2  $\text{cm s}^{-1}$  throughout almost the entire water column. The exception occurs in the 300 m thick bottom layer of WSBW where the flow speed ranges between 6.5 to 9  $\text{cm s}^{-1}$ . In addition

to the changes in baroclinic shear, the magnitude of the flow speed decreases between KN and AP ( $u_{\max} > 30 \text{ cm s}^{-1}$  at KN and  $u_{\max} < 20 \text{ cm s}^{-1}$  at AP, Figure 12.d).. The decrease in depth-averaged flow speed is at least partly explained by mass conservation of the geostrophic current, which follows the diverging topography. Indeed, the distance between the isobaths at AP is twice as large as at KN : Cisewski et al. (2011) and Heywood et al. (1998) respectively describe a boundary current of 75-100 km width at the PM and KN while Thompson and Heywood (2008) relate a width of 200 km at AP.

These observations are valid, regardless of the summer bias of the data used to construct the interannual-mean sections (Fig. 8). For example, the OI does not capture the warmer temperature observed by the current meters between July and December at 200 m depth at KN<sub>2500</sub> and AP<sub>2500</sub>, and at 400 m depth at AP<sub>1000</sub> (Fig. 12.a and Fig. 13). However, the temperature is well reproduced elsewhere, and the thermal-wind derived baroclinic velocities are consistent with the current meter measurements (Fig. 12.d).

### 3.1.2 Seasonal variability

The previous sub-section emphasised some along-slope change of the hydrological properties of the water masses carried by the BCS. This sub-section focuses on the seasonal variability of the temperature at the three different mooring sites. Nevertheless, at KN, the seasonal cycle of temperature could not be retrieved because the time-series were too short. On the shallower edge of the continental slope, above the 1000 m isobath, our dataset shows no seasonality at any of the three mooring sites, except for the bottom of AP (Fig. 13, left panels). This highlights a larger sensitivity to sub-seasonal processes such as dense water runoff and/or frontal meanders. Above the middle and outer edge of the continental slope (i.e. above the 2000/2500 and 3000/3500 isobaths, respectively), observations show a gradual shift towards bottom amplified seasonal variations of temperature along the slope (Fig. 13, middle and right panels), which is consistent with the presence of dense shelf regime on the western part of the Antarctic Peninsula. At PM and KN, i.e. upstream of the dense water formation, the seasonal amplitude of temperature variations is maximum for surface waters. The seasonal cycle at 200 m and 700-1000 m depth vary in opposite phase because the temperature sensors capture the

vertical movements of the WDW layer. The latter is characterized by a tempera-

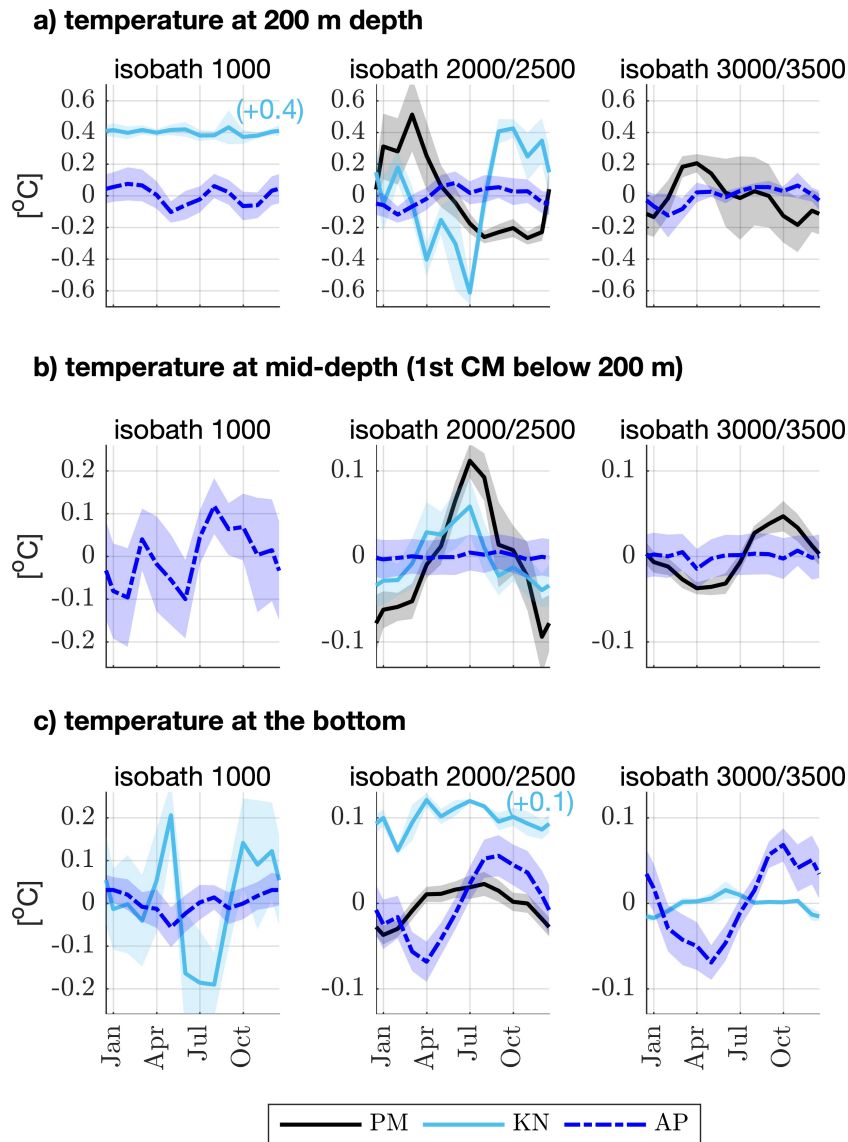


Figure 13: Seasonal temperature estimated at three study sites along the 1000, 2000/2500, and 3000/3500 m isobaths. (a) temperature at 200 m depth, (b) temperature at mid-depth and (c) temperature at the bottom. The shaded areas represent the standard error. Note the difference in scale between the plots. Some temperature cycles are shifted along the y-axis to not overlap with the other cycles. The number indicates the shift in  $^{\circ}\text{C}$ .

ture maximum at 400 m depth (Fig. 12.a). Therefore, when it uplifts (deepens), temperature increases (decreases) at 200 m depth and decreases (increases) at 700-1000 m depth. Nearby the bottom (panel c2), the seasonal cycle is weaker and in phase with the one at 700-1000 m depth. At AP, downstream of the dense water formation region, seasonal temperature variations are maximum at the bottom (panels c2 and c3). While at 700-1000 m depth temperature variations have no seasonality, a seasonal cycle can still be observed at 200 m depth

(panels a2 and a3) with a weaker amplitude than upstream, i.e. at PM and KN. This indicates a decoupling between the surface layer and the dense plume and a weakening of the surface seasonality along the slope. At depth, nearby the bottom, a seasonal signal is found above the 2000-2500m and 3000-3500m isobaths (panels c2 and c3) with 1-month lag in the offshore direction. This seasonal variability is comparable with the one observed at 700-1000 m depth upstream, at PM (panels b2 and b3), and will be discussed in Section 3.5.4.

Despite the interannual-mean shift in density regime, the seasonal variability in velocity is mainly barotropic along the continental slope (Fig. 14). Comparing the seasonal cycles of barotropic velocity suggests that a coherent seasonal acceleration of the barotropic flow exists along the continental slope with a time-lag between the 2000/2500 and 3000/3500 m isobaths. In fact, with the exception of the 1000 m isobath, the seasonal cycle of barotropic velocity is mostly in phase among all sites (Fig. 14.a). A maximum (minimum) occurs in April/May (between December and February) above the 2000-2500 m isobath while the signal is lagged by 1-month above the 3500 m isobath. However, the seasonal variability above the 2000/2500 isobaths is not clear at AP because the amplitude of the seasonal variations progressively decreases from  $7 \text{ cm s}^{-1}$  at PM to  $1\text{-}3 \text{ cm s}^{-1}$  at AP (panel b2). The decrease in velocity is not valid along the 3000/3500 isobath (panel b3) because KN<sub>3500</sub> is located near a velocity front. This velocity front is associated with an abrupt change in topography (Fig. 12.d), which separates offshore and onshore water masses. As the amplitude of the seasonal variability decreases along the continental slope, both the uncertainty in the seasonal cycle and the offshore lag increases. However, the seasonal cycles remain significant at all sites.

The baroclinic velocities are defined as the difference between the absolute velocity and the barotropic component. These velocities are shown at the surface and the bottom in Figure 14.b and 14.c, respectively. As the baroclinic structure of the flow shifts from being surface to bottom intensified along the slope, the baroclinic velocities shift from being larger at the surface at PM and KN to being larger at the bottom of AP. At PM, the amplitude baroclinic velocities varies by  $1\text{-}6 \text{ cm s}^{-1}$  over the year (black line, Fig. 14.b), lagging the barotropic signal by 1-2 months. Above the 2000-2500 m isobath, they reach a maximum at 200 m depth and a minimum at the bottom in June (black line, panels b2 and c2, respectively).

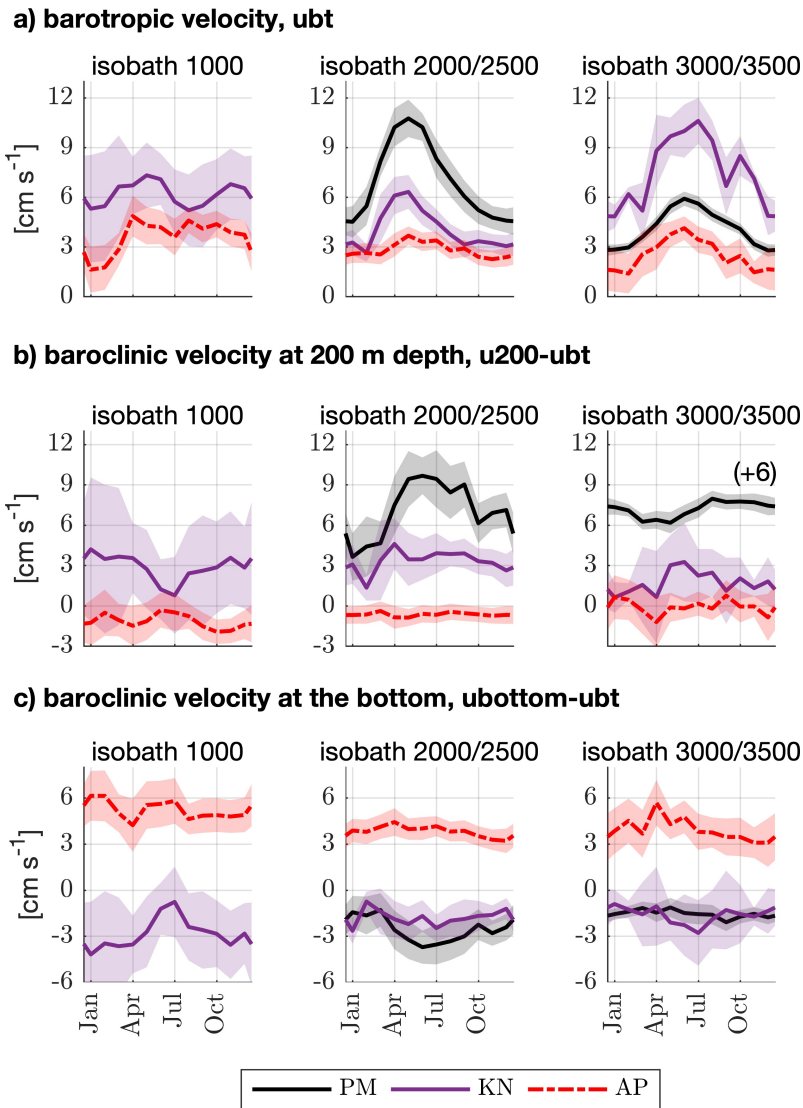


Figure 14: Seasonal velocity estimated at three study sites along the 1000, 2000/2500, and 3000/3500 m isobaths. (a) depth-averaged velocity, (b) baroclinic seasonality at 200 m depth and (c) baroclinic seasonality at the bottom. The shaded areas represent the standard error. The barotropic component is defined as the depth-averaged velocity. The baroclinic component is defined as the difference between the absolute velocity and the depth-averaged velocity. The baroclinic seasonal cycle in the middle right panel (black line) is shifted by  $6 \text{ cm s}^{-1}$  to not overlap with the other cycles.

Above the 3500 m isobath, the signal is lagged by 3 months at 200 m depth, and the variations are negligible at the bottom (panels b3 and c3, respectively). The data are generally not sufficient to fully assess the seasonal variability at KN. Nevertheless, it is worth noting that the baroclinic variability is enhanced between March and June, in phase with the maximum flow speed (i.e. standard error in purple, panels b2 and b3). At AP, downstream of the dense water formation region, the analysis suggests a baroclinic seasonal cycle exists at the

bottom. The signal is maximum (minimum) in April (December/January) at the 2000-2500 m and 3500 m isobath (dashed line, Fig. 14.c, panels c2 and c3) and its amplitude matches the barotropic variability. However, our conclusions are limited by the uncertainty of the baroclinic cycles, which is larger than at PM and KN. No seasonality is observed at 200 m depth nor along the 1000 m isobath at all locations and depths.

### 3.2 RELATION TO THE SURFACE STRESS

The input of dense waters from the continental shelves is expected to be the main driver of interannual-mean changes along-slope. Nevertheless, the weakening of both the Ekman pumping and along-slope surface stress downstream of KN (Figure 11 and 15.a) can partially explain the ascent of the pycnocline depth between KN and AP. The Ekman pumping reaches up to  $100 \text{ m year}^{-1}$  east of PM, whereas it is smaller than  $20 \text{ m year}^{-1}$  between KN and AP. In the BCS vicinity, the along-slope surface stress reaches up to  $0.12\text{-}0.16 \text{ N m}^{-2}$  upstream of KN, whereas it becomes negligible downstream. This implies a weakening of the downwelling across the continental slope downstream of KN, leading the pycnocline to slope upwards towards the AP (Section 3.1.1).

The seasonal variability of velocity and temperature associated with the surface stress consists of two components: i) The Ekman pumping averaged over the gyre, which controls sea level anomalies and the upwelling in the centre of the gyre and ii) the along-slope surface stress averaged across the continental slope, which controls the sea-level anomalies and the downwelling at the coast. These components determine the across-slope gradient of sea-level and density anomalies, which sets the flow strength and the baroclinic structure of the flow, respectively. The gyre scale Ekman pumping exhibits a seasonal cycle with a maximum (minimum) in June (December-January), independently of the method used to estimate the surface stress (Fig. 15.b, right panel). Only the magnitude differs. This cycle peaks 1-2 months later than the depth-averaged flow strength (Fig. 14, panels a2 and a3). This suggests that the barotropic flow is rather controlled by the surface stress or/and by the change in thermohaline properties along the continental slope than by the gyre-scale surface stress. The seasonal cycle of along-slope surface stress differs according to the stress formulation (Fig. 15.a and 15.b panel A, B, C and D). Regarding  $\tau_{wicv}$ ,

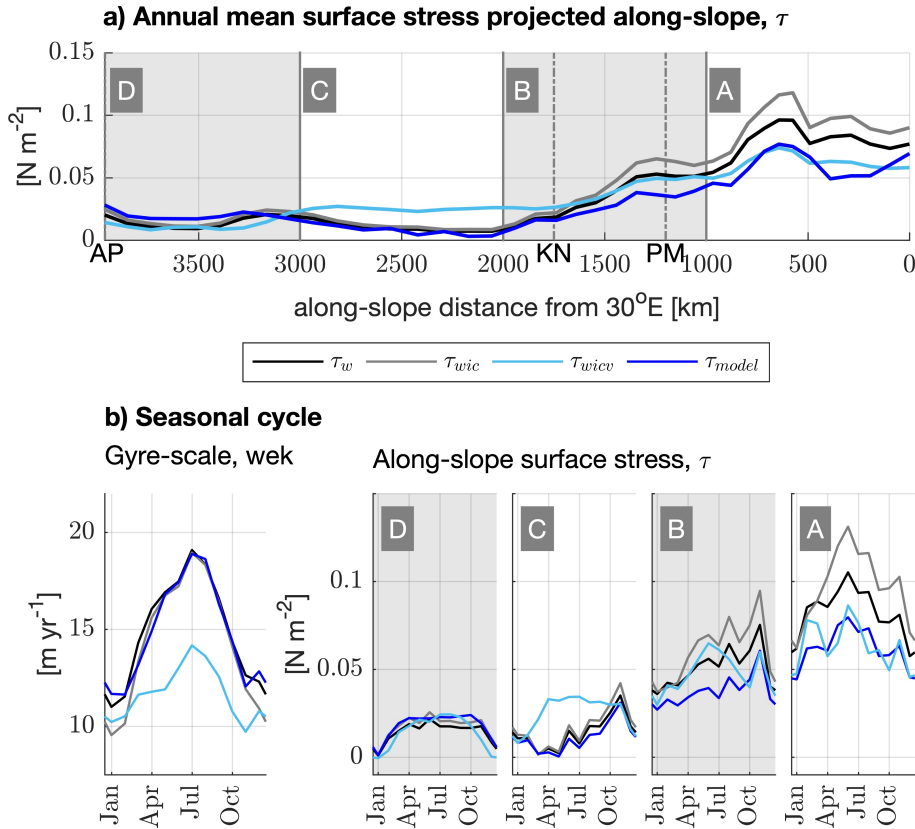


Figure 15: Along-slope and seasonal variability in surface stress. a) Annual-mean surface-stress averaged across the continental slope within 100 km band centred on the 2500 m isobath. b) Seasonal variability in Ekman pumping and surface stress projected along-slope. The Ekman pumping is averaged over the gyre, south of the zero-crossing given in Figure 11. The along-slope stress is averaged across, and along the continental slope within the domain, A, B, C and D. Four different estimates of surface stress are compared to represent its uncertainty.  $\tau_w$ ,  $\tau_{wic}$ ,  $\tau_{wicv}$  and  $\tau_{model}$  are defined in the main manuscript in Section 2.2.3. The standard errors associated with each product are negligible for the Ekman pumping and below  $0.015 \text{ N m}^{-2}$  for the along-slope stress.

the along-slope surface stress varies by  $0.03\text{-}0.05 \text{ N m}^{-2}$  over the year. The seasonal cycle is indistinct upstream of PM (region A), and it reaches a maximum (minimum) in winter (summer) downstream. Contrastingly, the seasonal signal peaks in winter at PM, for either  $\tau_w$ ,  $\tau_{wic}$  or  $\tau_{model}$ . Also, the along-slope surface stress peaks in November between  $20^\circ\text{W}$  and  $60^\circ\text{W}$  instead of peaking in winter (region B and C on Fig. 15.b). Ultimately, the uncertainty in sea-ice/ocean momentum transfer is too large to directly match the local averages in seasonal surface stress with the seasonal cycles of temperature and velocity given in Figure 13 and 14.

### 3.3 COHERENT SEASONAL ACCELERATION OF THE BAROTROPIC FLOW ALONG THE CONTINENTAL SLOPE

The coherent seasonal acceleration of the barotropic flow and its across-slope lag is confirmed along the 2000/2500 and 3000/3500 isobaths on Figure 16.a and 16.b. The barotropic signal is well captured at KN, despite the sparsity of the data (Fig. 9). In fact, the seasonal barotropic signal from our data compilation shows a similar seasonality with data from a more recent year-long mooring deployed 350 km downstream of our study site (Graham et al., 2013) (Fig. 34, Appendix A.4). This suggests that opposingly to the baroclinic cycle, the seasonal acceleration of the barotropic flow is consistent over the years at this study location. An EOF analysis shows that the along-slope seasonal acceleration of the flow is also present in the variability of sea-level anomalies (SLA). The first mode of SLA, which is associated with an across-slope gradient along the slope (Fig. 16.c), is in phase with the seasonal cycle of barotropic velocity along the 2000/2500 m isobath ( $r=1$  at 0-lag). This confirms the existence of a coherent seasonal cycle of the geostrophic flow intensity. The second mode, which is associated with seasonal changes in the zonal gradient of SLA has a maximum correlation of  $r=0.8$  at 2-months lag ( $r=-0.1$  at 0-lag). This implies that the meridional flow associated with the zonal gradient of SLA is at least partly decoupled from the barotropic seasonal cycle.

The seasonal analysis in surface stress shows a maximum input upstream of the Prime Meridian (Fig. 15.b). Except for  $\tau_{w_{icv}}$ , the surface stress increases between January and May, in phase with the barotropic flow. Anticipating a connection between the zonal stress and the barotropic flow, we used an EOF approach to identify the gyre-scale pattern of zonal stress. The first mode of variability shows a meridional oscillation of the zonal winds (Fig. 16.d). It correlates with the seasonal cycle of barotropic flow along the 2000/2500 isobath with  $r=0.5$  at 0-lag, but their respective seasonality differs. The second mode, which is associated with a cyclonic momentum input on the eastern side of the gyre in autumn, presents a similar seasonal cycle with the barotropic flow along both isobaths, with  $r=0.8$  at 0-lag along the 2000/2500 m isobath. This correlation suggests that the along-slope surface stress, which controls the cross-slope gradient of SLA on the eastern margin, relates to the barotropic

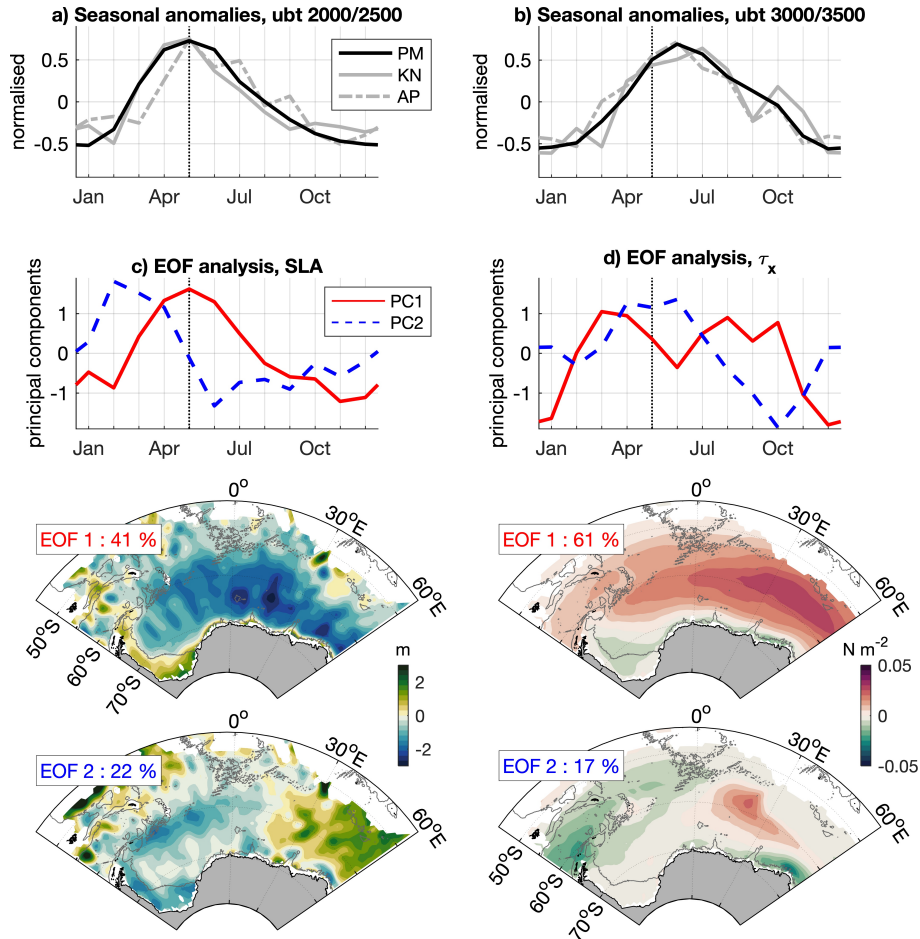


Figure 16: Comparison between the phase of the barotropic flow (ubt) at the three study sites, the variability in sea-level anomalies (SLA) and the variability in zonal surface stress. Panel a and b show the normalised barotropic velocity along the 2000/2500 and 3000/3500 m isobaths, respectively. Panels c and d show the EOF analysis on sea-level anomalies and zonal stress ( $\tau_{wicv}$ ), respectively. The two first principal components and their corresponding modes are presented from top to bottom.

seasonal cycle for all three sites. This result is valid for all four surface stress estimates (Fig. 35, Appendix A.5).

### 3.4 CORRELATION BETWEEN THE BAROTROPIC VARIABILITY AT THE TIP OF THE ANTARCTIC PENINSULA AND THE SURFACE STRESS

Our previous analysis computed seasonal cycles independently from each other and compared their variability. Such comparisons reveal if patterns covary in time but do not provide compelling evidence for causal linkages. To test for a causal relationship between momentum input in the eastern Weddell Sea and seasonal acceleration of the barotropic flow at AP, we correlated the ve-

locities recorded at AP with the different components of surface stress (Fig. 17). The seasonal variability is barotropic above the dense plume (Fig. 14, panel b2) and we chose the along-slope velocity at 750 m depth at AP<sub>2500</sub> ( $u_{750}$ ) to monitor the barotropic variations. This choice allowed constructing a 10-year long time-series rather than 5 years by constructing monthly barotropic time-series. A mean value was subtracted for each 2-hourly interval period to avoid spurious correlations. Indeed, a shift in velocity associated with a change in current meter depth would artificially bias the correlation towards low-frequencies. Finally, the records were averaged monthly to obtain a monthly-mean time-series, which covers 2005 to 2015 ( $u_{750}$ , Fig. 17.a).

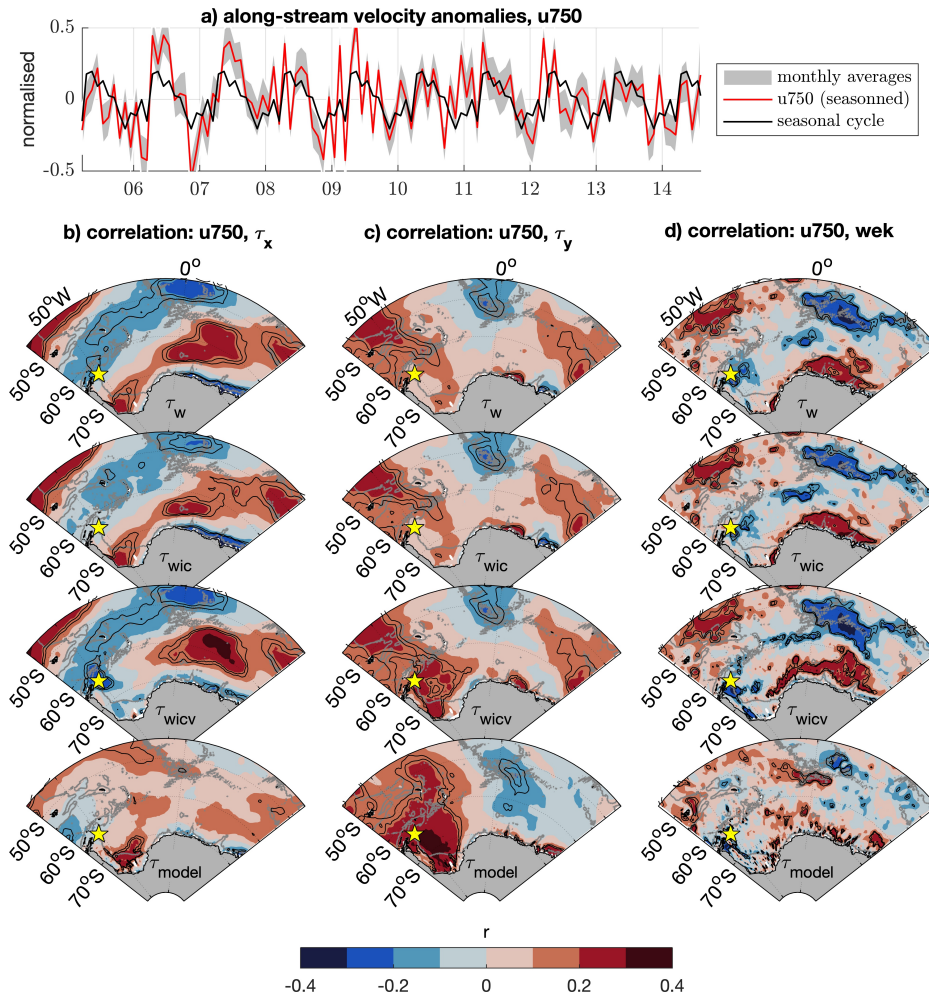


Figure 17: Zero-lag correlation between the monthly velocity observed between 2005 and 2015 at AP<sub>2500</sub> and the different components of surface stress. The velocity at 750 m is used as a proxy for the barotropic variations. The correlations maps are computed for four different estimates of surface stress, as described in Section 2.2.3. a) monthly velocity at 750 m depth. b, c and d) Correlation between  $u_{750}$  and the zonal stress, meridional stress and Ekman pumping, respectively. The star shows the position of AP<sub>2500</sub>. The black contours represent 90 and 95 % confidence interval.

The relationship between the cyclonic momentum input on the eastern margin of the study area and the seasonal acceleration of the barotropic flow is confirmed for three surface stress products (Figure 17.b). The correlation between  $u_{750}$  and westerly winds offshore ( $r > 0.2$ )/easterly winds along the continental margin ( $r < -0.2$ ) is significant for  $\tau_w$ ,  $\tau_{wic}$ . For  $\tau_{wicv}$ , the correlation is significant with the westerly winds only. A significant correlation associated with the across-slope surface stress is also found on the western margin for  $\tau_w$ ,  $\tau_{wic}$  and  $\tau_{model}$  ( $r > 0.2$ ). However, an increase in surface stress in the offshore direction cannot relate directly to the acceleration of the barotropic flow.  $\tau_{wic}$  and  $\tau_{model}$  show a significant correlation associated with the northward stress along the western margin ( $r > 0.2$ , Fig. 17.c). Nevertheless, no coastline can support the downwelling associated with the onshore Ekman transport there. The strongest correlation between  $u_{750}$  and Ekman pumping ( $w_{ek}$ ) is found upstream of the Prime Meridian, between  $60^\circ\text{S}$  and  $70^\circ\text{S}$  ( $\tau_w$ ,  $\tau_{wic}$  and  $\tau_{wicv}$ , Fig. 17.d). This result is consistent with a summer intensification of the easterly and westerly winds, which control the upwelling of waters offshore of the continental slope and the downwelling associated with the easterly winds at the continental margin (Fig. 16.d). The ocean does not immediately respond to the Ekman pumping, and its intensification needs to last a few months to explain an acceleration of the flow. For  $\tau_w$ ,  $\tau_{wic}$  and  $\tau_{wicv}$ , even though  $u_{750}$  is correlated with downwelling associated with negative Ekman pumping at AP ( $r < -0.2$ , Fig. 17), no lagged correlation exists. The correlation between  $u_{750}$  and the Ekman pumping persists up to 2 months upstream of  $20^\circ\text{E}$  (lagged correlation in Fig. 36, Appendix A.6), confirming that the seasonal acceleration of the barotropic flow is correlated with an increase in atmospheric forcing that slowly propagates westward in front of the eastern margin. Even though this correlation is not found in  $\tau_{model}$ , the connection between eastern atmospheric input and barotropic seasonality is found when averaging the monthly variability over the years (EOF analysis in Fig. 35, Appendix A.5). This suggests a larger inter-annual variability in the model and also confirms the large uncertainty in ice-ocean momentum transfer. It also confirms the large uncertainty on the momentum transfer between ice-ocean.

In summary, the correlation analysis suggests that the along-slope barotropic flow mainly responds rapidly to a seasonal convergence of water masses as-

sociated with the surface stress on the eastern gyre. Nevertheless, it is not possible to fully assess if this convergence of water masses is controlled by the open ocean Ekman pumping or by the southward Ekman transport. Indeed, the spatial distribution in surface stress depends on the momentum transfer between ice and ocean, which is partly unknown.

### 3.5 DISCUSSION

#### 3.5.1 *Annual mean shift in flow regime along-slope*

Although the along-slope densification of the water masses is well established Gill (1973), we have provided new insight into the along-slope shift in density regime, by combining historical data from a variety of sources from along the continental slope of the Weddell Sea. The along-slope cooling and salt enrichment of the shelf waters shown in the climatological sections (Fig. 12) attest the importance of the DML and the FRIS continental shelves for shifting from a fresh to a dense shelf regime. Along the pathway of the BCS, modified Warm Deep Water (mWDW) exchanges properties with the less saline Eastern Shelf Water formed along the narrow continental shelf of Dronning Maud Land, and with the High Salinity Shelf Water (HSSW) and Ice Shelf Water (ISW) formed on the continental shelves in front of the Filchner-Ronne Ice Shelf (FRIS) and Larsen Ice Shelf (LIS) through surface thermohaline forcing and convection (Nicholls et al., 2009). This leads to the formation of Weddell Sea Deep Water (WSDW) and the flow of Weddell Sea Bottom Water (WSBW) along the western continental slope. This dense water outflow may subsequently create instabilities that foster transport of WDW onto the continental shelf as suggested by an idealised model simulations (Stewart and Thompson, 2016). Meanwhile, the surface stress weakens downstream of KN and, in the absence of coastline, the downwelling of lighter water at the coast associated with the Ekman transport reduces. (Mosby, 1934; Nøst et al., 2011; Zhou et al., 2014). Therefore, the BCS dynamics change from being directly driven by atmospheric processes along the DML coast (Hattermann, 2018; Riboni and Fahrback, 2009) to being dominated by continental shelf processes downstream of the FRIS. The density input from the continental shelves and the weakening of the surface stress lead the pycnocline and the halocline to slope upwards towards the AP. Also, the

cross-slope density gradient, which is negative upstream of KN, weakens at the surface and reverses at the bottom towards the AP. In the end, the along-slope shift from a fresh to a dense shelf regime (Thompson et al., 2018) results in a reversal of interannual-mean baroclinic shear along the slope. Note that several other processes shape the boundary current system. For instance, KN is an area of complex topography where the flow is still influenced by upstream variations (Graham et al., 2013; Heywood et al., 1998) and the AP is an area where barotropic jets, unresolved in our analysis, are known to exist (Stewart and Thompson, 2016; Thompson and Heywood, 2008).

### 3.5.2 *Seasonal acceleration of the barotropic flow*

Our analysis revealed that a coherent seasonal cycle of the barotropic flow exists along the slope, with 1-month lag in the offshore direction. The seasonal cycle is captured upstream and downstream of the dense water formation regions. Its coherency is confirmed in the variability in sea-level anomalies. While along-slope shifts in the baroclinic structure of the flow exist, the variability observed above the dense plume remains barotropic at AP. In fact, the barotropic cycle accounts for more than 50 % of the variability in bottom velocity at the 2500 m and 3500 m isobaths (Fig. 14). This suggests that most of the seasonal variability in bottom water transport is associated with the seasonal acceleration of the barotropic flow along the slope. However, current meter measurements are also needed at locations where the dense water outflow is the most energetic, i.e. where the bottom slope is the steepest, to quantify the seasonal transport above and inside the dense plume.

The cross-slope phase lag between the 2000/2500 and 3000/3500 m isobaths is found at the three study sites. However, the seasonal acceleration/deceleration of the flow is slightly offset towards winter at AP. This suggests a weakening of the across-slope phase lag towards the Antarctic Peninsula, which can be explained by the seasonal changes in thermohaline properties at the surface. As sea-ice melts during austral summer, the across-slope density gradient between light surface water and deep water increases (Hattermann, 2018). Theoretically, this would modulate the cross-slope gradient of sea-level anomalies that relates to the geostrophic flow intensity and temporally shifts the maximum depth-averaged flow strength towards summer. Such mechanisms would

be enhanced onshore and could both explain why an across-slope seasonal lag exists along the slope and why the maximum surface stress lags the maximum bottom velocities by few months at  $PM_{2000}$  and  $KN_{2500}$  (Fig. 14). At AP, the across-slope transport of surface water associated with the along-slope surface stress is weaker, reducing the steric contribution to the sea-level anomalies at the coast and limiting the shift towards summer along the 2000/2500 isobaths. Alternatively, Riboni and Fahrback (2009) argued that the local modulation of surface momentum input by the sea-ice explains the lag across-slope. However, the spatial uncertainty on the surface stress remains too large to comment on their hypothesis. Seasonal changes at the gyre inflow (Cisewski et al., 2011; Ryan et al., 2016) could also modify the seasonality across-slope. However, an increase in flow speed over the continental slope might result in an increase in flow speed, offshore of the continental slope, further downstream. Thus, it would not explain why a phase-lag remains at AP. In the end, both uncertainties on the barotropic variations and the surface stress are too large to conclude about the cross-slope lag.

### 3.5.3 *Teleconnection between flow speed and eastern/north-eastern Weddell Sea winds*

The seasonal cycle in barotropic velocity is not strongly correlated to spatial averages of surface stress and Ekman pumping, suggesting that neither the local surface stress nor the gyre-scale Ekman pumping directly control the barotropic fluctuations. To corroborate this statement, we investigated the spatial variability in surface stress, using an EOF approach (Fig. 16) and spatially correlating the monthly variability in surface stress with the monthly variability in barotropic velocity (Fig. 17). Both analyses relate the seasonality of the barotropic flow with a surface momentum input on the eastern side of the gyre. This non-local correlation suggests that a teleconnection exists between the atmospheric momentum input on the eastern side of the gyre and the barotropic flow. This might be explained by the conservation of planetary vorticity along closed topographic contours (Isachsen et al., 2003) and the rapid westward propagation of sea level anomalies of a few centimetres height via barotropic Kelvin-Rossby waves (Hughes and Meredith, 2006; Spence et al., 2017). Although the significance is less clear, the patterns found in the de-

seasoned correlation maps are comparable with the seasoned correlation (Fig. 18 and Fig. 17, respectively). In particular, the zonal stress and the Ekman up-

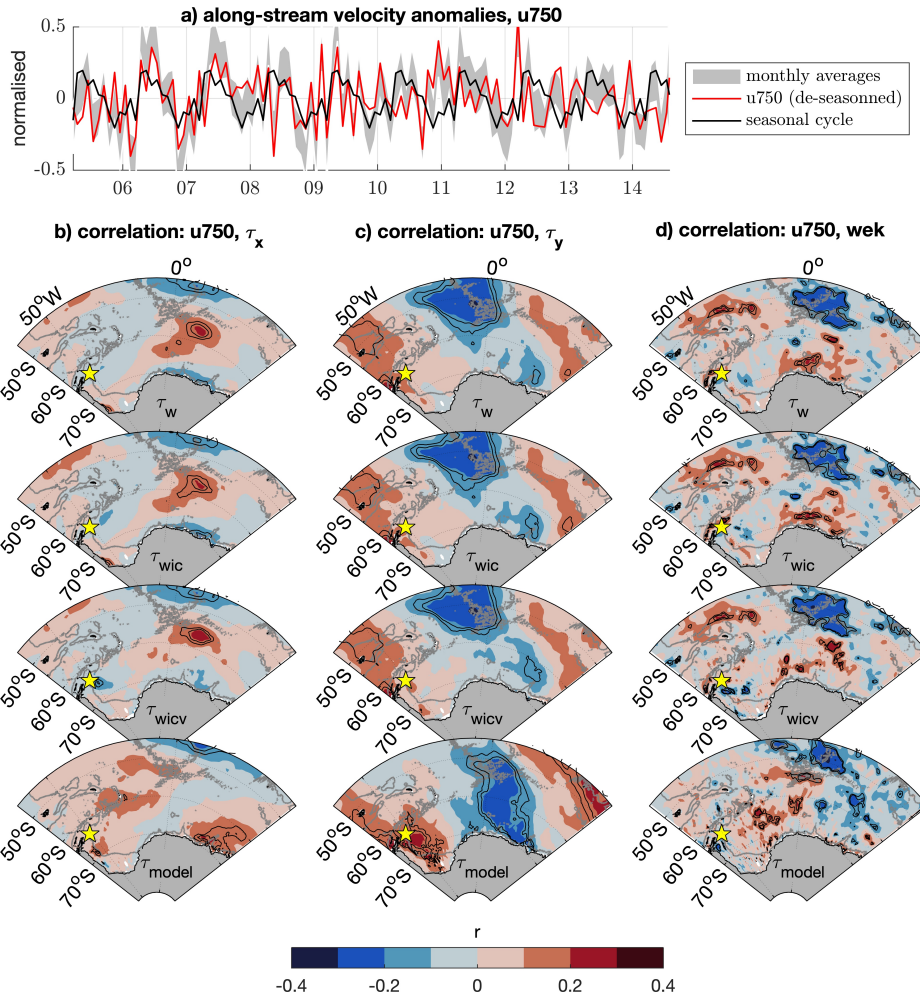


Figure 18: Same as in Figure 17 but the zero-lag correlation is made between the de-seasoned variability in velocity and surface stress (difference between monthly averages and seasonal cycle).

welling (downwelling) in the eastern inflow branch of the Weddell Gyre (and north of it in the ACC) indicates an even further upstream driver (Fig. 18.b and Fig. 18.d). This suggests that the variability in barotropic transport is indeed connected with remote forcing. In fact, Naveira Garabato et al. (2019) has already shown the connection between sea-level anomalies and circumpolar winds and our results support their discussion with in-situ observations. Also, the correlation between barotropic flow and surface stress is valid, regardless of whether or not sea-ice concentration/velocity were accounted for in the method used to calculate the surface stress. This highlights that the wind is the main driver of variability, although the sea-ice significantly modulates the surface stress locally.

### 3.5.4 *Baroclinic response to seasonal forcing*

The baroclinic variability differs at each study site, showing a larger sensitivity to local variations than for the barotropic signal. At PM, the baroclinic variations lag the barotropic velocity along the 2500 m isobath and thus, the surface stress, by 1 or 3 months, as shown by Riboni and Fahrback (2009). This time-scale is consistent with the temporal adjustment of the pycnocline slope via baroclinic instability in response to an increase in Ekman transport modulated by thermohaline forcing (Hattermann, 2018). This also confirms the probability of fast barotropic signals to propagate from this location. Downstream of PM, the seasonal cycles of velocity at the surface were weak compared to the depth-averaged signal. However, at KN, velocity records collected at the 1500 m isobath (Heywood et al., 2012) show that the top to bottom shear varied by 15 to 20 cm s<sup>-1</sup> between February and October 2010. It confirms that the baroclinic variations are stronger in this region than the ones shown by our analysis (Hattermann, 2018). In fact, our study uses velocity records at four depths over the 2500 m isobath, offshore of the sloping front. It allows for a good estimation of the depth-averaged flow speed but prevents us from capturing the seasonal baroclinic signal that is more pronounced closer to the coast. The shift in flow regime discussed in Section 3.5.1 explains the weak variability observed at AP. As the continental slope widens, the surface stress decreases, resulting in a weaker variability in temperature and velocity in the vicinity of the pycnocline depth (Figure 13 and 14).

The variability in baroclinic velocity and surface stress is not observed in the temperature variations at 200 m depth, which in fact, is not a good indicator for density variations. In the Weddell Sea, the horizontal density gradient, which determines the baroclinic variations, differs from the temperature gradient because relatively warm and salty WDW is present at intermediate depth (Fig. 12). Moreover, the variations in surface stress cannot directly relate to the temperature since it also varies seasonally as a function of the thermohaline forcing. Below 200 m depth, the density field follows the temperature, and a seasonal cycle is captured at several locations (Fig. 13, solid blue lines). This suggests that a common mechanism could explain the baroclinic fluctuations at depth. Using an idealised 2-layer model, Su et al. (2014) showed that the gyre-scale surface stress in balance with the across-slope eddy flux triggers

the seasonal oscillations of isopycnals at AP. The authors also show that the phase of these oscillations depends on the isopycnal slope, which varies across-slope. Except for the amplitude, the solution of Su et al. (2014) is valid for any outcropping isopycnal. This could explain why a seasonal signal is observed at the different locations and depths, and how its phase depends on the mooring location. The baroclinic seasonal response associated with the coastal propagation of Kelvin-Rossby waves could also explain these fluctuations. However, warming (cooling) at the subsurface related to the propagation of negative (positive) SLA discussed by Spence et al. (2017) on interannual time scales is not clear on seasonal time scales. In fact, the seasonal cycle of temperature at 200 m is decorrelated from the variability in SLA. Additionally, the variations downstream of FRIS can be controlled by the local adjustments of the flow to the surface forcing and the export of dense water from the ice shelves (Gordon et al., 2010; Meredith et al., 2011; Van Caspel, 2016; Wang et al., 2012), explaining the maximum velocity observed at the bottom in autumn. In the end, the baroclinic adjustments remain unclear and high-frequency current meters overlapping in time need to be deployed within the slope front to estimate the along-slope propagation of the signal. Observations on the western continental shelf are also required to understand the variability in the dense plume and isolate its main drivers.

### 3.6 SUMMARY

Past studies show that the boundary current system in the Weddell Sea contributes to both the export of deep and bottom waters toward lower latitudes and the flow of WDW towards the Filchner Ronne Ice Shelf cavities. Although the seasonality along the continental slope of the Weddell Sea has been investigated before at specific locations, here we present a coherent understanding of the entire boundary current system. This study combines multi-platform historical data at different locations, providing an interannual-mean view of the boundary current system and explores its adjustment on seasonal time-scales.

We confirm that the geostrophic flow reverses its interannual-mean vertical shear between KN and AP, which is characteristic for an overturning circulation forced by the dynamics on the continental shelf. The along-slope decrease in surface stress might also contribute to the shift in flow regime. A coher-

ent seasonal acceleration of the barotropic flow is observed at all sites with a maximum speed in austral autumn, associated with a coastal rise of SLA. The Comparison between the SLA and the surface stress field indicates that the barotropic flow adjusts to a momentum input on the eastern/north-eastern side of the gyre. Such teleconnection implies that changes in the surface stress field trigger a fast large-scale response in the ocean. At the tip of the Antarctic Peninsula, the barotropic flow significantly contributes to the seasonal velocity in the dense plume. Thus, by controlling the seasonal acceleration of the barotropic flow, the surface stress might remotely modulate the export of dense water from the Weddell Sea on monthly time-scales (Meijers et al., 2016).

Several methods of calculation of surface stress are compared to estimate its uncertainty, either considering the wind velocity only, accounting for the sea-ice modulation of the stress, or using sea-ice ocean model output. We find large differences in local-averages at the coast. However, the relationship between barotropic flow strength and surface stress variability on the eastern gyre is valid no matter the method. This shows that the main driver of barotropic seasonality is the wind even though sea-ice significantly modulates the surface stress in marginal ice zones. Further research integrating the contribution of the seasonal variations of buoyancy forcing at the continental shelf edge is needed to understand the seasonal baroclinic fluctuations.

## DRIVERS OF BAROCLINIC'S SEASONALITY ALONG THE CONTINENTAL SLOPE

---

The first part of this thesis consisted of providing a coherent analysis of the annual mean and seasonal changes in hydrographic properties along the Weddell Sea continental slope, using in situ observations. We confirmed the along-slope densification of the boundary current system (BCS) and found a decrease in baroclinic variability downstream of the dense water formation region. Our analysis suggested that the along-slope decrease in surface stress and the widening of the continental shelves can explain part of the changes in baroclinic properties along the continental slope. This Chapter challenges this assumption.

### 4.1 INTRODUCTION

The density overturning that occurs on the Weddell Sea's continental shelves is indicated by a change in baroclinic properties along the Weddell Sea continental slope, i.e. in the BCS (Fig. 4). These changes are characterised by a shift in density regime between the fresh shelf region, in front of the narrow eastern's continental shelves (from 30°E to 25°W) and the dense shelf region, in front of the wide south-western's continental shelves (from 25°W to the tip of the Antarctic Peninsula, Thompson et al., 2018). In front of the narrow continental shelves, the predominantly easterly winds sustain a coastal downwelling of surface water, which is counteracted by the growth of frontal instabilities. The latter drives the cross-slope transport of density through eddies, balancing the coastal downwelling. This balance maintains a density front between the deep ocean and the BCS (Nøst et al., 2011), which characterises the fresh shelf regime (Thompson et al., 2018, Fig 4). In front of the wide continental shelves, the dense water formed on those continental shelves creates a secondary front of density, which separate the cold and salty shelf water from the relatively warmer and fresher water advected from the fresh shelf region. This result in

a distinctive V-shaped front (Gill, 1973), in the vicinity of which frontal instabilities grow (Stewart and Thompson, 2016). Additionally, the formation of dense shelf water sustains a dense water outflow, which modulates the transport of mWDW towards the continental shelves (Morrison et al., 2020; Stewart and Thompson, 2015) and maintains a density overturning between mWDW and WSBW (Foster and Carmack, 1976). V-shaped front and dense water outflow characterise the dense shelf regime (Thompson et al., 2018, Fig 4).

Understanding the cross-frontal exchanges of density in the dense shelf region is primordial because they determine the amount of heat transported towards the continental shelves (Hellmer et al., 2012, 2017) and the export of dense shelf water, which fuel to the lower cell of the meridional overturning circulation (Meijers et al., 2016). Ryan et al. (2017) and Årthun et al. (2012) argued that the seasonal intrusion of mWDW observed towards the Filchner Ronne Ice shelves in austral Summer/Autumn is determined by the seasonal heaving of the mWDW in front of the Filchner Trough; the seasonal heaving being driven by the seasonally varying surface stress, the thermohaline variations above the thermocline and the melting of the ice-shelf cavities in the fresh shelf region (Hattermann, 2018; Zhou et al., 2014). Nevertheless, it is unclear if the signal propagates downstream of the Filchner Trough, i.e. in front of the southern and western continental shelves, which are the primary site of dense water formation (Foldvik et al., 2004; Huhn et al., 2008a; Nicholls et al., 2009). Moreover, we suggested in Chapter 3 that the along-slope decrease in surface stress and the widening of the continental shelves limit the downwelling of cold and fresh surface water originating from the deep ocean. It contributes to the rise of the modified Warm Deep Water (mWDW) layer along the Weddell Sea continental slope. This mechanism would imply that the off-shelf balance between Ekman and eddy overturning also reduces the cross-slope density gradient in the dense shelf region, reducing the isopycnals' tilting and thus, giving a path for the mWDW to intrude the continental shelves (Nicholls et al., 2009). Yet, it is unclear if the along-slope change in pycnocline height is rather controlled by the decrease of the coastal downwelling or the export of dense shelf water.

This chapter follows a conceptual approach to investigate baroclinic signals' advection from the fresh to the dense shelf region on seasonal time-scales. For this purpose, I developed a two-layer conceptual model, which is adapted from

Straneo (2006) and Hattermann (2018). Straneo (2006) created the Labrador Sea model to estimate the poleward heat transport associated with the along-slope densification of the boundary current through surface density flux and baroclinic instability. Hattermann (2018) included the cross-slope transport of density through Ekman transport and the seasonal variability in density to estimate the seasonal change in pycnocline height in the fresh shelf region of the Weddell Sea (Section 2.3). Combining both studies, I extend the version of Hattermann (2018) to the dense shelf region to analyse the variability in pycnocline height, i.e. mWDW layer depth, along the Weddell Sea continental slope (from  $30^{\circ}\text{E}$  to the AP, Fig.). The extended version accounts for the along-slope decrease in surface stress, the dense water formation occurring on the wide continental shelves (CS) and the cross-slope density transport associated with eddies. Because the dense water formation rate and eddy fluxes along the CS edge are poorly known, a sensitivity study is made to quantify the fluxes needed to reproduce the annual-mean change in baroclinic properties between the wide and fresh shelf region. Then, I investigate the seasonal variability in pycnocline height along the continental slope and identify the main drivers. Section 4.2 presents the observations used to set up the model. Section 4.3 presents the extended version of the model. Section 4.4 shows the model sensitivity to the different model parameters. Section 4.5 investigate the main driver of annual-mean and seasonal variability in pycnocline height along the continental slope. Section 4.6 discusses the results in relation with observations.

#### 4.2 HYDROGRAPHIC PROPERTIES OBSERVED UP- AND DOWNSTREAM THE DENSE SHELF REGION

The cross-slope Sections provided in Chapter 3 are used to represent the annual-mean difference in density and velocity between the fresh and the dense shelf region, i.e. between PM/KN and the AP (Fig. 19). Neutral density intervals are chosen based on Thompson and Heywood (2008) to highlight the presence of four water masses: the Antarctic Surface Water (AASW,  $\gamma_n < 28.1$ ), the modified Warm Deep Water (mWDW,  $28.1 < \gamma_n < 28.26$ ), the Weddell Sea Deep Water (WSDW,  $28.26 < \gamma_n < 28.4$ ) and the Weddell Sea Deep Water (WSBW,  $\gamma_n > 28.4$ ). The latter is only found at AP, downstream

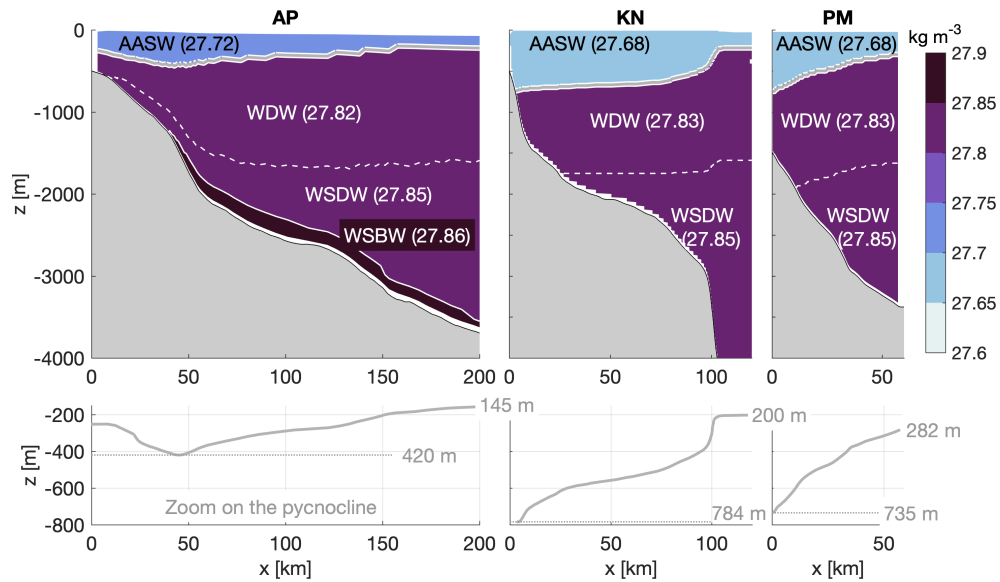


Figure 19: Upper panels) Cross-section of potential density at the AP, KN and PM. The Antarctic Surface Water (AASW), modified Warm Deep Water (mWDW), Weddell Sea Deep Water (WSDW) and Weddell Sea Bottom Water (WSBW) are separated by the neutral density surface 28.1, 28.26 and 28.4. The averaged-density of the different water masses is indicated for each section. Lower panels) Zoom on the 28.1 neutral density surface, representing the pycnocline depth.

of the CS, where bottom water forms. At PM and KN, the averaged densities above and below the pycnocline are 27.68 and 27.83-27.85 kg m<sup>-3</sup>, respectively (PM and KN, Fig. 19). At the AP, downstream the dense shelf region, the averaged densities above and below the pycnocline are 27.72 and 27.82-27.86 kg m<sup>-3</sup>, respectively (AP, Fig. 19). The difference in potential density averaged between the neutral density intervals is at least five times smaller between the mWDW, WSDW and WSBW layers than between the AASW and mWDW layers at the three study locations (Fig. 19.a). As a result, the density field can be described as a two-layer system where the layer interface shifts from a single front at PM/KN to a V-shaped front at the AP. At PM and KN, this front slopes upwards towards the open ocean, from 735-785 m depth to 200 m depth<sup>1</sup>). At the AP, the V-shaped density front slopes downwards between the shelf edge and the 1500 m isobath (from 230 m to 420 m depth) and upwards between the 1500 m isobath and the open ocean (from 420 m to 145 m depth).

The flow is surface intensified in the fresh shelf region such that two-layer approximation is also valid there (PM and KN, Fig. 20). Nonetheless, the two-layer approximation is not representative of the dense shelf region velocities as

<sup>1</sup> At PM, the mooring array only extends to the 3500 m isobath such that 284 m is not representative of the depth of the layer interface in the open ocean

they increase below the mWDW layer due to the presence of a dense water outflow of WSBW (AP, Fig. 20). A three-layer formulation is needed to model the

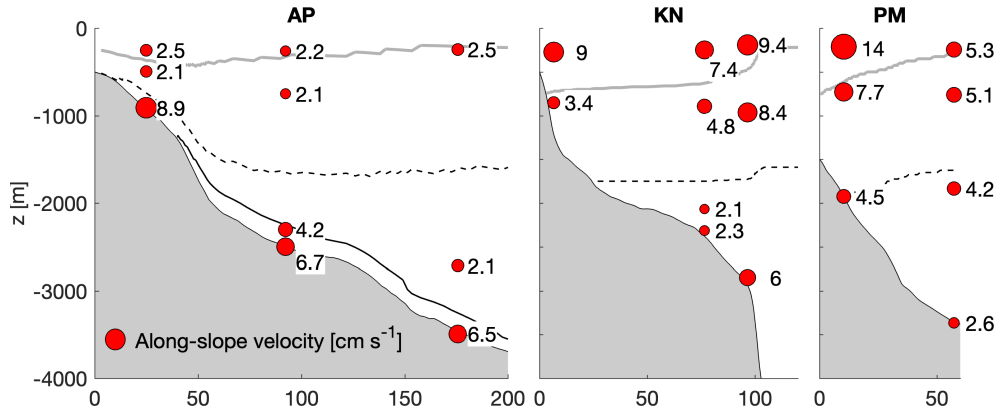


Figure 20: Along-slope velocities measured by moored current meters at the AP, KN and PM. The isolines separate the AASW, mWDW, WSDW and WSBW layers as given in Figure 19.

increase in velocity at the bottom. To achieve this formulation, one would need to parameterise for diapycnal mixing between the layers. It would significantly increase the model's complexity and, since diapycnal mixing is poorly known (Daae et al., 2019), add another degree of freedom in the system. Instead I decided to keep a two-layer formulation and focus on the variability of the pycnocline. This choice is justified because in a two-layer formulation, changes in the first layer directly impact the second layer through mass conservation (Straneo, 2006) such that diapycnal mixing does not need to be resolved.

### 4.3 TWO-LAYERS CARTESIAN MODEL

#### 4.3.1 General assumptions

The two-layers cylindrical model described in Chapter 2 (Section 2.3) is modified to include the dense shelf region downstream of KN (Fig. 3, Section 1.2). Modifications are made to simulate the cross-slope density exchange between three regions: The interior gyre (IG) and the boundary current system (BCS), already represented in Hattermann (2018, Fig. 10), and the wide continental shelves (CS), new to this study. In addition to the density exchange between the IG and the BCS, this study focuses on the density exchange between the CS and the BCS. In contrast to Hattermann (2018), the IG is considered as an open basin of infinite volume where the pycnocline depth is fixed. This assumption

is valid because the water volume in the IG is much larger than in the BCS and on the CS. The model geometry is simplified to use cartesian coordinates instead of cylindrical coordinates. Indeed, the solution is independent of the IG's geometry, and the BCS now consists of a zonal baroclinic jet that flows from east to west (along-slope) in a channel of length  $L_h$ , depth  $h_0$  and width  $W_h$ .  $W_h$  increases along the slope to represent the continental slope's widening in the dense shelf region (white area, Fig. 21). The channel shares its northern boundary with the IG and the downstream part of its southern boundary with the CS. The CS is a closed basin of width  $W_d$ , length  $L_d$  and depth  $d_0$  (CS, Fig. 21), which represents the wide continental shelves in the south-western Weddell.

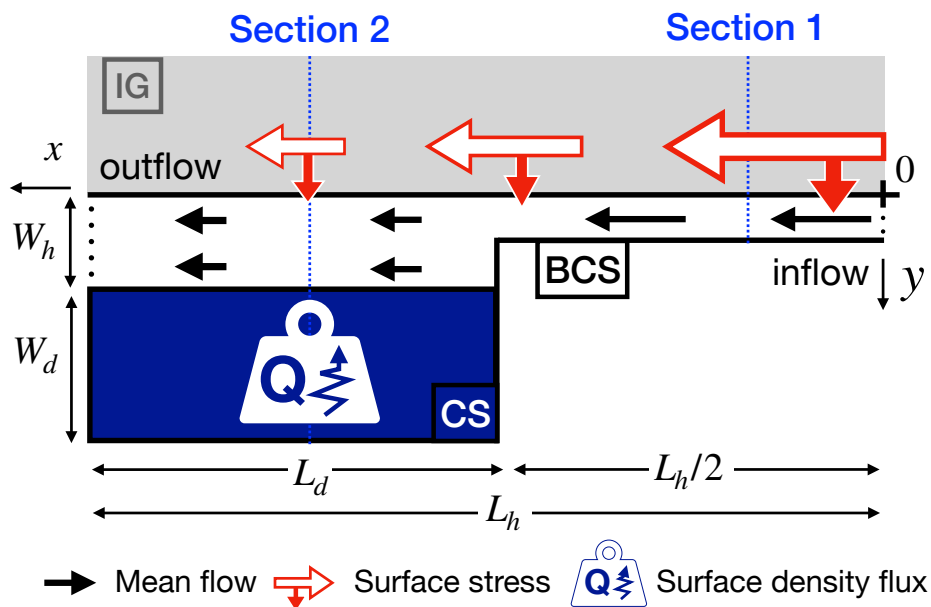


Figure 21: 2D schematic of the two-layer cartesian model used to simulate the pycnocline evolution (i.e. mWDW layer depth) along the continental slope between  $30^\circ\text{E}$  to the AP.

For the three regions, the ocean is represented by two homogeneous density layers (white and grey area in Fig. 22). The layer interface represents the neutral density surface  $\sigma_{\theta,1}$ , which defines the interface between the AASW and the mWDW (Thompson and Heywood, 2008). Three surface forcing mechanisms control the depth of the layer interface. The first is the along-slope surface stress, which controls the barotropic flow's strength (Equation 9, Section 2.3.2 in Chapter 2) and the on-shelf transport of surface water between the IG and the BCS. The on-shelf transport of surface water is in balance with the off-shelf transport of deep water associated with the bottom Ekman layer (Section

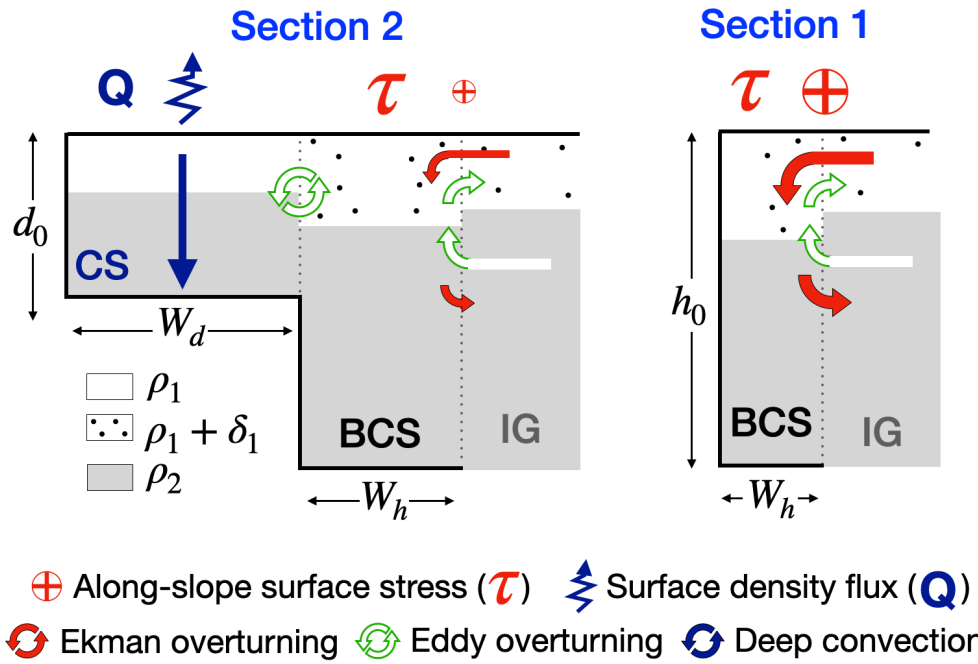


Figure 22: Cross-section summarising the processes involved in the two-layer cartesian model's density transport. The black dots represents the seasonal variations in upper layer density, occurring in the BCS and IG, exclusively ( $\delta_1$ ).

2.3.3, Chapter 2). Surface and bottom transports form an Ekman overturning cell that deepens the pycnocline in the BCS (red arrows, Fig. 22). The second is the seasonal variability in upper layer density (black dots, Fig. 22), which can be considered an indirect forcing, representing the upper layer's seasonal freshening through sea-ice melting and diapycnal mixing (Hattermann, 2018; Zhou et al., 2014). It modulates the seasonal response to the surface forcing (Section 2.3.1). Since sea-ice is present most of the year on the CS (Eayrs et al., 2019b), this variability is assumed to occur exclusively in the IG and the BCS area. The last forcing is the surface density flux, which is imposed on the CS to represent the transformation of surface water into dense water through heat loss and brine rejection (Nicholls et al., 2004; Nicholls et al., 2009). This flux drives a deep convection cell that decreases the pycnocline depth on the CS (blue arrow, Fig. 22).

The forcing mechanisms impose fluxes between the IG, BCS, and CS that introduce horizontal density gradients between the regions. These density gradients are balanced/ counteracted by two eddy overturning cells located at the BCS boundaries and centred at the interface between layer 1 and 2 (white arrows, Fig. 22). Although the seasonal variations in upper layer density  $\delta_1$  introduce a density gradient within the first layer between the BCS and the

CS (Section 2, Fig. 22), the cross-slope density exchange associated with this density gradient is assumed to be negligible. This assumption is reasonable because the density gradient between layer 1 and 2 is larger than within layer 1 ( $\partial_x \delta_1 < \partial_x \Delta_{21}$ ). A summary of the forcings and overturning processes is given in Figure 22.

#### 4.3.2 Discretisation of the pycnocline slope

The model represents a cross-slope average of ocean properties (across the  $y$ -axis) within the boundary current region for simplicity. In practice, these properties are expressed as a function of a pseudo-pycnocline slope ( $\Delta\eta/W_h$ ), representing the density gradient across the BCS. In contrast with Hattermann's model (Section 2.3), the pycnocline slope splits now into two components to represent the shift from a single density front in the eastern Weddell Sea to a v-shaped in the south-western Weddell Sea. The off-shelf slope ( $\Delta\eta_0/W_h$ ) represents the cross-slope density gradient between the BCS and the IG. The on-shelf slope ( $\Delta\eta_W/W_h$ ) represents the cross-slope density gradient between the CS and the BCS. Because we assume no flow in the IG and CS regions, both slopes are confined into the BCS area ( $u_{bc} \propto \Delta\eta/W_h = 0$  on the CS and in the IG). Consistent with Hattermann (2018), the cross-slope density gradient simply depends on the off-shelf slope upstream of the CS ( $\Delta\eta_0/W_h = 2h_1 - 2D_1$ , Fig. 23.a). In front of the CS, the cross-slope density gradient depends on the off-shelf and on-shelf slopes to represent the v-shaped front in the dense shelf region (green and blue lines, respectively, Fig. 24). On-shelf and off-shelf slopes are assumed to vary linearly across the BCS width. They rotate around a point located at mid-width and mid-depth of the slopes (green and blue dots between  $y_W$  and  $y_0$ ). When the difference in depth between the off-shelf-slope-mid-depth (on-shelf-slope-mid-depth) slope and the layer interface depth at the BCS/IG boundary (BCS/CS boundary) is null, the off-shelf slope (on-shelf slope) is flat (Fig. 37, Appendix A.7). When the difference in depth between the off-shelf-slope-mid-depth (on-shelf-slope-mid-depth) slope and the layer interface depth at the BCS/IG boundary (BCS/CS boundary) differs from 0, the off-shelf slope (on-shelf slope) starts sloping. The discretisation of the on-shelf slope is chosen such that it flattens in the absence of surface density flux on the CS (flattening of the isopycnal through baroclinic instability). In this case,

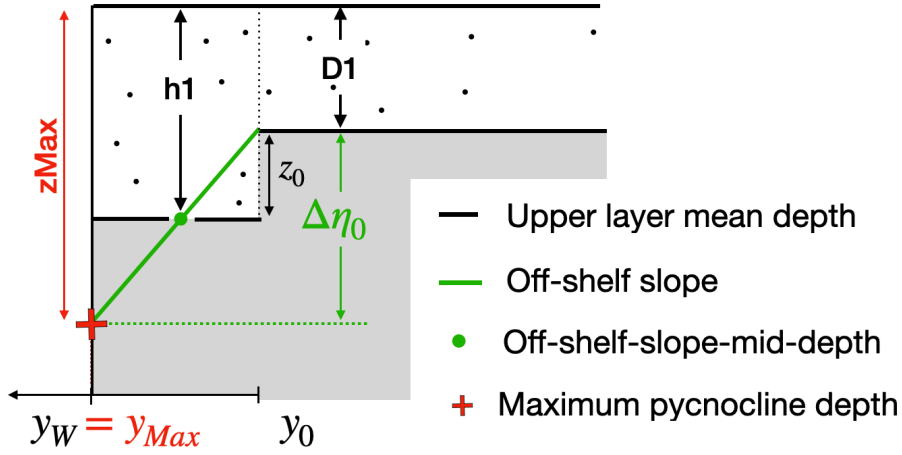


Figure 23: Representation of the pycnocline slope in the fresh shelf region.  $\Delta\eta_0 = 2(h_1 - D_1)$  represents the difference in pycnocline depth between the IG/BCS boundary (at  $y_0$ ) and the continental shelf edge (at  $y_W$ ).  $D_1$  is the upper layer thickness in the interior.  $h_1$  is the upper layer thickness in the boundary current.  $z_0 = h_1 - D_1 = \Delta\eta/2$  is the vertical distance where the cross-slope density difference between the boundary current and the interior differs from 0.

the on-shelf-slope-mid-depth matches the depth of the layer interface on the CS ( $d_1$ ) such that cross-slope density gradient is exclusively determined by the off-shelf slope (continuity between black and green line at  $y_W$  Fig. 24.a). When dense water forms ( $Q > 0$ ), the pycnocline rises on the CS, creating a difference between the maximum depth of the off-shelf slope and the depth of the layer interface on the CS (discontinuity between the black and green line at  $y_W$  Fig. 24.b). This difference in depth creates a density gradient between CS and BCS water, which triggers baroclinic instabilities along the CS edge. In turn, eddies feed the BCS of dense shelf water, decreasing the off-shelf slope's sloping. The averaged depth of the off-shelf slope (blue dot) varies as a function of the maximum depth of the on-shelf slope (blue dot and shaded green line) to relate on- and off-shelf variability. In turn, the cross-slope pycnocline slope discretises as follows,

$$\Delta\eta/W = \begin{cases} \Delta\eta_0/W_h = 2(h_1 - D_1)/W_h & \text{for } y_0 < y < y_{\max} \\ \Delta\eta_W/W_h = \xi 2(2h_1 - D_1 - d_1)/W_h & \text{for } y_{\max} < y < y_W \\ 0 & \text{otherwise} \end{cases} \quad (17)$$

where  $D_1$  and  $d_1$  are the pycnocline depth on the IG and the CS, respectively.  $h_1$  is the off-shelf-slope-mid-depth,  $2h_1 - D_1$  being the maximum depth of

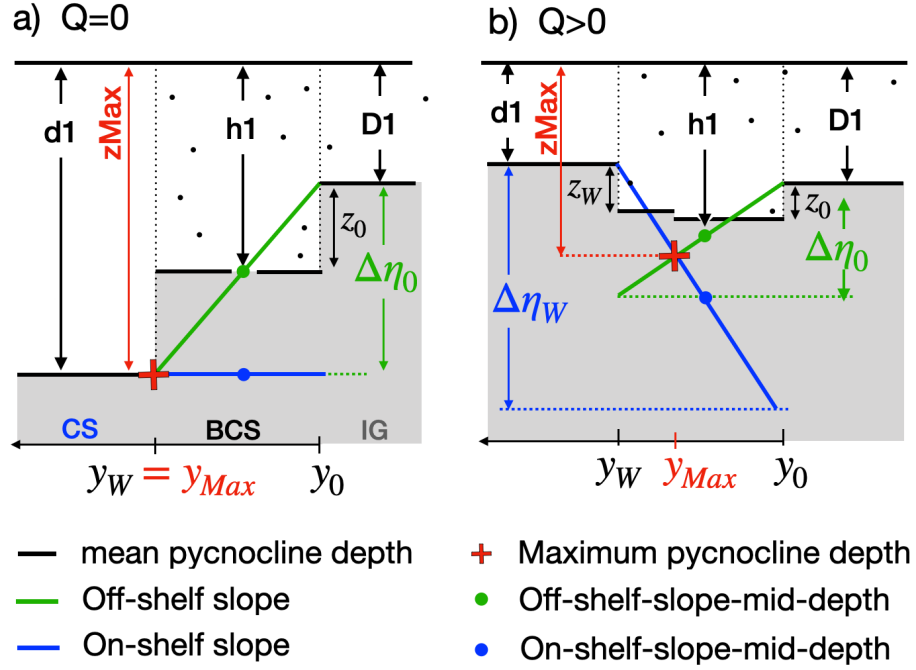


Figure 24: Representation of the pycnocline slope in the dense shelf region with and without surface density flux (plot a and b, respectively).  $y_W$  marks the boundary between the CS and the BCS.  $y_0$  marks the boundary between the BCS and the IG.  $d_1$  is the upper layer thickness on the CS.  $h_1$  is the averaged depth of the off-shelf slope in the BCS.  $D_1$  is the upper layer thickness in the IG.  $\Delta\eta_0$  and  $\Delta\eta_W$  the depth scale of the off-shelf and on-shelf slope, respectively.

the off-shelf slope ( $D_1 + \Delta\eta_0$ , Fig. 23).  $\xi$  is the wide shelf step function, representing the along-slope transition from the fresh shelf to the dense shelf region ( $\xi$  is set to 1 in front of the CS and 0 elsewhere).  $y_0$  and  $y_W$  are the IG/BCS boundary and the CS/BCS boundary, respectively.  $\Delta\eta_0 = 2(h_1 - D_1)$  and  $\Delta\eta_W = 2(2h_1 - D_1 - d_1)$  are the difference in depth between  $y_0$  and  $y_W$  for the off-shelf and on-shelf slope, respectively.  $z_{Max}$  and  $y_{Max}$  are the crossing coordinates of the off-shelf and on-shelf slope, representing the maximum pycnocline depth.  $z_{max}$  and  $y_{max}$  are geometrically derived from Figure 24 as,

$$y_{Max} = W_h - \xi W_h + \xi \frac{4h_1 - 3D_1 - d_1}{6h_1 - 4D_1 - 2d_1} W_h \quad (18)$$

and

$$z_{Max} = (1 - \xi)(D_1 - 2h_1) + \xi \left( (D_1 - h_1) \frac{4h_1 - 3D_1 - d_1}{3h_1 - 2D_1 - d_1} - D_1 \right) \quad (19)$$

Integrating Equation 17 across the BCS width and combining it with Equation 11 gives the baroclinic velocity in the BCS area,

$$U_{bc} = u_1 - u_2 = \frac{g'}{f} \left[ \frac{2(1 - \xi)(D_1 - h_1) + \xi(D_1 - d_1)}{W_h} \right] \quad (20)$$

where  $g' = \Delta\rho g/\rho_0$  is the reduced gravity, which depends on the annual-mean density difference in density between the layers  $\Delta_{21}$  and the seasonal variability in density in layer 1 (Equation 12). In the fresh shelf region ( $\xi = 0$ ),  $U_{bc}$  is proportional to the difference in layer thickness between the IG and the BCS. In the dense shelf region ( $\xi = 1$ ),  $U_{bc}$  is proportional to the difference in layer thickness between the IG and the CS.

#### 4.3.3 Parameterisation of the eddy fluxes

The eddy overturning determines cross-slope exchange of density through baroclinic instability. There exist two sources of baroclinic instability in the model: one is associated with the density gradient at the IG/BCS boundary and the other is associated to the density gradient at the CS/BCS ( $y = y_0$  and  $y = y_W$ , respectively, Fig. 24). The transport of density associated with the baroclinic instability is determined by the background potential vorticity gradient (Isachsen, 2011). For an along-slope flow of constant velocity across the slope, the background vorticity gradient is defined as,

$$\frac{\partial q}{\partial y} = \frac{\partial}{\partial y} \left( \frac{f_0}{h} \right) = -\frac{f_0}{h^2} \partial_y h \quad (21)$$

where  $q$  is the Ertel's potential vorticity.  $h$  is the thickness between the pycnocline and the continental slope and  $\partial_y h = \partial_y \eta - \partial_y H$  is the difference between the isopycnal and the continental slope, respectively. The baroclinic instability is controlled by the ratio between pycnocline and continental slope (Spall, 2004). When the continental slope opposes the pycnocline slope (prograde case), the topography acts as potential vorticity barrier and the flow is stabilised (i.e.  $\partial_y h$  is maximised in Equation 21). When the continental and the pycnocline slope have the same sign (retrograde case), the potential vorticity gradient is weaker in the lower layer (i.e.  $\partial_y h$  is minimised in Equation 21) and more instability can develop and interact with each other. The prograde case is valid at the boundary between the IG and the BCS while the retrograde

case better describes the boundary between the CS and the BCS (Fig. 4 and Fig. 22). The prograde eddy flux formulation (Spall and Chapman, 1998; Straneo, 2006) (Eq. 15) is used at both boundary to keep a fairly simple set of equations. Nevertheless, the efficiency coefficient  $c$  is parameterised differently at each boundary to account for the difference in dynamics ( $c_0$  at  $y_0$  and  $c_W$  at  $y_W$ ). Equation 15 is depth-integrated at each boundary to derive the eddy overturning in the cartesian model,

$$\int \overline{\rho'v'} dz = \begin{cases} E_0^* = c_0(\Delta_{21} - \delta_1) \frac{g'}{f} \frac{\Delta\eta_0}{W_h} z_0 & \text{at } y = y_0 \\ E_W^* = \xi c_0(\Delta_{21} - \delta_1) \frac{g'}{f} \frac{\Delta\eta_W}{W_h} z_W & \text{at } y = y_W \\ 0 & \text{otherwise} \end{cases} \quad (22)$$

where  $\Delta_{21}$  is the annual-mean difference between layer 1 and 2.  $\delta_1$  represents the seasonal variations in upper layer density (exclusively prescribed in the BCS and in the IG, section 4.3.1).  $z_0 = (|z_{\max}| - D_1)/2$  and  $z_W = (|z_{\max}| - D_1)/2$  are the vertical distance where the cross-slope density gradient differs from 0 at the BCS/IG and BCS/IG boundary, respectively (At  $y_0$   $\delta\rho(z) = \Delta_{21} - \delta_1$  for  $-D_1 > z > -D_1 - |z_{\max}|/2$  and 0 otherwise; At  $y_W$   $\delta\rho(z) = \Delta_{21} - \delta_1$  for  $-d_1 > z > -d_1 - |z_{\max}|/2$  and 0 otherwise, Fig. 24). Combining Equation 17 with Equation 22 finally gives the eddy flux at the BCS/IG and BCS/CS boundary,

$$\int \overline{\rho'v'} dz = \begin{cases} E_0^* = c_0^*(\Delta_{21} - \delta_1)(D_1 - h_1)(|z_{\max}| - D_1) & \text{at } y = y_0 \\ E_W^* = \xi c_W^*(\Delta_{21} - \delta_1)(2h_1 - D_1 - d_1)(|z_{\max}| - d_1) & \text{at } y = y_W \\ 0 & \text{otherwise} \end{cases} \quad (23)$$

where  $c_0^* = c_0 g'/(fW_h)$  and  $c_W^* = c_W g'/(fW_h)$  are the eddy growth rate at each boundary in  $s^{-1}$ . For  $\xi = 0$ ,  $\int \overline{\rho'v'} dz \propto (D_1 - h_1)^2$ , which is consistent with Hattermann (2018). The net cross-slope density transport associated with eddy fluxes is summarised in Figure 25.

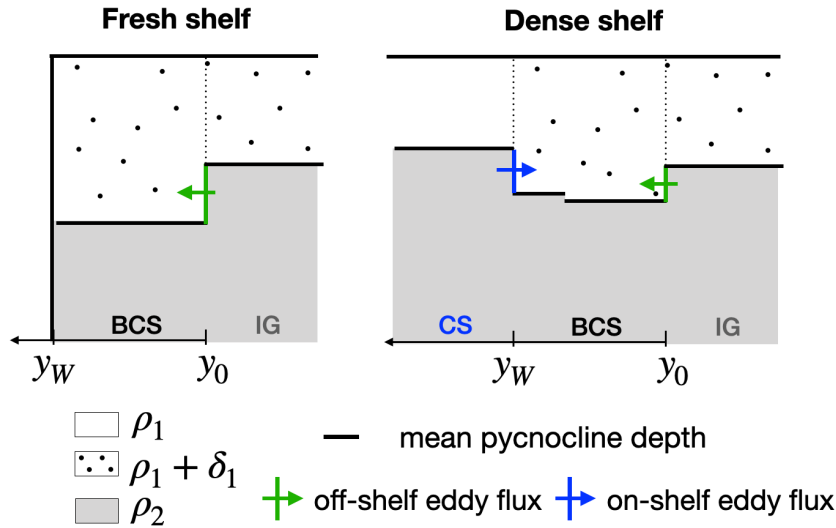


Figure 25: Eddy fluxes across the BCS boundaries in the fresh shelf and dense shelf regions.

#### 4.3.4 Prognostic equations for $h_1$ and $d_1$

The model expresses the along-slope evolution of baroclinic properties based on the density conservation averaged over the eddy time-scale (Section ??). While negligible in the eastern Weddell Sea, the surface density flux drives the formation of dense shelf water on the wide south-western Weddell Sea's continental shelves. Accounting for this flux, the density conservation averaged over the eddy time-scale becomes,

$$\begin{array}{cccccc} \partial_t \bar{\rho} & + & \partial_x (\bar{\rho} \bar{u}) & + & \partial_y (\bar{\rho} \bar{v}_e) & + & \partial_y (\bar{\rho}' v') & = & Q & (24) \\ 1. & & 2. & & 3. & & 4. & & 5. & \end{array}$$

1. Density variations
2. Along-slope transport of density by the mean flow
3. Cross-slope transport of density through Ekman overturning
4. Cross-slope transport of density through Eddy overturning
5. Surface density flux

Equation 24 is used to derive a set of prognostic equations, which define the pycnocline's variations in the BCS area and on the CS. The IG is a density reservoir of infinite volume such that the IG pycnocline depth  $D_1$  is fixed. On the CS, the surface stress is negligible such that the Ekman transport is assumed

to be null (third term in Equation 24). Also, the spatial density gradients and velocities are much larger in the BCS than on the CS. As a result, the pycnocline depth is assumed to be uniform and the mean flow to be null (second term in Equation 24). Following these assumptions, Equation 24 is integrated horizontally and vertically over the CS area and combined with equation 23 to estimate the pycnocline's variations on the CS,

$$A_d \partial_t (\rho_1 d_1 + \rho_2 d_2) = - \int_{L_d} E_W^* dx + \frac{1}{A_d} \int_{L_d} \int_{W_d} Q dx dy \quad (25)$$

where  $\rho_1$  and  $\rho_2$  are the annual-mean density in layer 1 and 2, respectively.  $d_1$  and  $d_2$  are the layer thicknesses of layer 1 and 2, respectively. The former represents the pycnocline depth on the CS. The latter is the distance between the pycnocline depth and the ocean floor.  $A_d = W_d L_d$  is the CS area and  $E_W^*$  is the eddy overturning at the CS/BCS boundary given in Equation 23. Considering that  $d_2 = d_0 - d_1$ ,  $d_0$  being the water depth on the CS, this equation simplifies to,

$$\partial_t d_1 = \frac{1}{\Delta_{21} A_d} \int_{L_d} E_W^* dx - \frac{Q_s}{\Delta_{21} A_d} \quad \text{for } \xi = 1 \quad (26)$$

where  $\Delta_{21} = \rho_2 - \rho_1$  is the annual-mean density difference between layer 2 and 1 and  $Q_s$  is the seasonal surface density flux integrated over the CS. This Equation shows that the balance between eddy overturning at the CS/BCS boundary and surface density flux determines the pycnocline's depth on the CS.

In the BCS, the density variations are dominated by the balance between Ekman and eddy overturning such that  $Q=0$ . Following this assumption, Equation 8 is vertically integrated across the BCS width and combined with Equation 23 to estimate the variations in pycnocline height along the continental slope,

$$W_h \left[ \partial_t \left( (\rho_1 + \delta_1) h_1 + \rho_2 h_2 \right) + \partial_x \left( (\rho_1 + \delta_1) v_1 h_1 + \rho_2 v_2 h_2 \right) \right] = \text{RHS} \quad (27)$$

where  $W_h$  is the continental slope width.  $h_1$  and  $h_2$  are off-shelf-slope-mid-depth and the distance between the off-shelf-slope-mid-depth and the ocean floor, respectively.  $u_1$  and  $u_2$  are the velocity in layer 1 and 2, respectively.  $\delta_1$  is the seasonal variations in upper layer density. RHS represents the cross-slope transport of density associated with balance between Ekman overturning (Eq.

14) and eddy overturning at the BCS/IG boundary and CS/BCS boundary (at  $y_0$  and  $y_W$ , respectively, Eq. 23),

$$\text{RHS} = -(\Delta_{21} - \delta_1) \frac{\tau_S}{\rho_0 f_0} - E_0^* + \xi E_W^*. \quad (28)$$

Noting that  $u_2 h_2 = U_{bt} h_0 - u_1 h_1$  (Eq. 9) and  $h_2 = h_0 - h_1$ ,  $h_0$  being the water depth in the BCS, this equation simplifies to,

$$\left[ \partial_t h_1 + \partial_x (u_1 h_1) \right] = \frac{\tau_S}{\rho_0 f_0 W_h} - \frac{E_0^*}{(\Delta_{21} - \delta_1) W_h} + \xi \frac{E_W^*}{(\Delta_{21} - \delta_1) W_h} \quad (29)$$

where  $u_1$  is derived from Equation 9 and 20,

$$\begin{aligned} u_1 &= U_{bt} + \left(1 - \frac{h_1}{h_0}\right) U_{bc} \\ &= \frac{\tau_S}{h_0 W_h} + \frac{g'}{f_0 W_h} \left(1 - \frac{h_1}{h_0}\right) \left(2(1 - \xi)(D_1 - h_1) + \xi(D_1 - d_1)\right) \end{aligned} \quad (30)$$

Using the algebraic property,

$$\begin{aligned} \partial_x (u_1 h_1) &= u_1 \partial_x h_1 + h_1 \partial_x u_1 \\ &= u_1 \partial_x h_1 + h_1 \frac{\partial u_1}{\partial x} \frac{\partial x}{\partial h_1} \frac{\partial h_1}{\partial x} \\ &= (u_1 + h_1 \frac{\partial u_1}{\partial h_1}) \partial_x h_1 \end{aligned} \quad (31)$$

Equation 29 can finally be written as,

$$\partial_t h_1 + U_{adv} \partial_x h_1 = \frac{\tau_S}{\rho_0 f_0 W_h} - \frac{E_0^*}{(\Delta_{21} - \delta_1) W_h} + \xi \frac{E_W^*}{(\Delta_{21} - \delta_1) W_h} \quad (32)$$

where

$$\begin{aligned} U_{adv} &= (u_1 + h_1 \frac{\partial u_1}{\partial h_1}) \\ &= u_1 + \frac{g'_{21} h_1}{f W_h h_0} \left(2(1 - \xi)(2h_1 - D_1 - h_0) - \xi(D_1 - d_1)\right) \end{aligned} \quad (33)$$

Equation 32 highlights that the balance between the advection of depth anomalies, the Ekman overturning, and the eddy overturning at the BCS boundaries controls the depth of the off-shelf slope in the BCS. Note that the eddy flux at the BCS/CS boundary is null in the fresh shelf region ( $\xi = 0$ ).

#### 4.3.5 *Input parameters and boundary conditions*

Equation 26 and 32 form a set of two coupled nonlinear equations with two unknowns:  $d_1(t)$  and  $h_1(x, t)$ . The numerical methods described in Hattermann (2018) and Straneo (2006) are used to calculate  $h_1$  and  $d_1$  and diagnose maximum pycnocline depth  $z_{Max}$  at each time-step. Except for the seasonal analysis where sensitivity tests on the BCS width are made, the BCS width is set to 80 km upstream of the CS (Hattermann, 2018) and 200 km in front of the CS to represent the along-slope widening of the BCS (Chapter 3). The BCS length is set to 4000 km to represent a continental slope that extends from  $30^\circ\text{E}$  to the AP (Fig. 3, Section 1.2). The CS length and width are set to 2000 km and 400 km to represent a dense shelf region that extends from  $25^\circ\text{W}$  to the AP. The CS starts at  $x = L_h/2$  (Fig. 21), where the wide shelf step function  $\xi$  switches from 0 to 1. The average water depths on the CS and in the BCS are set to 500 and 2250 m, respectively, to represent a continental shelf break that slopes from 500 m to 4000 m depth. Annual-mean density in layer 1 and 2 are chosen to be representative for the cross-sections given in Figure 19. The model does not represent the along-slope densification of the surface layer ( $28.68 \text{ kg m}^{-3}$  at PM/KN and  $28.72 \text{ kg m}^{-3}$  at the AP) such that  $\rho_1$  varies between  $1027.68 \text{ kg m}^{-3}$  and  $1027.72 \text{ kg m}^{-3}$ , depending on the experiment. The averaged density below the pycnocline is constant along the slope such that  $\rho_2$  is set to  $1027.84 \text{ kg m}^{-3}$ . The efficiency coefficient  $c_0$  is tuned to reproduce a maximum pycnocline depth of 780 m depth, which characterises the fresh shelf region (KN, Fig 19). The efficiency coefficient  $c_W$  can vary between 0 and 0.04 depending on the experiment to account for the eddy flux uncertainty over retrograde slope (Section 4.3.3).

The model predicts the temporal variations of the pycnocline as a function of three surface forcings: the seasonal variability in upper layer density ( $\delta_1$ ), the seasonal variability in surface stress ( $\tau_S$ ) and the seasonal variability in surface density flux ( $Q_S$ ).  $\delta_1$  represents the accumulation of melted freshwater transported by the wind in the vicinity of KN in summer (panel a1 and a2, Fig. 26). These changes are assumed to be uniform in space and confined in the BCS, implying that the sea-ice melting cycle occurs in phase along the BCS and do not affect the CS. This hypothesis allows investigating the seasonal modulation of the surface stress by the seasonal variability in the upper layer along

the continental slope.  $\tau_S$  represents the along-slope surface stress derived in

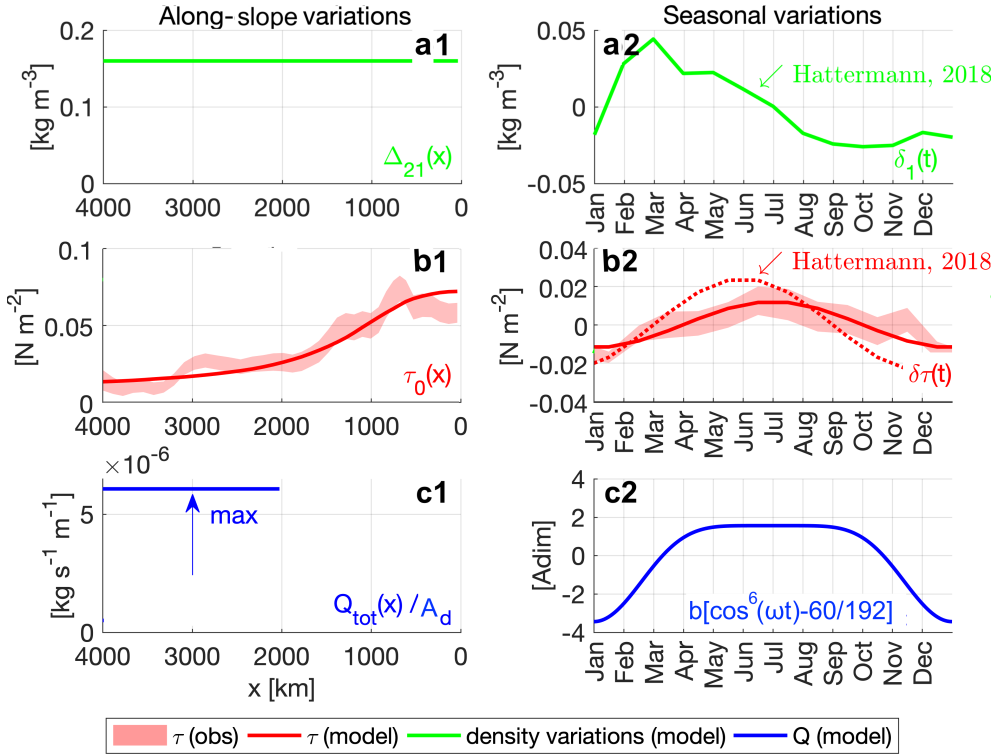


Figure 26: Along-slope and seasonal anomalies of the model forcings. a1) Along-slope variability in upper layer density in the model. a2) Seasonal anomalies in upper layer density in the model, matching the seasonality observed at KN (Hattermann, 2018). b1) Comparison between the along-slope decrease in surface observed in Chapter 3 (shaded area) and the variability in the model (solid line). b2) Comparison between the seasonal anomalies observed in Chapter 3 (shaded area), the seasonal anomalies in the model (solid line) and the seasonal anomalies in Hattermann (2018) (dashed-line). c1) Along-slope surface density flux in the model. c2) Seasonal anomalies in surface density flux in the model.

Chapter 3. Even though the amplitude of annual-mean surface stress decreases along the continental slope, the seasonal anomalies vary are uniformly along the slope (blue line, Fig. 15). In turn,  $\tau_S$  is defined as,

$$\tau_S(x, t) = \tau_0(x) + a_3 \cdot \sin(\omega t + \phi) \quad (34)$$

where  $\tau_0(x)$  is the annual-mean surface stress (panel a1, Fig. 26),

$$\tau_0(x) = a_1 \cdot \exp(-x^2/\lambda^2) + a_2 \quad (35)$$

$\lambda$  is the decrease length scale.  $a_1 = 0.06$  sets the amplitude of the decrease, and  $a_2 = 0.012$  is the minimum surface stress at AP.  $a_3 = 0.012$  sets the amplitude of the seasonal variations and  $\phi = 3\pi/2$  determines their phase. The reason

why the surface stress phase differs from Hattermann (2018) is discussed in section 4.6.1.  $Q_S$  represents the density input associated with ocean heat loss and brine rejection. On the CS, the flux of density is a maximum between May and September, corresponding to the winter period when sea-ice production is maximum (Paul et al., 2015). In turn,  $Q_S$  is defined as,

$$Q_S(t) = Q_0 \left( 1 + b \cdot [\cos^6(\omega t) - 60/192] \right) \quad (36)$$

where  $Q_0 = \int_{A_d} Q dA_d$  is the annual-mean density flux integrated over the CS, and  $b$  sets the seasonal variations' amplitude.  $Q_0$  can vary between 0 and  $10 \times 10^5 \text{ kg s}^{-1}$  depending on the experiment to account for the uncertainty on the dense water formation rate, occurring on the CS (panel c1, Fig. 26). The upper bound is approximately 1.5 times the upper value given in (Stewart and Thompson, 2015). Realistic simulations suggest the seasonal variability is ten orders of magnitude larger than the annual-mean flux (Stulic, personal communication). In turn,  $b$  is set to 10 as a first-order approximation. As a result, the seasonal anomalies are minus four times the mean value in January/December and one time the mean value between May and September (panel c2 in Fig. 26), which implies a net density flux of two times the mean value in between May and September and minus three times the mean value in January/December (the net flux is the sum of the annual mean flux and the seasonal anomalies).

Finally, boundary conditions for the IG pycnocline's depth  $D_1$  and the off-shelf-slope-mid-depth at the inflow  $h_1(0, t)$  are specified to solve the set of prognostic equations. Neglecting the variations in the interior gyre, the pycnocline depth  $D_1$  is fixed to 200 m depth (Fig. 19). A Neumann boundary condition is prescribed at the BCS inflow ( $\partial_x h_1 = 0$  at  $x=0$ ), allowing the pycnocline to vary as a function of the balance between Ekman and the eddy overturning, independently of the initial condition. Table 1 summarises the constants and forcing parameters that need to be specified for the solution. The table also includes the parameters calculated by the model (variables).

Parameters and constants	Symbol	Unit	Value
Coriolis force	$f$	$s^{-1}$	$-1.4 \cdot 10^{-4}$
gravity	$g$	$m s^{-2}$	9.81
BCS width	$W_h$	km	80 to 200
BCS length	$L_h$	km	4000
BCS water depth	$h_0$	m	2500
CS width	$W_d$	km	400
CS length	$L_d$	km	2000
CS area	$A_d$	$m^2$	$L_d W_d$
CS water depth	$d_0$	m	500
IG pycnocline depth	$D_1$	m	200
Wide shelf step function	$\xi$		0 or 1
Reference density	$\rho_0$	$kg m^{-3}$	1027
Annual-mean density in layer 1	$\rho_1$	$kg m^{-3}$	1027.68 to 1027.72
Seasonal variations in layer 1	$\delta_1(t)$	$kg m^{-3}$	[H., 2018]
Annual-mean density in layer 2	$\rho_2$	$kg m^{-3}$	1027.84
Efficiency coefficient at $y_0$	$c_0$		0.02 to 0.025
Efficiency coefficient at $y_W$	$c_W$		0 to 0.04
Annual-mean surface stress	$\tau_0(x)$	$N m^2$	[Eq. 35]
Time-varying surface stress	$\tau_S(x, t)$	$N m^2$	[Eq. 34]
Annual-mean density flux	$Q_0 = \int_{A_d} Q d$	$kg s^{-1}$	0 to $1 \cdot 10^5$
Time-varying density flux	$Q_S(t)$	$kg s^{-1}$	[Eq. 36]
Annual-mean volume transport	$T_0$	Sv	11.5
Time-varying volume transport	$T_S$	Sv	[Eq. ??]
Variables	Symbol	Unit	Value
CS pycnocline depth	$d_1$	m	
Off-shelf-slope-mid-depth	$h_1$	m	
Maximum pycnocline depth	$z_{Max}$	m	[Eq. 19]
BCS upper layer velocity	$u_1$	$m s^{-1}$	[Eq. 30]
Eddy flux at $y_0$	$E_0^*$	$kg s^{-1}$	[Eq. 23]
Eddy flux at $y_W$	$E_W^*$	$kg s^{-1}$	[Eq. 23]

Table 1: Model constants, parameters and variables

## 4.4 MODEL SENSITIVITY

## 4.4.1 Sensitivity parameters

Before investigating the fluxes needed to change the pycnocline height along the continental slope, one needs to determine the solution's sensitivity to the different parameters. For this purpose, a scaling analysis is performed. Using the steady state ( $\partial_t = 0$ ) of Equation 26 and 32, I derive two scaling relations that describe the annual-mean difference in off-shelf slope-mid-depth along the continental slope,

$$\Delta h_1^* = \frac{1}{U_1^* W_h} \left[ L_h U_e + L_h W_h \frac{g c_0 \Delta \rho}{\rho_0 f} \left( \frac{\Delta \eta_0^*}{W_h} \right)^2 - \frac{Q_{\text{tot}}}{\Delta \rho} \right] \quad (37)$$

and the annual-mean pycnocline depth on the CS

$$d_1^* = \Delta \eta_0^* - \sqrt{\frac{Q \rho_0 f W_h}{g c_W \Delta \rho^2 L_d}}. \quad (38)$$

as a function of the constants,  $g$ ,  $f$  and  $\rho_0$ , the efficiency parameters  $c_0$  and  $c_W$  at the BCS/IG and CS/BCS boundary (Section 4.3.3), the channel length  $L_h$ , the channel width  $W_h$ , the CS length  $L_d$ , the vertical scale of the off-shelf slope  $\Delta \eta_0^*$ , the velocity scale of the along-slope flow in the upper layer  $U_1^*$  ( $U_{\text{adv}} \sim u_1$ , Eq. 33), the Ekman transport  $U_e$ , the density flux  $Q_{\text{tot}}$  and the density difference  $\Delta \rho$ . Equation 37 highlights that the overall balance between Ekman transport, eddy overturning at the IG/BCS boundary and surface density flux (1<sup>st</sup>, 2<sup>nd</sup> and 3<sup>rd</sup> term on the right-hand side of Eq. 37) determines the change in pycnocline height along the continental slope. The ratio between cross-slope transport and along-slope transport of density (the latter being represented by  $U_1^* W_h$ , in Equation 37) controls the amplitude of the along-slope change in pycnocline height: the quicker the flow is, the less efficient the cross-slope transport of density. This scaling reveals that the eddy flux at the CS/BCS boundary does not impact the along-slope change in pycnocline height, which contrasts with the time-dependent solution (Eq. 32). Indeed, in a steady-state, the eddy overturning along the CS/BCS boundary is proportional to the surface density flux ( $\int E_W^* dx \propto Q_s / \Delta_{21}$ , Eq. 26). As a result, the discharge of dense water from the CS to the BCS is independent of the eddy efficiency's parametrisation at the CS/BCS boundary  $c_W^*$ . Nevertheless,  $c_W^*$

determines the depth of the pycnocline on the CS (Eq. 38). The smaller/larger the eddy efficiency is, the thinner (thicker)  $d_1$ . In fact,  $c_W^*$  determines eddies' efficiency in transporting dense water across the BCS/CS boundary. At low eddy efficiency, the newly formed dense water tends to remain on the CS, lifting the pycnocline on the CS and decreasing the upper layer's thickness. At large eddy efficiency, the newly formed dense water tends to flow out from the CS, lowering down the pycnocline on the CS and increasing the thickness of the upper layer. In turn,  $c_W^*$  modulates the difference in pycnocline height between the CS and the BCS such that the net transport of density between the CS and the BCS remains proportional to the surface density flux.

Considering the model geometry, the barotropic flow strength and the Ekman transport to be fixed parameters, one can identify two numbers that determine the along-slope change in off-shelf-slope-depth  $\Delta h_1$  and pycnocline depth on the CS  $d_1$ : the dense water formation rate  $Q^* = Q/\Delta\rho$  and the eddy growth rate at the CS/BCS boundary  $c_W^* = c_W g \Delta\rho / (f W_h \rho_0)$  (Eq. 37 and 38). To understand the relationship between  $\Delta h_1$ ,  $d_1$ ,  $Q^*$  and  $c_W^*$ , cross-sensitivity tests are performed, varying  $Q_{tot}$ ,  $\Delta\rho$  and  $c_W$ . The eddy growth rate at the BCS/IG boundary  $c_0^* = c_0 g \Delta\rho / (f W_h \rho_0)$  is fixed to  $3 \times 10^{-6} \text{ s}^{-1}$  to reproduce a maximum pycnocline depth of 780 m, representing the eastern Weddell Sea's fresh shelf regime (KN, Fig. 19). The relationship between  $Q^*$  and  $\Delta h_1$  is linear (Fig. 27.a): consistent with the observation made in the previous paragraph, the more efficiently dense water forms, the larger the rise of the off-shelf slope. Interestingly,  $\Delta h_1$  is also sensitive to  $c_W^*$  even though this term does not appear in Equation 37. For instance, for a dense water formation rate of 0.4 Sv, the absolute value of  $\Delta h_1$  decreases from 110 to 80 m, increasing  $c_W^*$  by a factor of 2 (isoline indicated by the arrow, Fig. 27.b). This result highlights a non-linear relationship between the change in pycnocline height and the eddy flux at the IG/BCS boundary. Indeed,  $c_W^*$  also modulates the difference in pycnocline height between the IG and the BCS and, therefore, the eddy flux at the BCS/IG boundary ( $\Delta\eta_0^*$  in Equation 37). The data points scatter between 0 and 400 m for  $d_1$  for different values of  $Q^*$  such that there exist no clear relationship between  $\Delta h_1$  and  $Q^*$  (Fig. 27.c). Nevertheless, as expected from Equation ??,  $d_1$  adjusts quadratically to the choice  $c_W^*$ . For instance, for a dense water formation rate of  $Q^* = 0.4 \text{ Sv}$  (arrow on Figure 27.d),  $d_1$  varies between 50 m to

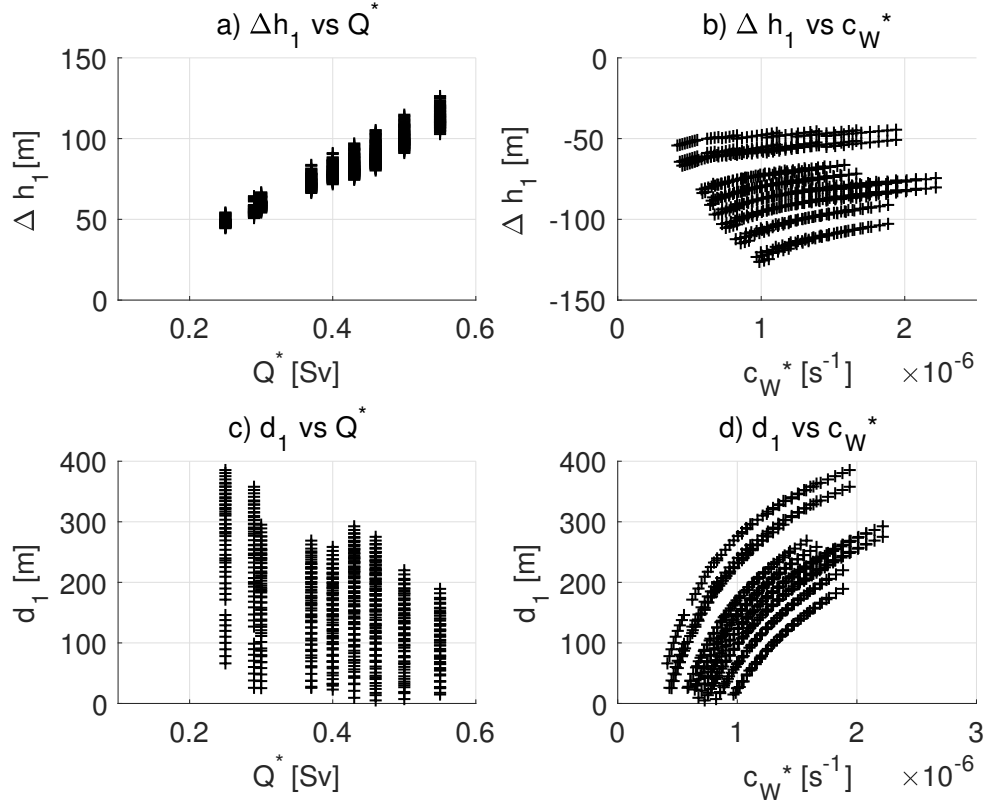


Figure 27: Sensitivity analysis of the relationship between  $\Delta h_1$ ,  $d_1$ ,  $Q^*$  and  $c_W^*$ .  $Q^* = Q_{\text{tot}}/\Delta\rho$  is the dense water formation rate.  $c_W^* = c_W g \Delta\rho / (f W_h \rho_0)$  is the eddy growth rate at the CS/BCS boundary. The data points represent  $\Delta h_1$  and  $d_1$  as a function  $Q^*$  (panel a and c) and  $c_W^*$  (panel b and d) for values of  $\Delta\rho$ ,  $Q_{\text{tot}}$  and  $c_W$ , varying between  $0.12$  and  $0.16 \text{ kg m}^{-3}$ ,  $3 \cdot 10^4$  and  $7 \cdot 10^4 \text{ kg s}^{-1}$  and  $0.005$  and  $0.035$ , respectively. The arrows in panel c and d point out the isoline  $Q^* = 0.4 \text{ Sv}$ .

300 m, increasing  $c_W^*$  by a factor of two. This result highlights that the solution on the CS is more sensitive to  $c_W^*$  than  $Q^*$ .

#### 4.4.2 Set up reproducing the BCS properties

Our sensitivity analysis reveals that the model is sensitive to the choice of dense water formation rate ( $Q^*$ ) in the BCS and the choice of the eddy efficiency at the CS/BCS boundary ( $c_W^*$ ) on the CS. Nevertheless,  $Q^*$  and  $c_W^*$  are poorly known due to the lack of observations in the dense shelf region. To better constrain the model, these fluxes are chosen to represent the change in baroclinic properties between the region up-and downstream the dense shelf region, i.e. between KN and the AP. Considering an uncertainty on the cross-section mapping of  $\pm 25 \text{ m}$  and neglecting the rise of the pycnocline associated

with the densification of the interior gyre, the change in pycnocline height in the BCS area is  $\Delta z_{\text{Max}} = (780 - 420) - (200 - 145) = 305 \pm 25$  m (KN and AP, Fig. 19). Thermal-wind derived velocities and current meter data suggests a velocity above the pycnocline ranging between 2.1 and 2.5  $\text{cm s}^{-1}$  at the AP (2-2.2  $\text{cm s}^{-1}$  for the thermal-wind derived velocity averaged above the pycnocline, not shown, and 2.1-2.5 for the moored current meter velocity, Fig. 20). Seeking a set of experiments that are representative of the along-slope shift in density regime, I select the solutions that both reproduce an along-slope rise of the pycnocline between KN and AP of  $280 < \Delta z_{\text{Max}} < 330$  m and an upper layer velocity of  $2 < u_1 < 2.5$   $\text{cm s}^{-1}$  at the AP<sup>2</sup>. These conditions are met for experiments with dense water rate  $Q^*$  of 0.3 to 0.55 Sv and an eddy growth rate at the CS/BCS boundary  $c_W^*$  of 0.6 to  $2 \cdot 10^{-6}$   $\text{s}^{-1}$  (Fig. 28). Within

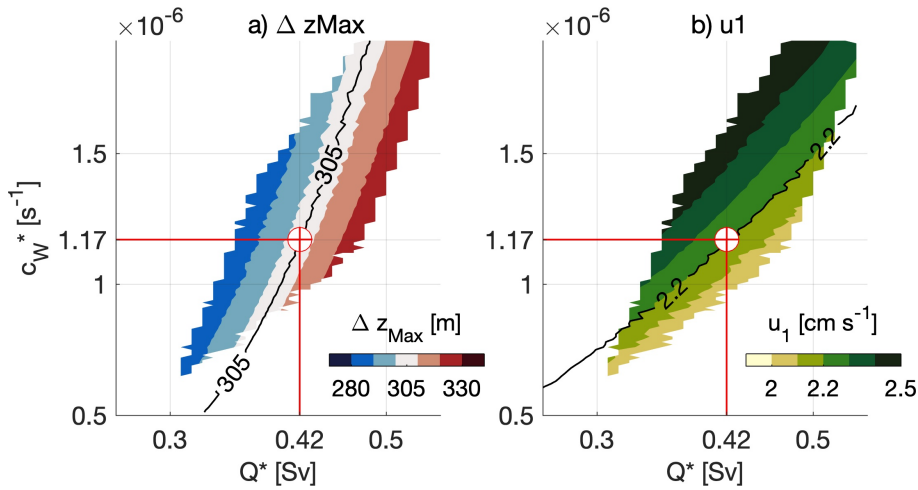


Figure 28: Sensitivity analysis on the along-slope change in pycnocline height ( $\Delta z_{\text{Max}}$ , panel a) and the upper layer velocity ( $u_1$ , panel b) for experiments representative of the along-slope shift in density regime. The color scale shows the amplitude of  $\Delta z_{\text{Max}}$  and  $u_1$ , with contour interval of 10 m and 0.1  $\text{cm s}^{-1}$ , respectively. The red cross highlights the optimised setup used for the seasonal analysis.

that ranges, the relationship between  $Q^*/\Delta z_{\text{Max}}$  and  $Q^*/u_1$  is linear (Fig. 28.a and 28.b, respectively). For a small/large value  $Q^*$ ,  $c_W^*$  must be relatively small/large to represent the along-slope change in pycnocline height and the velocity in the upper layer. However, the coefficient of proportionality between  $Q^*$  and  $\Delta z_{\text{Max}}$  differs from  $Q^*$  and  $u_1$  (divergence between the  $\Delta z_{\text{Max}} = 305$  m isoline and the  $u_1 = 2.2$   $\text{cm s}^{-1}$  isotach for large value of  $Q^*$ , Fig. 28). The setup that reproduces the best the along-slope rise of the pycnocline between

<sup>2</sup> Velocities below the pycnocline are inferred through mass conservation and through thermal wind balance.

KN and the AP and, the velocity above the pycnocline at the AP, is found for  $Q^* = 0.42 \text{ Sv}$   $c_W^* = 1.17 \cdot 10^{-6} \text{ s}^{-1}$  (red cross, Fig. 28.a and 28.b).  $Q^* = 0.45 \text{ Sv}$  is consistent with the findings of Pellichero et al. (2017), which estimated an averaged dense water formation rate of  $1.5 \cdot 10^{-12} \text{ Sv m}^2$  over the Southern and western Weddell Sea's continental shelves, implying a net transport of  $0.45 \text{ Sv}$  for a CS area of  $3 \cdot 10^{11} \text{ m}^2$ . Although the eddy flux cannot directly be linked with observations nor regional modelling study<sup>3</sup>, the eddy growth rate at the CS/BCS and IG/BCS boundaries have the same order of magnitude for all realistic setups ( $c_W^*$  is 0.4 to 1.8 times  $c_0^*$ , not shown), suggesting that the model correctly scales the eddy fluxes.

#### 4.5 MECHANISMS DRIVING THE PYCNOCLINE HEIGHTS' SEASONALITY

Gaining some confidence in the model estimates, I investigate the drivers of annual-mean and seasonal changes in pycnocline height along Weddell Sea's continental slope. The fraction of  $\Delta z_{\text{Max}}$  associated with  $Q^*$  shows how much of the annual-mean difference in pycnocline height is associated with the export of dense water from the CS (Fig. 29). There exist a relation of proportionality between the dense water formation rate  $Q^*$  the along-slope increase in  $\Delta z_{\text{Max}}$  (grey and coloured dots). The larger  $Q^*$  is, the larger the fraction of along-slope change in pycnocline height associated with cross-slope density transport along the CS/BCS boundary. In fact, the more the pycnocline rises (red dots, Fig. 29), the weaker the density gradient between the IG and the BCS. As positive feedback, the cross-slope density transport along the IG/BCS boundary decreases, increasing the contribution from  $Q^*$  in changing the pycnocline height along the slope. The contribution of  $Q^*$  varies between 76 % to 89 % for the experiments representative of along-slope changes in baroclinic properties observed between KN and PM (coloured dots, Fig. 29). The optimised setup reproducing the along-slope rise of the pycnocline between KN and AP and the velocity above it at the AP suggests that the export of dense water from the CS determines 84 % of the along-slope rise (red cross in Fig. 29). This result is consistent with an along-slope shift in density regime determined by dense shelf water formation. The remaining variability is associated with changes in the balance between surface stress and eddy overturning along the

<sup>3</sup> The eddy field non-linearly varies as a function of local density fronts (Vallis, 2017), which the two-layer cartesian model does not resolve.

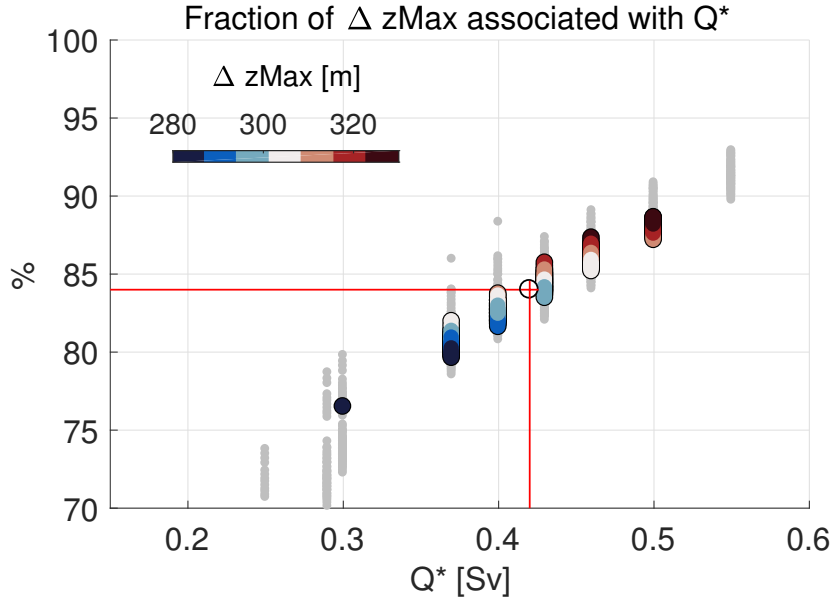


Figure 29: Fraction of the along-slope change in pycnocline height associated with the export of dense water from the CS to the BCS. The grey dots show the sensitivity analysis experiments (Fig. 27). The coloured dots highlight the experiments, reproducing the along-slope rise of the pycnocline between KN and AP and the velocity above the pycnocline at the AP ( $280 < \Delta z_{Max} < 330$  m and  $2 < u_1 < 2.5$  cm s<sup>-1</sup>). The colour scale shows the along-slope change in pycnocline height with contour intervals of 10 m. The red cross shows the value suggested by the optimised setup.

IG/BCS boundary, accounting for 16% of the along-slope change in pycnocline height.

The solution is too sensitive to the choice of  $c_W^*$  to investigate the seasonal variations on the CS ( $\pm 15$  m of  $d_1$  for a change of 1% in  $c_W^*$ ). In turn, the optimised setup shown in Figure 28 is used to investigate the seasonal variability in the BCS area. Since the seasonal anomalies in upper layer velocity vary within the observation's range of uncertainty (not shown), I focus on the seasonal anomalies in pycnocline's height along the continental slope ( $\pm 0.5$  m of  $z_{Max}$  for a change of 1% in  $c_W^*$ ). To investigate the main drivers of variability, I perform twelve experiments (Fig. 30), alternatively setting on and off: the widening of the continental slope in front of the CS ( $W_h(x)$ ), the eddy flux between CS and the BCS ( $E_W^*$ ), the seasonal variations in surface stress ( $\tau_S$ ), the seasonal variations in the upper layer density ( $\delta_1$ ) and the seasonal variability in surface density flux ( $Q_S$ ). First, I investigate how the widening of the BCS affects the downstream propagation of baroclinic anomalies, i.e. setting the CS/BCS eddy flux to 0. For a continental slope of uniform ( $W_h = 80$  km, panels a in Fig. 30), the amplitude of the variations driven by the seasonal

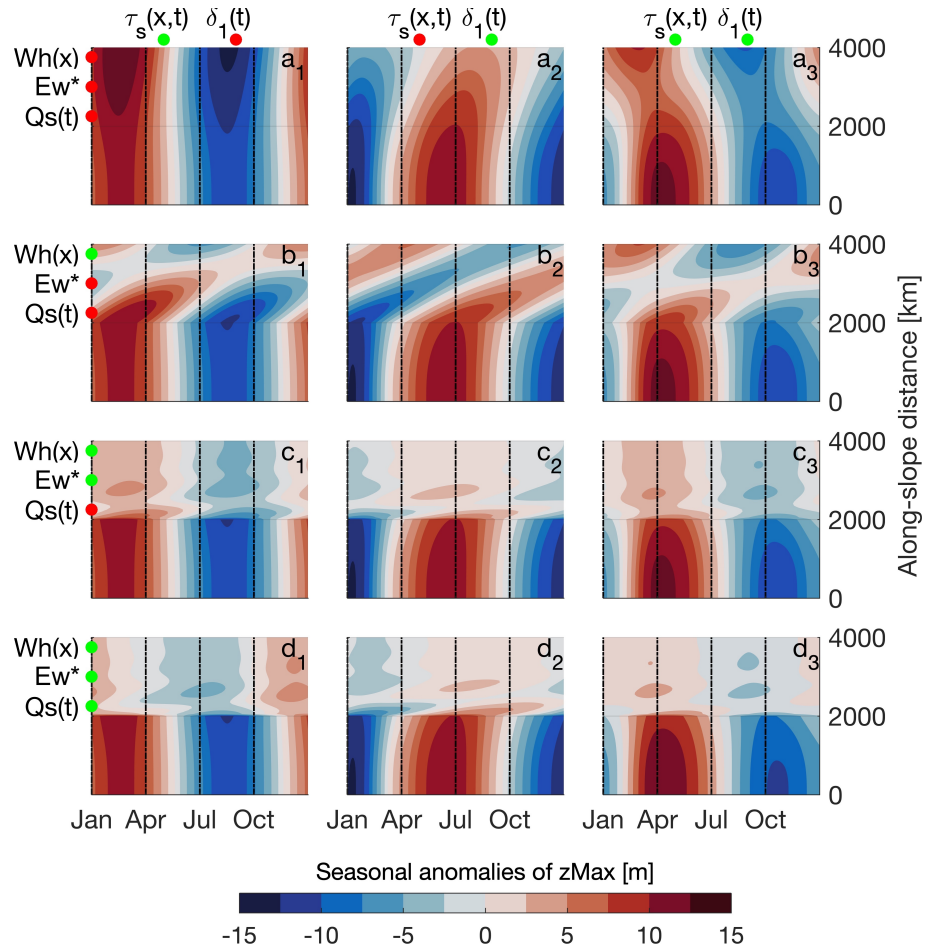


Figure 30: Hovmüller diagrams illustrating the pycnocline height's seasonal anomalies within the BCS. X-axis: seasonal variations. Y-axis: along-slope distance. Twelve experiments are made setting on/off the widening of the continental slope,  $W_h(x)$ , the density exchange between the CS and the BCS  $E_w^*$ , the seasonal variations in surface stress,  $\tau_s(x, t)$ , the seasonal variations in upper layer density,  $\delta_1(t)$ , and the seasonal variations in surface density flux,  $Q_s(t)$ . Red dot: parameter off. Green dot: parameter on.  $Q^*$  is set to  $0.42 \text{ Sv}$  and  $c_w^*$  to  $1.17 \cdot 10^{-6} \text{ s}^{-1}$ . The fresh and dense shelf regions extend from 0 to 2000 km and from 2000 to 4000 km, respectively.

surface stress increases along the slope (panel a1). In September (March), the pycnocline rises (deepens) by 10 m at  $x=0$  km instead of 15 m at  $x=4000$  km. The amplitude of the variations driven by the seasonal variability in upper layer density decreases from 10 m to 5 m along the slope with a two-months phase shift along the continental slope (panel a2). The combination of seasonal surface stress and seasonal variations in upper layer density amplifies and modulates the phase of the oscillation of  $z_{\text{Max}}$  (panel a3). As a result, the pycnocline rises (deepens) in May (November) in the fresh shelf region (upstream of  $x=2000$  km) and in March (September) downstream of the dense shelf region (at  $x=4000$ ). The widening of the continental slope in front of the

CS significantly impacts the phase and the amplitude of seasonal variability along the slope (panels b in Fig. 30). No matter the forcings, a pronounced phase-shift of the seasonality is found between 2000 km and 4000 km for a continental slope that widens from 80 km to 200 km at  $x=2000$  km. Also, the amplitude of the seasonal variations decreases from 20-30 m at  $x=2000$  km to 10 m at  $x=4000$  km. This result highlights that the continental slope's width controls the phase and the amplitude of the seasonality along the slope.

Figure 30.c illustrates how the eddy flux along the CS edge affects the seasonal variability in the dense shelf region ( $E_W^* \neq 0$ ). There exist a significant dampening of the seasonality between 2000 and 4000 km, no matter the surface forcing ( $Q_s = 0$ , 30.c). For instance, the anomalies driven by the seasonal surface stress vanish at  $x = 2200$  km (panel  $c_1$  30), suggesting that the exchange at CS boundary rapidly diffuses the upstream variability. Also, compared to panel a and b, the seasonal anomalies are more uniform in time (panels  $c_1$  and  $c_2$  30). As the upstream variability diffuses along the CS edge, the local variations in surface stress become the primary driver of variability (no seasonality associated with the change in upper layer density, Fig. 30.c2). The seasonal variations in surface density flux ( $Q_s \neq 0$ ) slightly modulate the seasonality in pycnocline height in front of the CS (between 2000 and 4000 km, panels d in Fig. 30). Their phase shifts towards summer, and their amplitude decrease to minimum values of 2 to 8 m at 4000 km. Nevertheless, the amplitude of the modulation is negligible compared to the along-slope dampening of the seasonal variability.

In the end, our analysis suggests that the widening of BCS along the continental slope and the eddy flux along the CS edge significantly dampens the baroclinic signals advected from the fresh shelf to the dense shelf region. Model output and observations are compared in the discussion to assess the robustness of these results.

## 4.6 DISCUSSION

### 4.6.1 *Seasonal anomalies in pycnocline height along the continental slope*

The model-inferred variability in the fresh shelf region is consistent with the one described in Hattermann (2018): the pycnocline rises (deepens) in summer

(winter), and the change in upper layer density both amplifies and delays the phase of the seasonal variations (Fig. 30). However, the pycnocline is shallowest in May (panels a3, b3, c3 and d3), two-month later than the model results from Hattermann (2018). Instead of using the gyre-scale wind stress, which is maximum in June (Su et al., 2014), this study uses the surface stress modulated by the sea-ice drift and averaged over the continental slope, which is maximum in July (Fig. 26). Also, instead of prescribing the pycnocline depth at the inflow, the pycnocline varies freely as a function of the local forcing such that the delay between surface forcing and maximum pycnocline height is uniform within the fresh shelf region. As a result, the minimum pycnocline depth (or maximum pycnocline height) occurs later in the year. Although our analysis neglects the contribution of freshwater fluxes associated with the basal melting of ice shelf cavities, these fluxes would phase-shift the maximum pycnocline height towards winter by a month (Hattermann, 2018). As a result, the pycnocline (i.e. the mWDW layer) would be highest in April, phasing the maximum temperature observed at the shelf edge of the Filchner trough between 2007 and 2009 (Årthun et al., 2012). It strengthens the argument that the combination between surface stress, surface freshwater fluxes, and basal melting determines the mWDW layer's depth in the fresh shelf region (Hattermann, 2018; Riboni and Fahrbach, 2009; Zhou et al., 2014).

The seasonal analysis shows a significant dampening of the seasonal variability in pycnocline height between the fresh and the dense shelf regions (Fig 30). This dampening is associated with the widening of the continental slope and the eddy flux along the CS edge. The former reduces the flow strength between fresh and dense shelf region, slowing down the advection of density anomalies from upstream ( $U_{adv} \rightarrow 0$ , Eq. 32). The latter increases the lateral diffusivity along the CS edge. The difference in magnitude in pycnocline height's seasonality between the fresh and the dense shelf region is consistent with the along-slope decrease in temperature variability observed along the 2000-2500 isobath between PM/KN and AP (Section 3.1.2, Fig. 13.a). However, observations are generally insufficient to compare the density variations along the continental slope on seasonal time-scales (Section 3.5.4). Investigating the non-seasonal variability from individual CTD profiles, we find that the pycnocline depth is more variable upstream of the dense shelf region than downstream (PM/KN and AP, respectively). Above the 2000 m isobath, it varies by

500 m upstream of the dense water formation and 250 m at AP. Even though winter data is lacking, this suggests that an along-slope decrease in variability is also valid on non-seasonal time-scales. (Daae et al., 2017; Ryan et al., 2017; Årthun et al., 2012). Nonetheless, the difference in amplitude between model

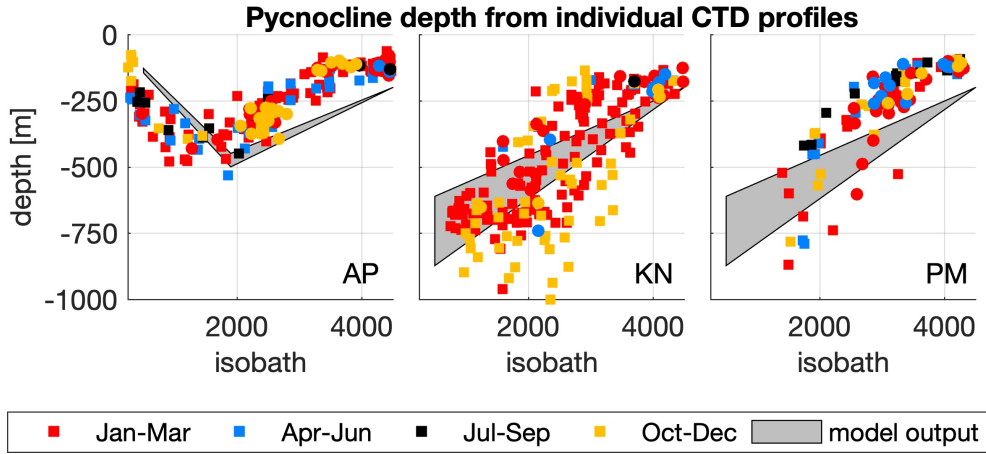


Figure 31: Across-isobath distribution of the seasonal variability in pycnocline depth (corresponding to the neutral density surface 28.1) estimated from float and ship CTD profiles (Section 2.1). The colored squares represent the seasonal distribution of the data. The shaded area illustrates the seasonal variability in the model. This variability is amplified by ten times to compare observations and model output.

output and observations is significant. The model-inferred variability is at least ten times smaller than the non-seasonal variability in the fresh shelf region (shaded area represents ten times  $\Delta z_{\text{Max}}$  at PM and KN, Fig. 31) and negligible in the dense shelf region. Also, since significant variability in mWDW depth has been observed in front of the upstream part of the dense shelf region (Ryan et al., 2017), the abrupt dampening of the seasonality at the transition between the fresh shelf and dense shelf region appears unrealistic (at  $x=2000$  km, Fig. 30).

I identify four mechanisms that could explain the differences between model output and observations. First, the surface stress that forces the ocean circulation is averaged across the continental slope such that the amplitude of coastal downwelling might be underestimated. Second, the model does not account for the along-slope mixing, which is needed to represent the transition between the fresh shelf and dense shelf region. Indeed, in the model, the seasonal anomalies diffuse rapidly at the transition between the fresh shelf and dense shelf region because of the abrupt increase in cross-slope density gradient associated with the step function. Third, the model only considers baroclinic

anomalies' advection from the fresh to the dense shelf region, neglecting the propagation of baroclinic waves. Such wave could significantly amplify the amplitude of the oscillations (Spence et al., 2017). Finally, the model might overestimate the lateral diffusivity associated with eddies. Nonetheless, one cannot compare it with theoretical estimates (Isachsen, 2011) nor observations such that our results remain bounded by this unknown. In the end, even though our results suggest that the western Weddell Sea's continental shelves are less sensitive to seasonal variations in the surface forcings, direct measurements are needed in front of those continental shelves to confirm this mechanism.

#### 4.6.2 *Validity of the two-layer approximation*

This study's results are based on a two-layer representation of the dense shelf region, where the eddy overturning along the CS edge counteracts the transformation of AASW into dense shelf water. In reality, the mWDW layer outcrops on the CS, transforming into a third layer of High salinity shelf water (HSSW) through heat loss and brine rejection (Nicholls et al., 2004). Following the bathymetry, HSSW circulates inside the ice shelf cavities, undergo diabatic transformations and end up forming a dense water outflow of Weddell Sea Bottom Water (WSBW) that flows along the continental slope. In turn, the dense water outflow modulates the transport of mWDW towards the continental shelves (Morrison et al., 2020; Stewart and Thompson, 2016), closing the density overturning between mWDW and WSBW. Although not representing this overturning, the model reproduces the change in upper layer properties observed along the continental slope for a net density flux of  $6 \cdot 10^4 \pm 1 \cdot 10^4 \text{ kg s}^{-1}$  from the CS towards the BCS. Assuming this density flux to be exclusively driven by an inflow of mWDW ( $\rho'_2 = 1027.83 \text{ kg m}^{-3}$ ) towards the CS and compensated by an outflow of WSBW ( $\rho_3 = 1027.86 \text{ kg m}^{-3}$ ) towards the BCS implies a density overturning between mWDW and WSBW of  $F_{32'} = 2 \pm 0.4 \text{ Sv}^4$ . This estimate falls in the lower range of previous estimates (Jullion et al., 2014). For instance, the observation-based analysis of Huhn et al. (2008b) estimates a WSBW formation rate of  $5 \pm 1.7 \text{ Sv}$ , from which 1.1 Sv are formed in the Western Weddell Sea and 3.9 Sv in the southern Weddell Sea. Considering that only a portion of the WSBW remains on the continental shelf break, our

---

<sup>4</sup>  $F_{32'} = \int_{L_d} E_W^* dx / (\rho_3 - \rho'_2)$

estimate of  $2 \pm 0.4$  Sv appears realistic. However, the transformation rate of mWDW into WSBW depends on the difference in density between the water masses ( $Q^* = Q_{\text{tot}}/\Delta\rho$  in Sv). The larger the density difference between the layer is, the less efficient the transformation rate and inversely. Following the definition of Ryan et al. (2017), which consider a density of  $\rho'_2 = 1027.75 \text{ kg m}^{-3}$  for the mWDW layer, one can find a transformation rate of mWDW into WSBW of  $F_{32'} = 0.4 \pm 0.05$  Sv. This last estimate is not realistic because at least  $1.3 \pm 0.4$  Sv of WSBW is transported across the continental slope at the AP (Fahrbach et al., 2001). The sensitivity on  $\Delta\rho$  highlights the limit of our study: one needs to represent the outcrop of mWDW on the CS and model the density transfer associated with the third layer of WSBW to quantify the density overturning associated with the formation of bottom water.

At this stage, a three-layer formulation (Fig. 38, Appendix A.8) is complicated to set up because the processes controlling the bottom water export and the density transfer over retrograde slopes are unclear yet. Without theoretical knowledge on these mechanisms and, observations in the dense shelf region, the number of degrees of freedom in the system is expected to be too large for making a conclusive study. Nevertheless, a two-layer formulation is sufficient to estimate the net transport of volume transport needed to change the pycnocline height along the continental slope. In fact, it is reasonable to assume that there is no net cross-slope transport of volume associated with the overturning between mWDW and WSBW as the seawater's thermal expansion (0 cm, ref) is much smaller than the along-slope change in pycnocline height. Our simulations suggest that 75-90% of the along-slope change in pycnocline height are associated with the discharge of dense shelf water, whereas the dense water transport from the interior gyre to the BCS through eddy overturning controls 10-25% of the along-slope change in pycnocline height. As the Ekman overturning decreases between the fresh and the dense shelf region, eddies become more efficient in reducing the cross-slope density gradient (i.e. eddies transport dense/light water towards the BCS/IG). This result highlights that the along-slope decrease in surface stress accounts for a substantial part of the along-slope change in pycnocline height in the BCS. Several studies have shown that changes in the distribution in surface stress field and changes in water mass properties on the CS might impact the cross-slope exchange between the CS and the BCS (Hellmer et al., 2012; Naveira Garabato et al., 2019;

Stewart et al., 2019). Our analysis suggests that changes in surface stress in the fresh shelf region might also modulate the mWDW depth in the dense shelf region's. Further investigation is required to confirm this mechanism.

#### 4.7 SUMMARY

The flow of mWDW towards the Weddell Sea's continental shelves determines on-shelf transport of heat and therefore, the basal melting the ice shelf cavities and the transformation of mWDW into AABW, contributing to the lower cell of the meridional overturning circulation. Several studies have shown that the seasonal heaving of the pycnocline along the Weddell Sea's continental slope determines the flow of mWDW onto the southern Weddell Sea's continental shelves. The processes controlling the height of the pycnocline on the western Weddell Sea's continental is still an open question due to the sparsity of winter measurements. Using a conceptual model, I investigated the annual-mean and seasonal change in pycnocline height associated with the advection of baroclinic anomalies from the fresh to the dense shelf region.

The main finding of this study is the along-slope dampening of the seasonal anomalies advected from the fresh to the dense shelf region. The mechanisms driving this dampening are the decrease in flow strength associated with the widening of the continental slope, and the along-slope increase in lateral diffusivity associated with cross-slope density transport along the CS edge. Even though the formation of dense shelf water remains the main driver of along-slope changes in pycnocline height, the along-slope decrease in surface stress substantially contributes to the rise of the pycnocline along the continental slope. This finding suggests that the along-slope asymmetry in surface stress must be considered to predict the dense shelf region's mWDW depth.

There exist a few caveats to this study. For instance, the comparison between model output and observations suggests that the model overestimates the eddy diffusivity along the CS edge. However, the theoretical understanding of the eddy dynamic over retrograde slopes is still lacking. Also, the model does not represent the outcrop of modified Warm Deep Water on the CS continental shelves nor the bottom water outflow. Both mechanisms are essential for the cross-slope exchange of density between the CS and BCS. Direct measurements are needed in the western Weddell Sea to quantify the density flux

on the CS and understand the eddy dynamic over retrograde slopes. Knowing these components would limit the system's degrees of freedom, providing a conceptual framework for understanding the BCS dynamic. More importantly, in situ data will allow quantifying the cross-slope exchange between CS and BCS water.



## CONCLUSION AND OUTLOOK

---

The Southern Ocean plays a significant role in controlling the meridional exchange of heat and biogeochemical properties, such as carbon, across the world ocean. One of its dominant features is the pan-Antarctic boundary current system, which flows westward around the Antarctic continent aside dense water formation regions. A central area where dense water forms is the Weddell Sea. There, the relatively warm water that is advected from lower latitude densifies and sinks, trapping heat into the deep ocean for several centuries. The Weddell Sea Boundary Current System (BCS) marks the boundary between the open ocean, where a vast pool of modified Warm Deep Water is found, and the continental shelves, where dense water forms. The cross-slope exchanges of oceanographic properties between the continental shelves and the open ocean drive the BCS densification along the continental slope. These exchanges modulate the seasonal inflow of relatively warm water towards the continental shelves and the export dense shelf waters advected by the BCS towards lower latitudes. So far, a coherent description of the BCS dynamic along the continental slope has been lacking. Also, how the along-slope densification of the BCS affects the seasonal variability along the continental slope has remained an open question. This Chapter provides specific answers to the research questions formulated in Chapter 1 and suggestions for future work.

- **Research question 1 (Chapter 3):** *How does the along-slope shift in density regime affect the seasonal variability in temperature and velocity along the continental slope? How do the seasonal variations in temperature and velocity relate to the variability in the large-scale wind-field?*

Oceanographic data confirmed that the along-slope densification of the BCS is accompanied by a reversal of the baroclinic shear between the fresh shelf and the dense shelf region. At the subsurface, the along-slope weakening of the cross-slope density gradient controls the barotropisation of the flow. At the bottom, the dense water outflow of WSBW determines the intensification of the flow strength within the dense shelf re-

gion. Despite the along-slope shift in flow regime, we found that a significant part of the seasonal variability remains barotropic. The barotropic flow accelerates in phase along the continental slope and accounts for more than 50% of the variability in the bottom water outflow. The barotropic flow's seasonal acceleration correlates with the wind variability on the eastern/north-eastern side of the gyre. Such finding suggests that upstream winds partly drive the seasonal variability in dense plume transport. However, the uncertainty on the surface stress is too significant to determine whether the Ekman transport or the Ekman pumping drives the barotropic flow's seasonal acceleration. Moored current meter data suggested a weakening of the seasonal variability in temperature and baroclinic velocity between the fresh and the dense shelf region. However, more data are needed to differentiate between the drivers of baroclinic fluctuations, especially within the dense shelf region.

- **Research question 2 (Chapter 4):** *What drives the baroclinic variability along the continental slope on seasonal time-scales ?*

I used a conceptual approach to investigate the baroclinic variability along the Weddell Sea's continental slope. The two-layer cartesian model developed for this purpose represents three key processes:

1. The along-slope decrease in coastal downwelling
2. The densification of the water masses, occurring on the wide continental shelves of the southwestern Weddell Sea.
3. The cross-slope exchange of water mass properties occurring in the pycnocline vicinity

Modelling analyses confirmed that the density input from the wide continental shelves is the first-order densification driver along the continental slope. Moreover, we found that the along-slope decrease in coastal downwelling substantially contributes to the pycnocline's rise between the fresh and the dense shelf region. The model output confirmed a significant dampening of the seasonal variability in pycnocline height in the dense shelf region. Part of the along-slope decrease in seasonal variability is explained by the reduction in flow strength associated with the widening of the continental slope in the dense shelf region. Such a decrease implies a weakening of the downstream advection of density anomalies.

Additionally, the density gradient between the continental shelf and BCS waters enhances the lateral diffusivity associated with eddies. In turn, they stabilise the flow, reducing the seasonal variability in the dense shelf region. The abrupt shift in seasonality between the fresh shelf and the dense shelf region found in the simulations appears unrealistic compared to observational studies. It suggests that seasonal dampening of the seasonality advected from the fresh shelf region is not valid in front of the southern continental shelves (Filchner-Ronne Ice Shelf) but probable in front of the western continental shelves (Larsen Ice Shelf). Yet, it is unclear where the transition occurs along the continental slope, and direct measurements are needed to confirm this mechanism. Also, the uncertainty of the eddy flux over retrograde slopes is too significant to quantify the cross-slope density exchange based on my methods.

- *Outlook*

In the end, this thesis provides useful insights on the mechanisms controlling the seasonality of the BCS along the continental slope. The teleconnection between bottom water transport and eastern Weddell Sea winds (red area, Fig. 32) suggests that the export of AABW is not solely determined by local processes but also by rapid changes in the large-scale wind field. Also, the dampening of the baroclinic seasonality along the continental slope (blue line, Fig. 32) suggests that the region in front of the western Weddell Sea continental shelves are little affected by the downstream advection of baroclinic signals. Thus, further research should focus on processes such as wave propagation, eddies, tides, etc ... to explain the baroclinic fluctuations. Following on these statements, I conclude this thesis by providing suggestions for future research :

1. The barotropic flow likely responds to the fast propagation of barotropic waves. However, the uncertainty on the surface stress is too large to directly relate wave propagation and surface forcing. I suggest using a regional model and performing sensitivity tests on the wind forcing to confirm the mechanism responsible for the barotropic flow's seasonal acceleration.
2. There exist a lack of overlapping data along the Weddell Sea's continental slope. Such overlap is necessary to monitor baroclinic waves'

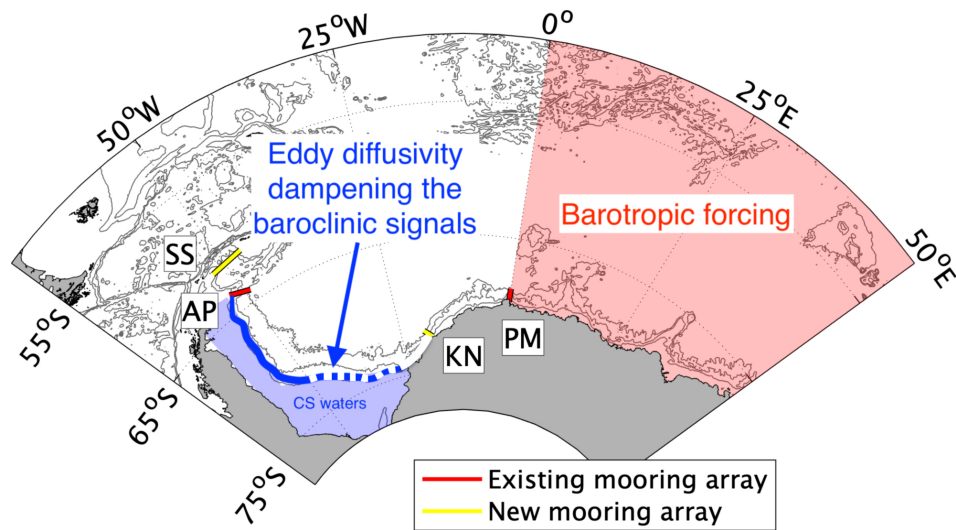


Figure 32: Map summarising the main findings, including the observational array suggested to monitor the along-slope propagation of the signals. The position at Kap Norvegia (KN) reproduces the SASSI array, which consisted in the deployment of moorings with high spatial resolution between 2009 and 2010 (Heywood et al., 2012). Scotia Sea, SS. Tip of the Antarctic Peninsula, AP. Continental shelves, CS. Prime Meridian, PM.

downstream propagation and link the seasonal acceleration of the flow with the dense water export towards lower latitudes. So far, the Alfred Wegner Institute regularly deployed mooring along the Prime Meridian (PM) and the Antarctic Peninsula's tip (AP). These arrays are essential to keep long-term monitoring in the Weddell Sea. International collaborations are needed to extend the observing system to Kapp Norvegia (KN), where the flow diverges due to topographic constraints, and the Scotia Sea (SS), where dense water is exported (new array, Fig. 32). Note that the ongoing EU project SO-CHIC already focuses on the relationship between dense water export at AP and SS.

3. Theoretical understanding of the density exchange associated with eddies along the CS edge is still lacking. Modelling studies are tackling this question, but in-situ data is needed to support the results. The COSMUS campaign of 2021 (Hellmer, 2020) targets the flow of mWDW towards the western continental shelves. The data collected during this campaign will help to understand the cross-slope density exchange associated with eddies. Such knowledge is needed to improve the parameterisation of ocean models and understand the relationship between mWDW inflow and bottom water export.

Answering these research questions will help understanding the meridional exchange of heat and biogeochemical properties between the Weddell Sea and the world ocean and, the cross-slope density exchange between the open ocean and the continental shelves. In turn, we will be able to better simulate the ocean circulation and better predict future changes in the Weddell Sea, such as the stability of the ice shelves. This knowledge could also be valid for other the dense shelf region around Antarctica such as the Ross Sea.



## ACKNOWLEDGMENTS

---

I want to express my gratitude to Olaf Boebel, Torsten Kanzow and Tore Hattermann for supervising me during this PhD. I thank Olaf for his unconditional encouragement, for allowing me to reach the Weddell Sea twice and for always supporting me, even when I was messing up with my flight tickets. I thank Torsten for trusting my scientific guts all along and finding time to guide me in a hectic schedule. I thank Tore for sharing his passion for science and for allowing me to visit Norway. Our discussions were very inspiring, and the reason why I enrolled in science at first sight. I would finally like to thank the three of you for giving me the privilege to discover the scientific world through expeditions, summer schools, conferences, and research stay abroad.

I want to thank each of the Physical Oceanography group members for sharing scientific knowledge and the excellent time we spent together. I thank Volker Strass and Ralph Timmermann, for their valuable scientific input during my PhD committee panels. Many thanks to Lukre, Janine and Svenja. You have been such good support to me!

I want to thank the Dokteam 2017-2018 for the great time we spent together. I would also like to thank the postgraduate school Polmar for their full support during my PhD and for funding my stay at the Norwegian Polar Institute (NPI). Following on those lines, I would also like to thank the NPI for their warm welcome.

I want to thank the Polarstern crew for their tremendous work. Feeling safe to sail on the ice is a privilege. A special big up also for the polarstern's penguins named Mortiz, Chachob, Sarah, Mathias, Maria, Margarita, Sandra, Diego and Elise. Being on an expedition with you has been fantastic :)

I want to thank my Bremerhaven family, Dami, Lenni, Raggi, Niels, Rémi, Alix, Jean-Louis, Diana, Vincent, Cora, Thomy, Natou. Few words are needed here, you know what you mean to me ;)

Pour finir je voudrais remercier Laura, Mathieu, Papa et Maman. Sans votre soutien je n'aurais jamais pu faire de thèse, ni faire ces voyages en Antarctique ... Mille fois merci !



## APPENDIX

## A.1 LIST OF AWI MOORINGS

mooring ID	Lon	Lat	year	water depth	n° of depths	record length
AWI103	-20.60	-72.56	1986-1986	3410 m	6	< 1 yr
AWI201	-19.60	-72.88	1987-1987	440 m	2	< 1 yr
AWI202	-8.29	-70.43	1987-1987	470 m	2	< 1 yr
AWI203	-11.76	-71.05	1989-1989	430 m	1	< 1 yr
AWI204	-11.96	-70.94	1989-1989	1520 m	2	< 1 yr
AWI205	-12.36	-70.71	1989-1989	2120 m	4	< 1 yr
AWI206	-52.00	-63.48	1989-2012	950 m	3	4 to 10 yrs
AWI207	-50.86	-63.73	1993-2016	2490 m	4	10 to 15 yrs
AWI208	-36.44	-65.62	1989-1995	4730 m	4	2 to 5 yrs
AWI209	-27.11	-66.61	1989-2008	4840 m	4	3 to 8 yrs
AWI210	-15.74	-69.65	1989-1992	4730 m	4	1 to 2 yrs
AWI211	-13.12	-70.49	1989-1992	2400 m	4	1 to 3 yrs
AWI212	-11.86	-70.97	1989-1993	1960 m	2	1 to 4 yrs
AWI213a	-20.79	-71.10	1990-1991	4440 m	2	1 yr
AWI213b	-26.11	-73.63	1991-1992	3360 m	3	≤ 1 yr
AWI215	-52.84	-63.33	1996-1998	460 m	2	2 yrs
AWI216	-49.09	-63.90	1990-2015	3490 m	3	2 to 9 yrs
AWI217	-45.86	-64.39	1990-2016	4420 m	4	2 to 10 yrs
AWI218	-42.49	-64.82	1990-1992	4650 m	3	1 to 2 yrs
AWI219	-37.71	-65.67	1990-1992	4730 m	2	1 yr
AWI220	-33.34	-65.97	1990-1991	4800 m	1	1 yr
AWI221	-30.30	-66.28	1990-1992	4750 m	4	1 to 2 yrs

AWI222	-24.87	-67.06	1990-1992	4840 m	2	1 to 2 yrs
AWI224	-17.91	-68.83	1990-1991	4740 m	1	< 1 yr
AWI225	-13.66	-70.32	1990-1992	4330 m	4	≤ 1 yr
AWI226	-13.54	-70.38	1990-1992	2900 m	3	1 yr
AWI227a	-3.19	-59.46	1994-1995	5060 m	5	< 1 yr
AWI227b	0.08	-59.07	1996-2008	4600 m	4	9 to 11 yrs
AWI229	-0.01	-63.94	1996-2016	5400 m	6	2 to 15 yrs
AWI230	0.05	-66.04	1996-2014	3500 m	4	10 to 16 yrs
AWI231	-0.02	-66.51	1996-2014	4500 m	4	10 to 13 yrs
AWI232	-0.08	-68.98	1996-2016	3350 m	4	8 to 18 yrs
AWI233	-0.27	-69.37	1996-2008	1940 m	3	4 to 11 yrs
AWI238	0.02	-54.28	1999-2008	1700 m	4	4 to 8 yrs
AWI239	0.01	-53.01	2001-2002	2470 m	5	2 yrs
AWI241	-0.00	-55.53	2005-2008	3610 m	4	3 yrs
AWI400	4.05	-57.63	1991-1992	4440 m	5	< 1 yr
BO	-3.29	-54.34	1990-1997	2710 m m	7	1 to 3 yrs
FR1	-31.76	-75.02	1995-1997	610 m	4	≤ 2 yrs
FR2	-33.56	-75.04	1995-1997	570 m	4	≤ 2 yrs
FR3	-49.02	-77.00	1995-1997	250 m	1	2 yrs
FR5	-58.73	-75.16	1995-1997	600 m	3	≤ 2 yrs
FR6	-60.81	-74.71	1995-1997	610 m	3	≤ 2 yrs
KG3	-57.92	-62.37	1985-1986	1990 m	2	< 1 yr
KN	-12.11	-71.11	1988-1989	660 m	3	< 1 yr
PF	5.89	-50.18	1986-1995	3800 m	7	≤ 2 yrs
WS	-2.56	-64.91	1987-1988	5050 m	5	< 1 yr

Table 2: AWI moorings deployed in the Weddell Sea between 1987 and 2017. Mooring in red have at least three instrument depths with velocity time-series longer than 3 years.

## A.2 DETAILS ON THE OPTIMAL INTERPOLATION (OI)

To perform the OI, the dataset is split into sub-datasets corresponding to sub-domains. Considering a vertically stratified ocean, the sub-datasets are selected within constant vertical depth-layers at PM and KN and terrain-following depth-layers at the tip of the AP. While the former coordinates provided better results in the vicinity of the thermocline depth, the latter proved to be more performant in mapping the dense bottom layer at the AP. The choice of the layer thickness is somehow arbitrary but a vertical resolution of 10 m (10-80 m) for the constant vertical (terrain-following) coordinates ensures to have a well-resolved interpolation grid and, include enough data to limit the error of the estimated field. The optimal interpolation is iteratively performed by depth-layers to produce map of temperature and salinity in the PPV-Z space. Points with an error larger than  $0.1^{\circ}\text{C}$  and  $0.02$  absolute salinity are discarded.

Temperature (T) and salinity (S) are determined at each interpolation grid point (g) from a linear weighted combination of valid observations selected around the interpolation depth,

$$T_g, S_g(\text{PPV}, Z_i) = \overline{T, S} + w \cdot [T, S - \overline{T, S}]. \quad (39)$$

$i$  is the depth index.  $\overline{T, S}$  is the averaged value of the sub-dataset, corresponding to the first guess. The interpolation is weighted such that, the larger the difference on PPV and/or the larger the uncertainty on the data points, the smaller the weights ( $w$ ).  $w$  are then defined as a function of, the PPV distance, the uncertainty associated to the instrument accuracy ( $\epsilon$ ) and, the uncertainty associated to the temporal variability of the measured field ( $\eta$ ),

$$w = C_{dg} \cdot [C_{dd} + I \cdot (\epsilon^2 + \eta^2)]^{-1}. \quad (40)$$

$I$  is the identity matrix. The PPV distances are enclosed in the data-grid ( $C_{dg}$ ) and data-data ( $C_{dd}$ ) covariance matrices. These matrices are filled with

values of covariance between two points (a,b) based on a Gaussian decay law which depends on the point to point PPV distance [Böhme *et al.*, 2005],

$$C_{ab}^2 = \langle s^2 \rangle \exp\left(-\frac{|\text{PPV}_a - \text{PPV}_b|^2}{\text{PPV}_a^2 + \text{PPV}_b^2}\right). \quad (41)$$

with  $\langle s^2 \rangle$  being the variance of the sub-dataset. It represents the variability to the mean state used to scale the covariance functions.  $\epsilon$  corresponds to  $1.10^{-3}$  °C and  $2.10^{-3}$  PSU for the CTD profiles, to  $2.10^{-3}$  °C and  $1.10^{-2}$  PSU for the float profiles and to  $2.10^{-2}$  °C and  $3.10^{-2}$  PSU for the seal profiles.  $\eta^2$  describes the variations between nearby data located within the same depth layer [Reeve *et al.*, 2016],

$$\eta^2 = \frac{1}{2N} \sum_{d=1}^N (x_d - x_n)^2 \quad (42)$$

$x_d$  are the data points,  $x_n$  are their closest neighbour and  $N$  is total the number of points in the sub-dataset.

### A.3 ERROR ASSOCIATED WITH THE VERTICAL INTERPOLATION

The uncertainty associated to the seasonal variations of the barotropic velocity ( $u_{bt}$ ) includes the error related to the calculation of the monthly mean ( $\sigma_{err}$ ) and, the error related to the vertical interpolation ( $\sigma_{pchip}$ ),

$$\sigma_{bt} = \sqrt{\frac{1}{I} \sum_{i=1}^I \sigma_{err}^2(i) + \sigma_{pchip}^2}, \quad (43)$$

$I$  being the number of multi year time series used to perform the depth-average. At each study location,  $\sigma_{pchip}$  is estimated from a set of realistic velocity profiles. This set includes all thermal-wind derived profiles estimated via objective mapping to represent a large range of realistic profiles. Each of them is normalized and velocities are interpolated between the current meter depths assuming a linear, spline or pchip interpolation method to model mooring profiles (Figure vertical interpolation). The difference between the depth-averaged velocity calculated from realistic and mooring profiles represents the uncertainty on  $u_{bt}$  associated to the vertical interpolation. This error

is quadratically averaged within the set of profiles to estimate a typical error of interpolation at the three study sites. The pchip proved to perform the best, giving an error of 2%, 1.4% and 8.7% of the shear at  $PM_1$ ,  $KN_2$  and  $AP_2$ , respectively. Then, this error is scaled depending both on the seasonal shear and the study location and, included in  $\sigma_{bt}$ . Note that the error associated to the baroclinic velocities ( $u_{bc} = u_i - u_{bt}$ ) corresponds to,

$$\sigma_{bc}(i) = \sqrt{\sigma_{err}^2(i) + \sigma_{bt}^2} \quad (44)$$

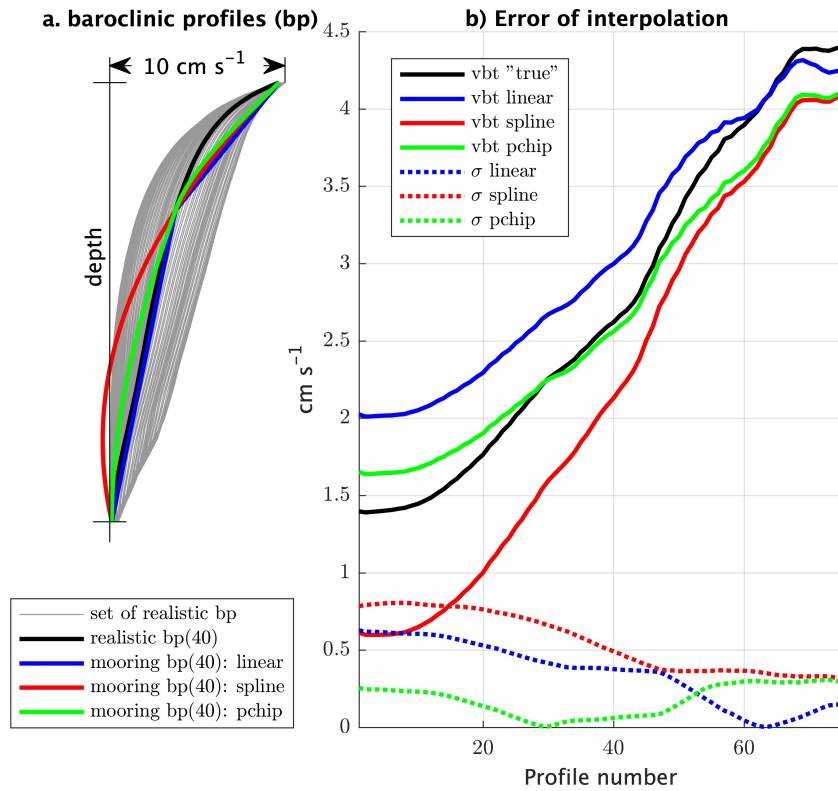


Figure 33: Comparison between four schemes of vertical interpolation used to estimate the error on the depth-averaged flow strength. a) Set of baroclinic profiles (bp) estimated at PM. Gray lines: realistic profiles. Black line: realistic profile number 40. Colored lines: mooring profiles estimated from the realistic profile number 40. b) Error of interpolation associated to each profile. Solid lines: baroclinic velocity depth-averaged ( $v_{bt}$ ). Dotted lines: difference between realistic bp and mooring bp.

## A.4 PHASE OF THE BAROTROPIC FLOW AT KN

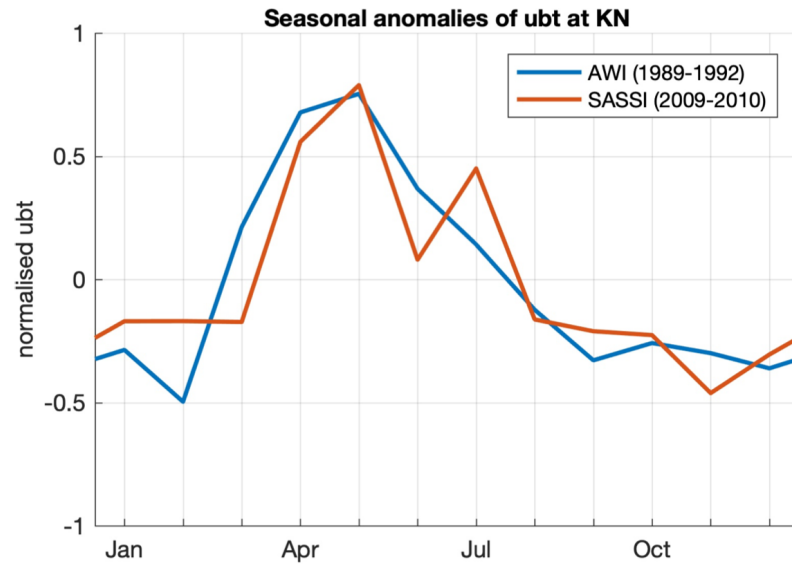


Figure 34: Phase of the barotropic flow (ubt) estimated over the 2500 isobath at Kapp Norvegia for different years from different mooring arrays. The AWI array has been deployed between 1989 and 1992 at  $13^{\circ}\text{W}$ . The SASSI array has been deployed between 2009 and 2010, 350 km downstream of the former array (Graham et al., 2013).

A.5 EOF ANALYSIS ON THE ZONAL STRESS

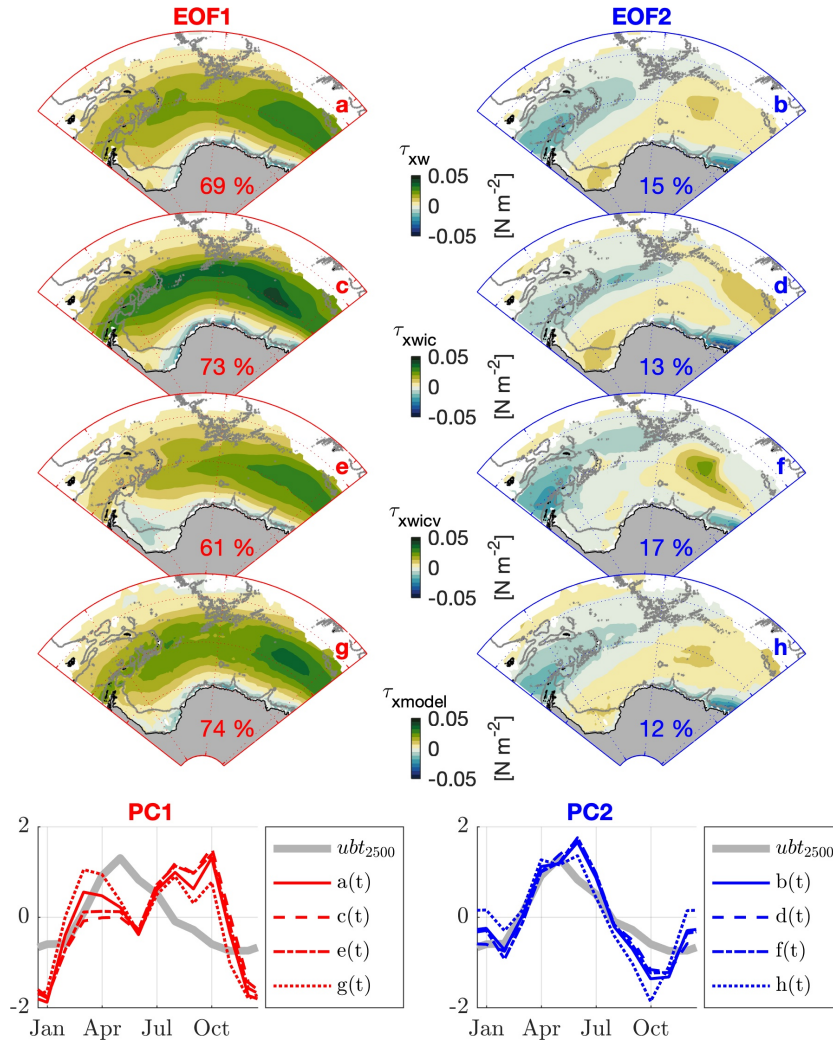


Figure 35: Comparison between the phase of the barotropic flow (ubt) estimated along the 2000-2500 m isobath and the two first modes of zonal stress. (a,b) Zonal stress estimated from  $\tau_w$ . (c,d) Zonal stress estimated from  $\tau_{wic}$ . (e,f) Zonal stress from  $\tau_{wicv}$ . (g,h) Zonal stress estimated from  $\tau_{model}$ . The percentage of variability explained by each mode is indicated. The bottom panels show the principal components of mode 1 and 2, from left to right. The definitions of  $\tau$  are given in the main manuscript in Section 2.3.

### A.6 TWO-MONTH-LAG-CORRELATION BETWEEN THE BAROTROPIC FLOW AND THE SURFACE STRESS

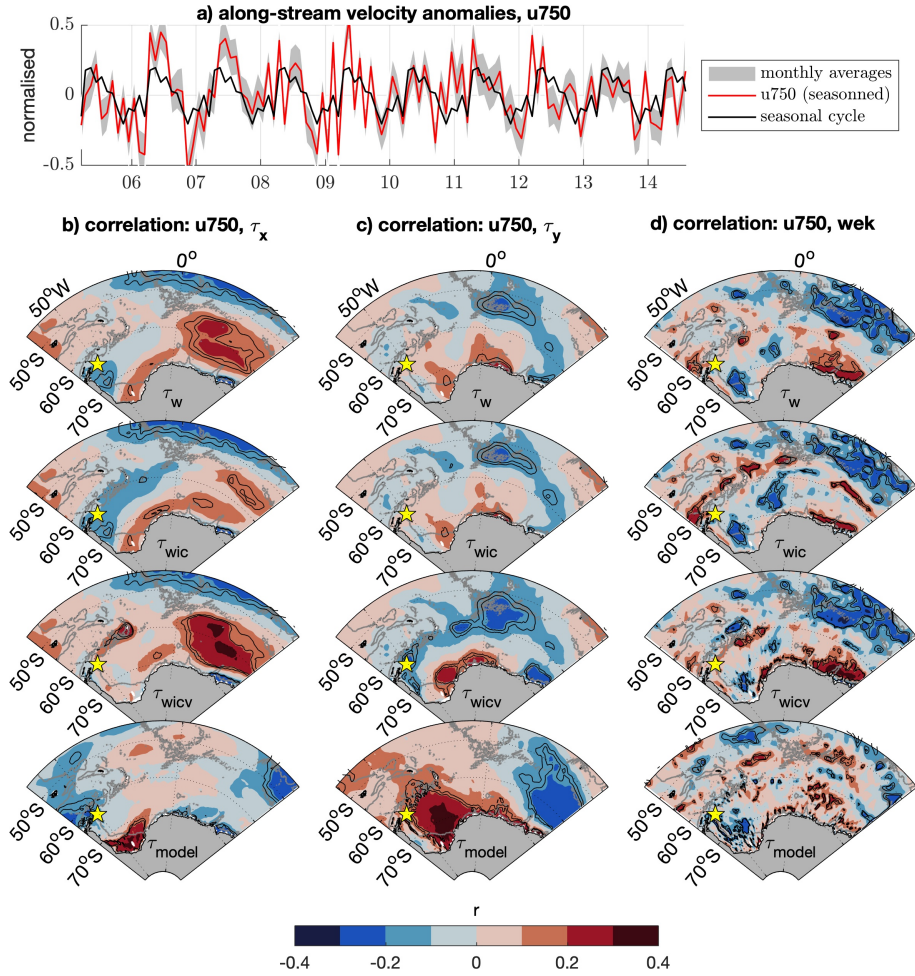


Figure 36: Two-months lag correlation between the monthly velocity observed between 2005 and 2015 at AP<sub>2500</sub> and the different components of surface stress. The velocity at 750 m is used as a proxy for the barotropic variations. The correlations maps are computed for four different estimates of surface stress,  $\tau_w$ ,  $\tau_{wic}$ ,  $\tau_{wicv}$  and  $\tau_{model}$ , which are defined in the main manuscript in Section 2.3. a) monthly velocity at 750 m depth. b,c and d) Correlation between u750 and the zonal stress, meridional stress and Ekman pumping, respectively. The star shows the position of AP<sub>2500</sub>. The black contours represent 90 and 95 % confidence interval.

A.7 OFF-SHELF SLOPE'S SLOPING

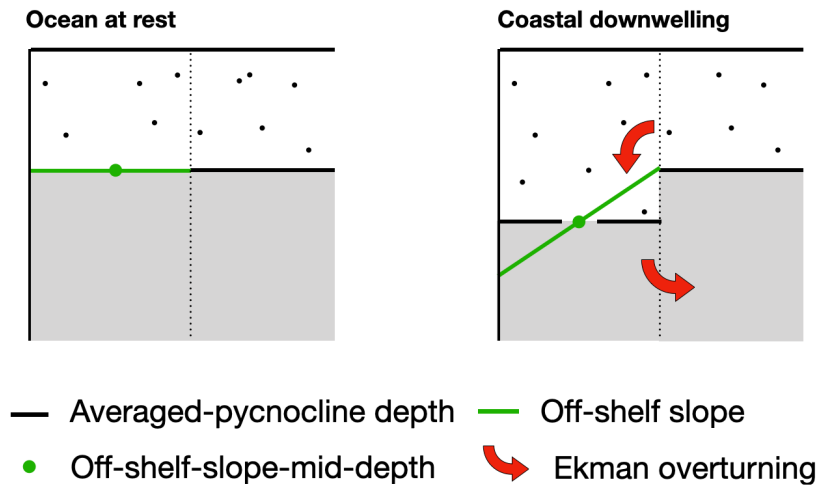


Figure 37: Schematic of the off-shelf-slope's sloping for an ocean at rest and for an ocean with coastal downwelling

A.8 FROM TWO-TO THREE LAYERS

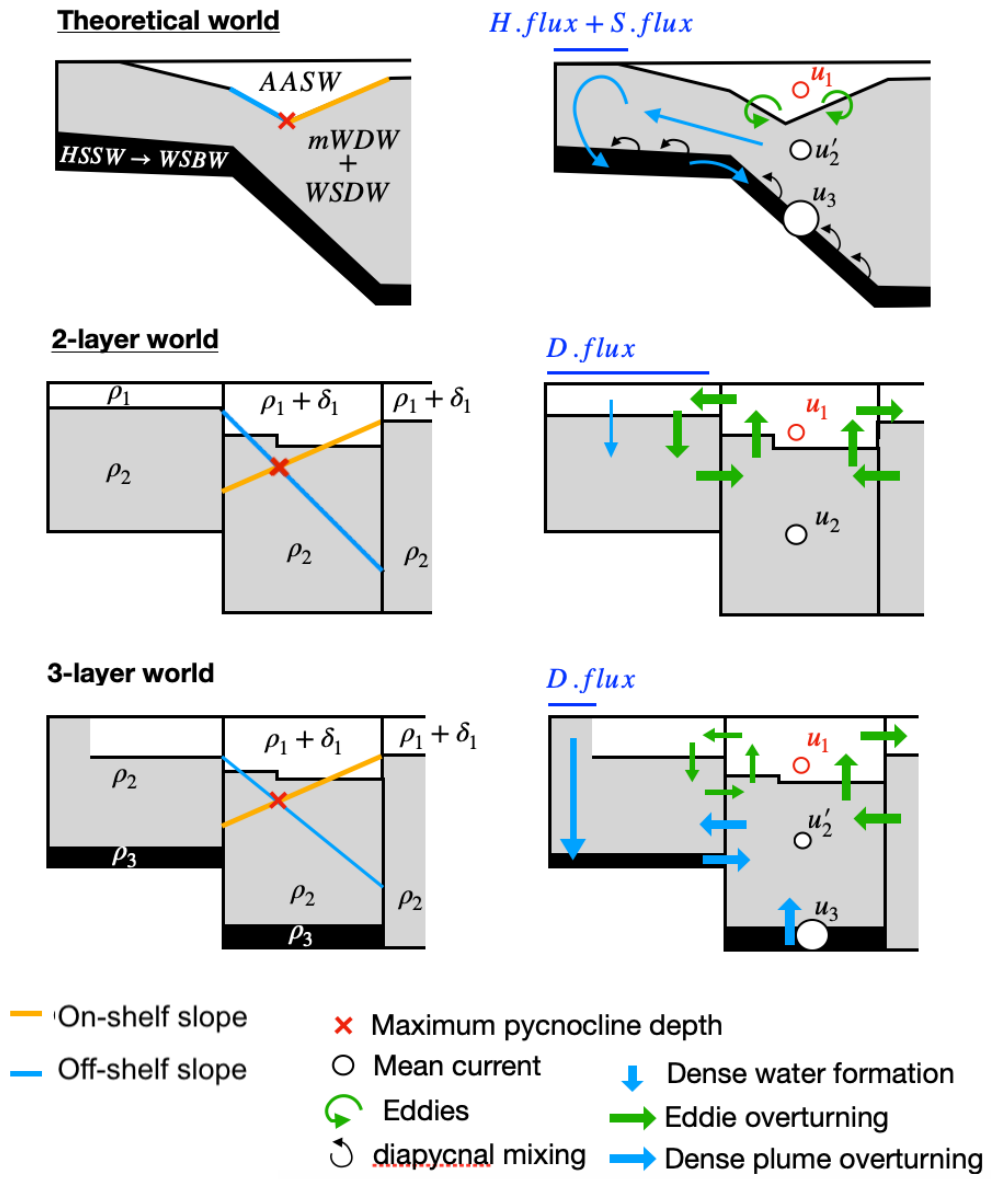


Figure 38: Schematic representing the water ocean stratification (left panels) and the processes controlling the cross-slope density transfer (right panels) in a theoretical, two-layer and three-layer world. The along-slope velocities averaged within the layers are represented by the black dots.

## BIBLIOGRAPHY

---

- Argo (2017). "Argo float data and metadata from Global Data Assembly Centre (Argo GDAC). SEANOE." In: URL: <https://doi.org/10.17882/42182>.
- Armitage, Thomas W. K., Ron Kwok, Andrew F. Thompson, and Glenn Cunningham (2018). "Dynamic Topography and Sea Level Anomalies of the Southern Ocean: Variability and Teleconnections." In: *Journal of Geophysical Research: Oceans* 123.1, pp. 613–630. DOI: [doi:10.1002/2017JC013534](https://doi.org/10.1002/2017JC013534). URL: <https://agupubs.onlinelibrary.wiley.com/doi/abs/10.1002/2017JC013534>.
- Böhme, Lars and Uwe Send (2005). "Objective analyses of hydrographic data for referencing profiling float salinities in highly variable environments." In: *Deep Sea Research Part II: Topical Studies in Oceanography* 52.3-4, pp. 651–664. ISSN: 09670645. DOI: [10.1016/j.dsr2.2004.12.014](https://doi.org/10.1016/j.dsr2.2004.12.014).
- Brink, K. H. and S. J. Lentz (2010a). "Buoyancy Arrest and Bottom Ekman Transport. Part I: Steady Flow." In: *Journal of Physical Oceanography* 40.4, pp. 621–635. DOI: [10.1175/2009jpo4266.1](https://doi.org/10.1175/2009jpo4266.1). URL: <http://journals.ametsoc.org/doi/abs/10.1175/2009JP04266.1>.
- Brink, K. H. and S. J. Lentz (2010b). "Buoyancy Arrest and Bottom Ekman Transport. Part II: Oscillating Flow." In: *Journal of Physical Oceanography* 40.4, pp. 636–655. DOI: [10.1175/2009jpo4267.1](https://doi.org/10.1175/2009jpo4267.1). URL: <http://journals.ametsoc.org/doi/abs/10.1175/2009JP04267.1>.
- Carmack, Eddy C. and Theodore D. Foster (1975). "On the flow of water out of the Weddell Sea." In: *Deep Sea Research and Oceanographic Abstracts* 22.11, pp. 711–724. ISSN: 0011-7471. DOI: [http://dx.doi.org/10.1016/0011-7471\(75\)90077-7](https://doi.org/10.1016/0011-7471(75)90077-7). URL: <http://www.sciencedirect.com/science/article/pii/0011747175900777>.
- Castagno, Pasquale, Vincenzo Capozzi, Giacomo R. DiTullio, Pierpaolo Falco, Giannetta Fusco, Stephen R. Rintoul, Giancarlo Spezie, and Giorgio Budillon (2019). "Rebound of shelf water salinity in the Ross Sea." In: *Nature Communications* 10.1, p. 5441. ISSN: 2041-1723. DOI: [10.1038/s41467-019-13083-8](https://doi.org/10.1038/s41467-019-13083-8). URL: <https://doi.org/10.1038/s41467-019-13083-8>.

- Cavaliere, D. J., C. L. Parkinson, P. Gloersen, and H. J. Zwally (1996). *Sea Ice Concentrations from Nimbus-7 SMMR and DMSP SSM/I-SSMIS Passive Microwave Data, Version 1*. Report. NASA National Snow and Ice Data Center Distributed Active Archive Center. DOI: <https://doi.org/10.5067/8GQ8LZQVL0VL>.
- Church, John A., Peter U. Clark, Anny Cazenave, Jonathan M. Gregory, Svetlana Jevrejeva, Anders Levermann, Mark A. Merrifield, Glenn A. Milne, R. Steven Nerem, Patrick D. Nunn, Antony J. Payne, W. Tad Pfeffer, Detlef Stammer, and Alakkat S. Unnikrishnan (2013). "Sea-Level Rise by 2100." In: *Science* 342.6165, pp. 1445–1445. DOI: [10.1126/science.342.6165.1445-a](https://doi.org/10.1126/science.342.6165.1445-a). URL: <https://science.sciencemag.org/content/sci/342/6165/1445.1.full.pdf>.
- Churchill, James H., Edward R. Levine, Donald N. Connors, and Peter C. Cornillon (1993). "Mixing of shelf, slope and Gulf Stream water over the continental slope of the Middle Atlantic Bight." In: *Deep Sea Research Part I: Oceanographic Research Papers* 40.5, pp. 1063–1085. ISSN: 0967-0637. DOI: [https://doi.org/10.1016/0967-0637\(93\)90090-P](https://doi.org/10.1016/0967-0637(93)90090-P). URL: <http://www.sciencedirect.com/science/article/pii/096706379390090P>.
- Cisewski, Boris, Volker H. Strass, and Harry Leach (2011). "Circulation and transport of water masses in the Lazarev Sea, Antarctica, during summer and winter 2006." In: *Deep Sea Research Part I: Oceanographic Research Papers* 58.2, pp. 186–199. ISSN: 0967-0637. DOI: <http://dx.doi.org/10.1016/j.dsr.2010.12.001>. URL: <http://www.sciencedirect.com/science/article/pii/S0967063710002402>.
- Cushman-Roisin, Benoit and Beckers Jean-Marie (2011). "Introduction to Geophysical Fluid Dynamics: Physical and Numerical Aspects." In: p. 789. ISBN: 978-0-12-088759-0.
- Daae, K., E. Darelus, I. Fer, S. Østerhus, and S. Ryan (2018). "Wind Stress Mediated Variability of the Filchner Trough Overflow, Weddell Sea." In: *Journal of Geophysical Research: Oceans* 123.5, pp. 3186–3203. ISSN: 2169-9275. DOI: [10.1002/2017jc013579](https://doi.org/10.1002/2017jc013579). URL: <https://agupubs.onlinelibrary.wiley.com/doi/abs/10.1002/2017JC013579>.
- Daae, K., I. Fer, and E. Darelus (2019). "Variability and Mixing of the Filchner Overflow Plume on the Continental Slope, Weddell Sea." In: *Journal of Physical Oceanography* 49.1, pp. 3–20. DOI: [10.1175/JPO-D-18-0093.1](https://doi.org/10.1175/JPO-D-18-0093.1). URL:

<https://journals.ametsoc.org/view/journals/phoc/49/1/jpo-d-18-0093.1.xml>.

- Daae, K., T. Hattermann, E. Darelius, and I. Fer (2017). "On the effect of topography and wind on warm water inflow—An idealized study of the southern Weddell Sea continental shelf system." In: *Journal of Geophysical Research: Oceans* 122.3, pp. 2622–2641. DOI: [doi:10.1002/2016JC012541](https://doi.org/10.1002/2016JC012541). URL: <https://agupubs.onlinelibrary.wiley.com/doi/abs/10.1002/2016JC012541>.
- Darelius, E., K. O. Strand, S. Østerhus, T. Gammeslrød, M. Årthun, and I. Fer (2014). "On the Seasonal Signal of the Filchner Overflow, Weddell Sea, Antarctica." In: *Journal of Physical Oceanography* 44.4, pp. 1230–1243. ISSN: 0022-3670. DOI: [10.1175/JPO-D-13-0180.1](https://doi.org/10.1175/JPO-D-13-0180.1). URL: <https://doi.org/10.1175/JPO-D-13-0180.1>.
- Dee, D. P. et al. (2011). "The ERA-Interim reanalysis: configuration and performance of the data assimilation system." In: *Quarterly Journal of the Royal Meteorological Society* 137.656, pp. 553–597. ISSN: 0035-9009. DOI: [10.1002/qj.828](https://doi.org/10.1002/qj.828). URL: <https://doi.org/10.1002/qj.828>.
- Dotto, Tiago S., Alberto Naveira Garabato, Sheldon Bacon, Michel Tsamados, Paul R. Holland, Jack Hooley, Eleanor Frajka-Williams, Andy Ridout, and Michael P. Meredith (2018). "Variability of the Ross Gyre, Southern Ocean: Drivers and Responses Revealed by Satellite Altimetry." In: *Geophysical Research Letters* 45.12, pp. 6195–6204. ISSN: 0094-8276. DOI: [10.1029/2018gl078607](https://doi.org/10.1029/2018gl078607). URL: <https://agupubs.onlinelibrary.wiley.com/doi/abs/10.1029/2018GL078607>.
- Driemel, A. et al. (2017). "From pole to pole: 33 years of physical oceanography onboard R/V Polarstern." In: *Earth Syst. Sci. Data* 9.1, pp. 211–220. ISSN: 1866-3516. DOI: [10.5194/essd-9-211-2017](https://doi.org/10.5194/essd-9-211-2017). URL: <http://www.earth-syst-sci-data.net/9/211/2017/>.
- Eayrs, Clare, David Holland, Diana Francis, Till Wagner, Rajesh Kumar, and Xichen Li (2019a). "Understanding the Seasonal Cycle of Antarctic Sea Ice Extent in the Context of Longer-Term Variability." In: *Reviews of Geophysics* 57, pp. 1037–1064. DOI: [10.1029/2018RG000631](https://doi.org/10.1029/2018RG000631). URL: <https://agupubs.onlinelibrary.wiley.com/doi/abs/10.1029/2018RG000631>.
- Eayrs, Clare, David Holland, Diana Francis, Till Wagner, Rajesh Kumar, and Xichen Li (2019b). "Understanding the Seasonal Cycle of Antarctic Sea

- Ice Extent in the Context of Longer-Term Variability." In: *Reviews of Geophysics* 57.3, pp. 1037–1064. ISSN: 8755-1209. DOI: [10.1029/2018rg000631](https://doi.org/10.1029/2018rg000631). URL: <https://agupubs.onlinelibrary.wiley.com/doi/abs/10.1029/2018RG000631>.
- Ekman, V. (1905). "On the influence of the Earth's rotation on ocean-currents." In: *Ark. Mat. Astron. Fys.* 2, pp. 1–53.
- Emery, William J. and Richard E. Thomson (2001). "Chapter 3 - Statistical Methods and Error Handling." In: *Data Analysis Methods in Physical Oceanography*. Ed. by William J. Emery and Richard E. Thomson. Amsterdam: Elsevier Science, pp. 193–304. ISBN: 978-0-444-50756-3. DOI: <https://doi.org/10.1016/B978-044450756-3/50004-6>. URL: <http://www.sciencedirect.com/science/article/pii/B9780444507563500046>.
- Fahrbach, E., M. Hoppema, G. Rohardt, O. Boebel, O. Klatt, and A. Wisotzki (2011). "Warming of deep and abyssal water masses along the Greenwich meridian on decadal time scales: The Weddell gyre as a heat buffer." In: *Deep Sea Research Part II: Topical Studies in Oceanography* 58.25–26, pp. 2509–2523. ISSN: 0967-0645. DOI: <http://dx.doi.org/10.1016/j.dsr2.2011.06.007>. URL: <http://www.sciencedirect.com/science/article/pii/S0967064511001809>.
- Fahrbach, E., G. Rohardt, and G. Krause (1992). "The Antarctic Coastal Current in the southeastern Weddell Sea." In: *Weddell Sea Ecology: Results of EPOS European "Polarstern" Study*. Ed. by Gotthilf Hempel. Berlin, Heidelberg: Springer Berlin Heidelberg, pp. 171–182. ISBN: 978-3-642-77595-6. DOI: [10.1007/978-3-642-77595-6\\_19](http://dx.doi.org/10.1007/978-3-642-77595-6_19). URL: [http://dx.doi.org/10.1007/978-3-642-77595-6\\_19](http://dx.doi.org/10.1007/978-3-642-77595-6_19).
- Fahrbach, E., G. Rohardt, M. Schröder, and V. Strass (1994). "Transport and structure of the Weddell Gyre." In: *Annales Geophysicae* 12.9, pp. 840–855. ISSN: 1432-0576. DOI: [10.1007/s00585-994-0840-7](http://dx.doi.org/10.1007/s00585-994-0840-7). URL: <http://dx.doi.org/10.1007/s00585-994-0840-7>.
- Fahrbach, Eberhard, Sabine Harms, Gerd Rohardt, Michael Schröder, and Rebecca A. Woodgate (2001). "Flow of bottom water in the northwestern Weddell Sea." In: *Journal of Geophysical Research: Oceans* 106.C2, pp. 2761–2778. ISSN: 0148-0227. DOI: [10.1029/2000jc900142](https://doi.org/10.1029/2000jc900142). URL: <https://agupubs.onlinelibrary.wiley.com/doi/abs/10.1029/2000JC900142>.

- Foldvik, A., T. Gammelsrød, S. Østerhus, E. Fahrbach, G. Rohardt, M. Schröder, K. W. Nicholls, L. Padman, and R. A. Woodgate (2004). "Ice shelf water overflow and bottom water formation in the southern Weddell Sea." In: *Journal of Geophysical Research: Oceans* 109.C2, n/a–n/a. ISSN: 2156-2202. DOI: [10.1029/2003JC002008](https://doi.org/10.1029/2003JC002008). URL: <http://dx.doi.org/10.1029/2003JC002008>.
- Foster, Theodore D. and Eddy C. Carmack (1976). "Frontal zone mixing and Antarctic Bottom water formation in the southern Weddell Sea." In: *Deep Sea Research and Oceanographic Abstracts* 23.4, pp. 301–317. ISSN: 0011-7471. DOI: [http://dx.doi.org/10.1016/0011-7471\(76\)90872-X](http://dx.doi.org/10.1016/0011-7471(76)90872-X). URL: <http://www.sciencedirect.com/science/article/pii/001174717690872X>.
- Gandin, L.S. (1965). *Objective Analysis of Meteorological Fields: GIMIZ, Gidrometeorologicheskoe Izdatelstvo, Leningrad 1963 : Transl. from the Russian*. Israel Program for scientific Translations. URL: <https://books.google.de/books?id=yux0nwEACAAJ>.
- Gill, A. E. (1973). "Circulation and bottom water production in the Weddell Sea." In: *Deep Sea Research and Oceanographic Abstracts* 20.2, pp. 111–140. ISSN: 0011-7471. DOI: [http://dx.doi.org/10.1016/0011-7471\(73\)90048-X](http://dx.doi.org/10.1016/0011-7471(73)90048-X). URL: <http://www.sciencedirect.com/science/article/pii/001174717390048X>.
- Gordon, Arnold L., Bruce Huber, Darren McKee, and Martin Visbeck (2010). "A seasonal cycle in the export of bottom water from the Weddell Sea." In: *Nature Geosci* 3.8, pp. 551–556. ISSN: 1752-0894. URL: <http://dx.doi.org/10.1038/ngeo916>.
- Gordon, Arnold L., Alejandro H. Orsi, Robin Muench, Bruce A. Huber, Enrico Zambianchi, and Martin Visbeck (2009). "Western Ross Sea continental slope gravity currents." In: *Deep Sea Research Part II: Topical Studies in Oceanography* 56.13–14, pp. 796–817. ISSN: 0967-0645. DOI: <http://dx.doi.org/10.1016/j.dsr2.2008.10.037>. URL: <http://www.sciencedirect.com/science/article/pii/S0967064508003603>.
- Graham, Jennifer A., Karen J. Heywood, Cédric P. Chavanne, and Paul R. Holland (2013). "Seasonal variability of water masses and transport on the Antarctic continental shelf and slope in the southeastern Weddell Sea." In: *Journal of Geophysical Research: Oceans* 118.4, pp. 2201–2214. ISSN: 2169-9291. DOI: [10.1002/jgrc.20174](https://doi.org/10.1002/jgrc.20174). URL: <http://dx.doi.org/10.1002/jgrc.20174>.

- Gregg, M.C., E.A. D'Asaro, J.J. Riley, and E. Kunze (2018). "Mixing Efficiency in the Ocean." In: *Annual Review of Marine Science* 10.1, pp. 443–473. DOI: [10.1146/annurev-marine-121916-063643](https://doi.org/10.1146/annurev-marine-121916-063643). URL: <https://www.annualreviews.org/doi/abs/10.1146/annurev-marine-121916-063643>.
- Hartmann, Dennis L. (2016). "Chapter 7 - The Ocean General Circulation and Climate." In: *Global Physical Climatology (Second Edition)*. Ed. by Dennis L. Hartmann. Boston: Elsevier, pp. 195–232. ISBN: 978-0-12-328531-7. DOI: <https://doi.org/10.1016/B978-0-12-328531-7.00007-4>. URL: <http://www.sciencedirect.com/science/article/pii/B9780123285317000074>.
- Hattermann, Tore (2018). "Antarctic Thermocline Dynamics along a Narrow Shelf with Easterly Winds." In: *Journal of Physical Oceanography* 48.10, pp. 2419–2443. DOI: [10.1175/jpo-d-18-0064.1](https://doi.org/10.1175/jpo-d-18-0064.1). URL: <https://journals.ametsoc.org/doi/abs/10.1175/JPO-D-18-0064.1>.
- Hellmer, Hartmut H., Frank Kauker, Ralph Timmermann, Jürgen Determann, and Jamie Rae (2012). "Twenty-first-century warming of a large Antarctic ice-shelf cavity by a redirected coastal current." In: *Nature* 485, p. 225. DOI: [10.1038/nature11064](https://doi.org/10.1038/nature11064)<https://www.nature.com/articles/nature11064#supplementary-information>. URL: <http://dx.doi.org/10.1038/nature11064>.
- Hellmer, Hartmut H., Frank Kauker, Ralph Timmermann, and Tore Hattermann (2017). "The Fate of the Southern Weddell Sea Continental Shelf in a Warming Climate." In: *Journal of Climate* 30.12, pp. 4337–4350. DOI: [10.1175/jcli-d-16-0420.1](https://doi.org/10.1175/jcli-d-16-0420.1). URL: <https://journals.ametsoc.org/doi/abs/10.1175/JCLI-D-16-0420.1>.
- Hellmer, Hartmut (2020). *Expedition Programme PS124, Expeditionsprogramm Polarstern, Bremerhaven, Alfred Wegener Institute for Polar and Marine Research*, 51 p. URL: <https://epic.awi.de/id/eprint/53220/>.
- Heywood, Karen, Ricardo A. Locarnini, Russell Frew, Paul Dennis, and Brian A. King (1998). *Transport and water masses of the Antarctic Slope Front system in the eastern Weddell Sea*. Vol. 75, pp. 203–214. DOI: [10.1029/AR075p0203](https://doi.org/10.1029/AR075p0203).
- Heywood, Karen, R. Muench, and G. Williams (2012). *An Overview of the Synoptic Antarctic Shelf-Slope Interactions (SASSI) project for the International Polar Year*. Vol. 8, pp. 1117–1122. DOI: [10.5194/os-8-1117-2012](https://doi.org/10.5194/os-8-1117-2012).
- Hogg, Nelson G. and William E. Johns (1995). "Western boundary currents." In: *Reviews of Geophysics* 33.S2, pp. 1311–1334. ISSN: 8755-1209. DOI: [10.1029/1995RG000131](https://doi.org/10.1029/1995RG000131).

1029/95rg00491. URL: <https://agupubs.onlinelibrary.wiley.com/doi/abs/10.1029/95RG00491>.

- Holland, David M. (2013). "Chapter 16 - The Marine Cryosphere." In: *International Geophysics*. Ed. by Gerold Siedler, Stephen M. Griffies, John Gould, and John A. Church. Vol. 103. Academic Press, pp. 413–442. ISBN: 0074-6142. DOI: <https://doi.org/10.1016/B978-0-12-391851-2.00016-7>. URL: <http://www.sciencedirect.com/science/article/pii/B9780123918512000167>.
- Hughes, Chris W and Michael P Meredith (2006). "Coherent sea-level fluctuations along the global continental slope." In: *Philosophical Transactions of the Royal Society A: Mathematical, Physical and Engineering Sciences* 364.1841, pp. 885–901. DOI: [doi:10.1098/rsta.2006.1744](https://doi.org/10.1098/rsta.2006.1744). URL: <https://royalsocietypublishing.org/doi/abs/10.1098/rsta.2006.1744>.
- Huhn, Oliver, Tore Hattermann, Peter E. D. Davis, Erich Dunker, Hartmut H. Hellmer, Keith W. Nicholls, Svein Østerhus, Monika Rhein, Michael Schröder, and Jürgen Sültenfuß (2018). "Basal Melt and Freezing Rates From First Noble Gas Samples Beneath an Ice Shelf." In: *Geophysical Research Letters* 45.16, pp. 8455–8461. ISSN: 0094-8276. DOI: <https://doi.org/10.1029/2018GL079706>. URL: <https://agupubs.onlinelibrary.wiley.com/doi/abs/10.1029/2018GL079706>.
- Huhn, Oliver, Hartmut H. Hellmer, Monika Rhein, Christian Rodehacke, Wolfgang Roether, Michael P. Schodlok, and Michael Schröder (2008a). "Evidence of deep- and bottom-water formation in the western Weddell Sea." In: *Deep Sea Research Part II: Topical Studies in Oceanography* 55.8, pp. 1098–1116. ISSN: 0967-0645. DOI: <https://doi.org/10.1016/j.dsr2.2007.12.015>. URL: <http://www.sciencedirect.com/science/article/pii/S0967064508000489>.
- Huhn, Oliver, Hartmut H. Hellmer, Monika Rhein, Christian Rodehacke, Wolfgang Roether, Michael P. Schodlok, and Michael Schröder (2008b). "Evidence of deep- and bottom-water formation in the western Weddell Sea." In: *Deep Sea Research Part II: Topical Studies in Oceanography* 55.8, pp. 1098–1116. ISSN: 0967-0645. DOI: <https://doi.org/10.1016/j.dsr2.2007.12.015>. URL: <http://www.sciencedirect.com/science/article/pii/S0967064508000489>.

- Huhn, Oliver, Monika Rhein, Mario Hoppema, and Steven van Heuven (2013). "Decline of deep and bottom water ventilation and slowing down of anthropogenic carbon storage in the Weddell Sea, 1984–2011." In: *Deep Sea Research Part I: Oceanographic Research Papers* 76, pp. 66–84. ISSN: 0967-0637. DOI: <https://doi.org/10.1016/j.dsr.2013.01.005>. URL: <https://www.sciencedirect.com/science/article/pii/S0967063713000253>.
- Isachsen, Pål E., J. H. LaCasce, C. Mauritzen, and S. Häkkinen (2003). "Wind-Driven Variability of the Large-Scale Recirculating Flow in the Nordic Seas and Arctic Ocean." In: *Journal of Physical Oceanography* 33.12, pp. 2534–2550. DOI: [10.1175/1520-0485\(2003\)033<2534:wvotlr>2.0.co;2](https://doi.org/10.1175/1520-0485(2003)033<2534:wvotlr>2.0.co;2). URL: <https://journals.ametsoc.org/doi/abs/10.1175/1520-0485%282003%29033%3C2534%3AWVOTLR%3E2.0.CO%3B2>.
- Isachsen, Pål Erik (2011). "Baroclinic instability and eddy tracer transport across sloping bottom topography: How well does a modified Eady model do in primitive equation simulations?" In: *Ocean Modelling* 39.1, pp. 183–199. ISSN: 1463-5003. DOI: <https://doi.org/10.1016/j.ocemod.2010.09.007>. URL: <http://www.sciencedirect.com/science/article/pii/S1463500310001460>.
- Jacobs, Stanley S., Anthony F. Amos, and Peter M. Bruchhausen (1970a). "Ross sea oceanography and antarctic bottom water formation." In: *Deep Sea Research and Oceanographic Abstracts* 17.6, pp. 935–962. ISSN: 0011-7471. DOI: [https://doi.org/10.1016/0011-7471\(70\)90046-X](https://doi.org/10.1016/0011-7471(70)90046-X). URL: <http://www.sciencedirect.com/science/article/pii/001174717090046X>.
- Jacobs, Stanley S., Anthony F. Amos, and Peter M. Bruchhausen (1970b). "Ross sea oceanography and antarctic bottom water formation." In: *Deep Sea Research and Oceanographic Abstracts* 17.6, pp. 935–962. ISSN: 0011-7471. DOI: [https://doi.org/10.1016/0011-7471\(70\)90046-X](https://doi.org/10.1016/0011-7471(70)90046-X). URL: <http://www.sciencedirect.com/science/article/pii/001174717090046X>.
- Jullion, Loïc, Alberto C. Naveira Garabato, Sheldon Bacon, Michael P. Meredith, Pete J. Brown, Sinhue Torres-Valdés, Kevin G. Speer, Paul R. Holland, Jun Dong, Dorothée Bakker, Mario Hoppema, Brice Loose, Hugh J. Venables, William J. Jenkins, Marie-José Messias, and Eberhard Fahrbach (2014). "The contribution of the Weddell Gyre to the lower limb of the Global Overturning Circulation." In: *Journal of Geophysical Research: Oceans* 119.6, pp. 3357–3377. ISSN: 2169-9291. DOI: [10.1002/2013JC009725](https://doi.org/10.1002/2013JC009725). URL: <http://dx.doi.org/10.1002/2013JC009725>.

- Klatt, Olaf, Olaf Boebel, and Eberhard Fahrback (2007). "A Profiling Float's Sense of Ice." In: *Journal of Atmospheric and Oceanic Technology* 24.7, pp. 1301–1308. DOI: [10.1175/jtech2026.1](https://doi.org/10.1175/jtech2026.1). URL: <http://journals.ametsoc.org/doi/abs/10.1175/JTECH2026.1>.
- Kottmeier, C., K. Frey, M. Hasel, and O. Eisen (2003). "Sea ice growth in the eastern Weddell Sea in winter." In: *Journal of Geophysical Research: Oceans* 108.C4, n/a–n/a. ISSN: 2156-2202. DOI: [10.1029/2001JC001087](https://doi.org/10.1029/2001JC001087). URL: <http://dx.doi.org/10.1029/2001JC001087>.
- Le Paih, Nicolas, Tore Hattermann, Olaf Boebel, Torsten Kanzow, Christof Lüpkes, Gerd Rohardt, Volker Strass, and Steven Herbette (2020). "Coherent Seasonal Acceleration of the Weddell Sea Boundary Current System Driven by Upstream Winds." In: *Journal of Geophysical Research: Oceans* 125.10, e2020JC016316. ISSN: 2169-9275. DOI: <https://doi.org/10.1029/2020JC016316>. URL: <https://doi.org/10.1029/2020JC016316>.
- Leach, Harry, Volker Strass, and Boris Cisewski (2011). "Modification by lateral mixing of the Warm Deep Water entering the Weddell Sea in the Maud Rise region." In: *Ocean Dynamics* 61.1, pp. 51–68. ISSN: 1616-7228. DOI: [10.1007/s10236-010-0342-y](https://doi.org/10.1007/s10236-010-0342-y). URL: <http://dx.doi.org/10.1007/s10236-010-0342-y>.
- Lumpkin, Rick and Kevin Speer (2007). "Global Ocean Meridional Overturning." In: *Journal of Physical Oceanography* 37.10, pp. 2550–2562. DOI: [10.1175/jpo3130.1](https://doi.org/10.1175/jpo3130.1). URL: <http://journals.ametsoc.org/doi/abs/10.1175/JP03130.1>.
- Lüpkes, Christof and Vladimir M. Gryanik (2015). "A stability-dependent parametrization of transfer coefficients for momentum and heat over polar sea ice to be used in climate models." In: *Journal of Geophysical Research: Atmospheres* 120.2, pp. 552–581. ISSN: 2169-8996. DOI: [10.1002/2014JD022418](https://doi.org/10.1002/2014JD022418). URL: <https://doi.org/10.1002/2014JD022418>.
- Lüpkes, Christof, Vladimir M. Gryanik, Jörg Hartmann, and Edgar L. Andreas (2012). "A parametrization, based on sea ice morphology, of the neutral atmospheric drag coefficients for weather prediction and climate models." In: *Journal of Geophysical Research: Atmospheres* 117.D13. ISSN: 0148-0227. DOI: [10.1029/2012jd017630](https://doi.org/10.1029/2012jd017630). URL: <https://agupubs.onlinelibrary.wiley.com/doi/abs/10.1029/2012JD017630>.

- Marshall, John and Kevin Speer (2012). "Closure of the meridional overturning circulation through Southern Ocean upwelling." In: *Nature Geoscience* 5.3, pp. 171–180. ISSN: 1752-0908. DOI: [10.1038/ngeo1391](https://doi.org/10.1038/ngeo1391). URL: <https://doi.org/10.1038/ngeo1391>.
- Meijers, A. J. S., M. P. Meredith, E. P. Abrahamson, M. A. Morales Maqueda, D. C. Jones, and A. C. Naveira Garabato (2016). "Wind-driven export of Weddell Sea slope water." In: *Journal of Geophysical Research: Oceans* 121.10, pp. 7530–7546. ISSN: 2169-9291. DOI: [10.1002/2016JC011757](http://dx.doi.org/10.1002/2016JC011757). URL: <http://dx.doi.org/10.1002/2016JC011757>.
- Meredith, Michael P., Arnold L. Gordon, Alberto C. Naveira Garabato, E. Povl Abrahamson, Bruce A. Huber, Loïc Jullion, and Hugh J. Venables (2011). "Synchronous intensification and warming of Antarctic Bottom Water outflow from the Weddell Gyre." In: *Geophysical Research Letters* 38.3, n/a–n/a. ISSN: 1944-8007. DOI: [10.1029/2010GL046265](http://dx.doi.org/10.1029/2010GL046265). URL: <http://dx.doi.org/10.1029/2010GL046265>.
- Meredith, Michael P., Ricardo A. Locarnini, Kim A. Van Scoy, Andrew J. Watson, Karen J. Heywood, and Brian A. King (2000). "On the sources of Weddell Gyre Antarctic Bottom Water." In: *Journal of Geophysical Research: Oceans* 105.C1, pp. 1093–1104. ISSN: 2156-2202. DOI: [10.1029/1999JC900263](http://dx.doi.org/10.1029/1999JC900263). URL: <http://dx.doi.org/10.1029/1999JC900263>.
- Morrison, A. K., A. McC. Hogg, M. H. England, and P. Spence (2020). "Warm Circumpolar Deep Water transport toward Antarctica driven by local dense water export in canyons." In: *Science Advances* 6.18, eaav2516. DOI: [10.1126/sciadv.aav2516](https://advances.sciencemag.org/content/advances/6/18/eaav2516.full.pdf). URL: <https://advances.sciencemag.org/content/advances/6/18/eaav2516.full.pdf>.
- Mosby, H (1934). *The waters of the Atlantic Antarctic Ocean, in Scientific Results of the Norwegian Antarctic Expedition, 1927-1928*. Report.
- Munk, Walter H. (1950). "On the wind-driven ocean circulation." In: *Journal of Meteorology* 7.2, pp. 80–93. ISSN: 0095-9634. DOI: [10.1175/1520-0469\(1950\)007<0080:otwdoc>2.0.co;2](https://doi.org/10.1175/1520-0469(1950)007<0080:otwdoc>2.0.co;2). URL: [https://doi.org/10.1175/1520-0469\(1950\)007<0080:OTWDOC>2.0.CO;2](https://doi.org/10.1175/1520-0469(1950)007<0080:OTWDOC>2.0.CO;2).
- Naveira Garabato, A. C., T. S. Dotto, J. Hooley, S. Bacon, M. Tsamados, A. Ridout, E. E. Frajka-Williams, L. Herraiz-Borreguero, P. R. Holland, H. D. B. S. Heorton, and M. P. Meredith (2019). "Phased Response of the Subpolar Southern Ocean to Changes in Circumpolar Winds." In: *Geophys-*

- cal Research Letters* 46.11, pp. 6024–6033. ISSN: 0094-8276. DOI: [10.1029/2019gl082850](https://doi.org/10.1029/2019gl082850). URL: <https://agupubs.onlinelibrary.wiley.com/doi/abs/10.1029/2019GL082850>.
- Naveira Garabato, Alberto C., Elaine L. McDonagh, David P. Stevens, Karen J. Heywood, and Richard J. Sanders (2002). “On the export of Antarctic Bottom Water from the Weddell Sea.” In: *Deep Sea Research Part II: Topical Studies in Oceanography* 49.21, pp. 4715–4742. ISSN: 0967-0645. DOI: [http://dx.doi.org/10.1016/S0967-0645\(02\)00156-X](http://dx.doi.org/10.1016/S0967-0645(02)00156-X). URL: <http://www.sciencedirect.com/science/article/pii/S096706450200156X>.
- Nicholls, K. W., C. J. Pudsey, and P. Morris (2004). “Summertime water masses off the northern Larsen C Ice Shelf, Antarctica.” In: *Geophysical Research Letters* 31.9. ISSN: 0094-8276. DOI: [10.1029/2004gl019924](https://doi.org/10.1029/2004gl019924). URL: <https://agupubs.onlinelibrary.wiley.com/doi/abs/10.1029/2004GL019924>.
- Nicholls, Keith W., Svein østerhus, Keith Makinson, Tor Gammelsrød, and Eberhard Fahrbach (2009). “Ice-ocean processes over the continental shelf of the southern Weddell Sea, Antarctica: A review.” In: *Reviews of Geophysics* 47.3. DOI: [doi:10.1029/2007RG000250](https://doi.org/10.1029/2007RG000250). URL: <https://agupubs.onlinelibrary.wiley.com/doi/abs/10.1029/2007RG000250>.
- Nøst, O. A., M. Biuw, V. Tverberg, C. Lydersen, T. Hattermann, Q. Zhou, L. H. Smedsrud, and K. M. Kovacs (2011). “Eddy overturning of the Antarctic Slope Front controls glacial melting in the Eastern Weddell Sea.” In: *Journal of Geophysical Research: Oceans* 116.C11, n/a–n/a. ISSN: 2156-2202. DOI: [10.1029/2011JC006965](http://dx.doi.org/10.1029/2011JC006965). URL: <http://dx.doi.org/10.1029/2011JC006965>.
- Orlanski, Isidoro and Michael D. Cox (1973). “Baroclinic instability in ocean currents.” In: *Geophysical Fluid Dynamics* 4.4, pp. 297–332. ISSN: 0016-7991. DOI: [10.1080/03091927208236102](https://doi.org/10.1080/03091927208236102). URL: <https://doi.org/10.1080/03091927208236102>.
- Orsi, A. H., G. C. Johnson, and J. L. Bullister (1999). “Circulation, mixing, and production of Antarctic Bottom Water.” In: *Progress in Oceanography* 43.1, pp. 55–109. ISSN: 0079-6611. DOI: [http://dx.doi.org/10.1016/S0079-6611\(99\)00004-X](http://dx.doi.org/10.1016/S0079-6611(99)00004-X). URL: <http://www.sciencedirect.com/science/article/pii/S007966119900004X>.
- Orsi, Alejandro H., Thomas Whitworth, and Worth D. Nowlin (1995). “On the meridional extent and fronts of the Antarctic Circumpolar Current.” In: *Deep Sea Research Part I: Oceanographic Research Papers* 42.5, pp. 641–

673. ISSN: 0967-0637. DOI: [http://dx.doi.org/10.1016/0967-0637\(95\)00021-W](http://dx.doi.org/10.1016/0967-0637(95)00021-W). URL: <http://www.sciencedirect.com/science/article/pii/S096706379500021W>.
- Park, Young-Hyang, Edwige Charriaud, Philippe Craneguy, and Annie Kartavtseff (2001). "Fronts, transport, and Weddell Gyre at 30°E between Africa and Antarctica." In: *Journal of Geophysical Research: Oceans* 106.C2, pp. 2857–2879. ISSN: 0148-0227. DOI: [10.1029/2000jc900087](https://doi.org/10.1029/2000jc900087). URL: <https://agupubs.onlinelibrary.wiley.com/doi/abs/10.1029/2000JC900087>.
- Paul, S., S. Willmes, and G. Heinemann (2015). "Long-term coastal-polynya dynamics in the southern Weddell Sea from MODIS thermal-infrared imagery." In: *The Cryosphere* 9.6, pp. 2027–2041. ISSN: 1994-0424. DOI: [10.5194/tc-9-2027-2015](https://doi.org/10.5194/tc-9-2027-2015). URL: <https://www.the-cryosphere.net/9/2027/2015/>.
- Pellichero, Violaine, Jean-Baptiste Sallée, Sunke Schmidtke, Fabien Roquet, and Jean-Benoît Charrassin (2017). "The ocean mixed layer under Southern Ocean sea-ice: Seasonal cycle and forcing." In: *Journal of Geophysical Research: Oceans* 122.2, pp. 1608–1633. DOI: [doi:10.1002/2016JC011970](https://doi.org/10.1002/2016JC011970). URL: <https://agupubs.onlinelibrary.wiley.com/doi/abs/10.1002/2016JC011970>.
- Reeve, K. A., O. Boebel, T. Kanzow, V. Strass, G. Rohardt, and E. Fahrbach (2016). "A gridded data set of upper-ocean hydrographic properties in the Weddell Gyre obtained by objective mapping of Argo float measurements." In: *Earth Syst. Sci. Data* 8.1, pp. 15–40. ISSN: 1866-3516. DOI: [10.5194/essd-8-15-2016](https://doi.org/10.5194/essd-8-15-2016). URL: <http://www.earth-syst-sci-data.net/8/15/2016/>.
- Reeve, Krissy Anne, Olaf Boebel, Volker Strass, Torsten Kanzow, and Rüdiger Gerdes (2019). "Horizontal circulation and volume transports in the Weddell Gyre derived from Argo float data." In: *Progress in Oceanography* 175, pp. 263–283. ISSN: 0079-6611. DOI: <https://doi.org/10.1016/j.pocean.2019.04.006>. URL: <http://www.sciencedirect.com/science/article/pii/S0079661117302756>.
- Riboni, Ismael Núñez and Eberhard Fahrbach (2009). "Seasonal variability of the Antarctic Coastal Current and its driving mechanisms in the Weddell Sea." In: *Deep Sea Research Part I: Oceanographic Research Papers* 56.11, pp. 1927–1941. ISSN: 0967-0637. DOI: <http://dx.doi.org/10.1016/j.dsr>.

- 2009.06.005. URL: <http://www.sciencedirect.com/science/article/pii/S0967063709001344>.
- Rignot, E., I. Velicogna, M. R. van den Broeke, A. Monaghan, and J. T. M. Lenaerts (2011). "Acceleration of the contribution of the Greenland and Antarctic ice sheets to sea level rise." In: *Geophysical Research Letters* 38.5. ISSN: 0094-8276. DOI: <https://doi.org/10.1029/2011GL046583>. URL: <https://agupubs.onlinelibrary.wiley.com/doi/abs/10.1029/2011GL046583>.
- Ryan, S., T. Hattermann, E. Darelius, and M. Schröder (2017). "Seasonal cycle of hydrography on the eastern shelf of the Filchner Trough, Weddell Sea, Antarctica." In: *Journal of Geophysical Research: Oceans* 122.8, pp. 6437–6453. DOI: [doi:10.1002/2017JC012916](https://doi.org/10.1002/2017JC012916). URL: <https://agupubs.onlinelibrary.wiley.com/doi/abs/10.1002/2017JC012916>.
- Ryan, S., M. Schröder, O. Huhn, and R. Timmermann (2016). "On the warm inflow at the eastern boundary of the Weddell Gyre." In: *Deep Sea Research Part I: Oceanographic Research Papers* 107, pp. 70–81. ISSN: 0967-0637. DOI: <https://doi.org/10.1016/j.dsr.2015.11.002>. URL: <http://www.sciencedirect.com/science/article/pii/S0967063715300315>.
- Spall, Michael A. (2004). "Boundary Currents and Watermass Transformation in Marginal Seas." In: *Journal of Physical Oceanography* 34.5, pp. 1197–1213. DOI: [10.1175/1520-0485\(2004\)034<1197:bcawti>2.0.co;2](https://doi.org/10.1175/1520-0485(2004)034<1197:bcawti>2.0.co;2). URL: <https://journals.ametsoc.org/doi/abs/10.1175/1520-0485%282004%29034%3C1197%3ABCAWTI%3E2.0.CO%3B2>.
- Spall, Michael A. and David C. Chapman (1998). "On the Efficiency of Baroclinic Eddy Heat Transport across Narrow Fronts." In: *Journal of Physical Oceanography* 28.11, pp. 2275–2287. DOI: [10.1175/1520-0485\(1998\)028<2275:oteobe>2.0.co;2](https://doi.org/10.1175/1520-0485(1998)028<2275:oteobe>2.0.co;2).
- Spence, Paul, Ryan M. Holmes, Andrew McC Hogg, Stephen M. Griffies, Kial D. Stewart, and Matthew H. England (2017). "Localized rapid warming of West Antarctic subsurface waters by remote winds." In: *Nature Climate Change* 7, p. 595. DOI: [10.1038/nclimate3335](https://doi.org/10.1038/nclimate3335)<https://www.nature.com/articles/nclimate3335#supplementary-information>. URL: <https://doi.org/10.1038/nclimate3335>.
- Stewart, Andrew L., Andreas Klocker, and Dimitris Menemenlis (2019). "Acceleration and Overturning of the Antarctic Slope Current by Winds, Eddies, and Tides." In: *Journal of Physical Oceanography* 49.8, pp. 2043–2074. DOI:

- 10.1175/jpo-d-18-0221.1. URL: <https://journals.ametsoc.org/doi/abs/10.1175/JPO-D-18-0221.1>.
- Stewart, Andrew L. and Andrew F. Thompson (2015). "Eddy-mediated transport of warm Circumpolar Deep Water across the Antarctic Shelf Break." In: *Geophysical Research Letters* 42.2, pp. 432–440. ISSN: 0094-8276. DOI: 10.1002/2014gl062281. URL: <https://agupubs.onlinelibrary.wiley.com/doi/abs/10.1002/2014GL062281>.
- Stewart, Andrew L. and Andrew F. Thompson (2016). "Eddy Generation and Jet Formation via Dense Water Outflows across the Antarctic Continental Slope." In: *Journal of Physical Oceanography* 46.12, pp. 3729–3750. DOI: 10.1175/jpo-d-16-0145.1. URL: <http://journals.ametsoc.org/doi/abs/10.1175/JPO-D-16-0145.1>.
- Stommel, Henry (1948). "The westward intensification of wind-driven ocean currents." In: *Eos, Transactions American Geophysical Union* 29.2, pp. 202–206. ISSN: 0002-8606. DOI: 10.1029/TR029i002p00202. URL: <https://agupubs.onlinelibrary.wiley.com/doi/abs/10.1029/TR029i002p00202>.
- Straneo, Fiammetta (2006). "On the Connection between Dense Water Formation, Overturning, and Poleward Heat Transport in a Convective Basin." In: *Journal of Physical Oceanography* 36.9, pp. 1822–1840. DOI: 10.1175/jpo2932.1. URL: <https://journals.ametsoc.org/doi/abs/10.1175/JPO2932.1>.
- Su, Zhan, Andrew L. Stewart, and Andrew F. Thompson (2014). "An Idealized Model of Weddell Gyre Export Variability." In: *Journal of Physical Oceanography* 44.6, pp. 1671–1688. DOI: 10.1175/jpo-d-13-0263.1. URL: <http://journals.ametsoc.org/doi/abs/10.1175/JPO-D-13-0263.1>.
- Talley, Lynne D., George L. Pickard, William J. Emery, and James H. Swift (2011). *Descriptive physical oceanography: an introduction*. Amsterdam; Boston: Academic Press. ISBN: 9780750645522 0750645520.
- Tamura, Takeshi, Kay I. Ohshima, Alexander D. Fraser, and Guy D. Williams (2016). "Sea ice production variability in Antarctic coastal polynyas." In: *Journal of Geophysical Research: Oceans* 121.5, pp. 2967–2979. ISSN: 2169-9275. DOI: 10.1002/2015jc011537. URL: <https://agupubs.onlinelibrary.wiley.com/doi/abs/10.1002/2015JC011537>.
- Thompson, Andrew F. and Karen J. Heywood (2008). "Frontal structure and transport in the northwestern Weddell Sea." In: *Deep Sea Research Part I: Oceanographic Research Papers* 55.10, pp. 1229–1251. ISSN: 0967-0637. DOI:

- <https://doi.org/10.1016/j.dsr.2008.06.001>. URL: <http://www.sciencedirect.com/science/article/pii/S0967063708001222>.
- Thompson, Andrew F., Andrew L. Stewart, Paul Spence, and Karen J. Heywood (2018). "The Antarctic Slope Current in a Changing Climate." In: *Reviews of Geophysics* 56.4, pp. 741–770. DOI: [doi:10.1029/2018RG000624](https://doi.org/10.1029/2018RG000624). URL: <https://agupubs.onlinelibrary.wiley.com/doi/abs/10.1029/2018RG000624>.
- Timmermann, R., Q. Wang, and H. Hellmer (2012). "Ice-shelf basal melting in a global finite-element sea-ice/ice-shelf/ocean model." In: *Annals of Glaciology* 53.60, pp. 303–314. DOI: [10.3189/2012AoG60A156](https://doi.org/10.3189/2012AoG60A156).
- Timmermann, Ralph and Hartmut H. Hellmer (2013). "Southern Ocean warming and increased ice shelf basal melting in the twenty-first and twenty-second centuries based on coupled ice-ocean finite-element modelling." In: *Ocean Dynamics* 63.9, pp. 1011–1026. ISSN: 1616-7228. DOI: [10.1007/s10236-013-0642-0](https://doi.org/10.1007/s10236-013-0642-0). URL: <https://doi.org/10.1007/s10236-013-0642-0>.
- Todd, Robert E. et al. (2019). "Global Perspectives on Observing Ocean Boundary Current Systems." In: *Frontiers in Marine Science* 6.423. ISSN: 2296-7745. DOI: [10.3389/fmars.2019.00423](https://doi.org/10.3389/fmars.2019.00423). URL: <https://www.frontiersin.org/article/10.3389/fmars.2019.00423>.
- Treasure, Anne M. et al. (2017). "Marine Mammals Exploring the Oceans Pole to Pole: A Review of the MEOP Consortium." In: *Oceanography* 30, 132 – 138. DOI: <https://doi.org/10.5670/oceanog.2017.234>.
- Tschudi, M., W. N. Meier, J. S. Stewart, C. Fowler, and J. Maslanik (2019). "Polar Pathfinder Daily 25 km EASE-Grid Sea Ice Motion Vectors, Version 4. [1987–2016, 45–90°S, 65°E–65°W]. Boulder, Colorado USA. NASA National Snow and Ice Data Center Distributed Active Archive Center." In: DOI: <https://doi.org/10.5067/INAWUW07QH7B>.
- Vallis, Geoffrey K. (2017). *Atmospheric and Oceanic Fluid Dynamics: Fundamentals and Large-Scale Circulation*. 2nd ed. Cambridge: Cambridge University Press. ISBN: 9781107065505. DOI: [DOI:10.1017/9781107588417](https://doi.org/10.1017/9781107588417). URL: <https://www.cambridge.org/core/books/atmospheric-and-oceanic-fluid-dynamics/41379BDDC4257CBE11143C466F6428A4>.
- Van Caspel, Mathias (2016). *The importance of the western Weddell Sea to Weddell Sea Deep Water formation*.

- Vernet, M. et al. (2019). "The Weddell Gyre, Southern Ocean: Present Knowledge and Future Challenges." In: *Reviews of Geophysics* 57.3, pp. 623–708. ISSN: 8755-1209. DOI: [10.1029/2018rg000604](https://doi.org/10.1029/2018rg000604). URL: <https://agupubs.onlinelibrary.wiley.com/doi/abs/10.1029/2018RG000604>.
- Wang, Q., S. Danilov, E. Fahrback, J. Schröter, and T. Jung (2012). "On the impact of wind forcing on the seasonal variability of Weddell Sea Bottom Water transport." In: *Geophysical Research Letters* 39.6, n/a–n/a. ISSN: 1944-8007. DOI: [10.1029/2012GL051198](https://doi.org/10.1029/2012GL051198). URL: <http://dx.doi.org/10.1029/2012GL051198>.
- Whitworth T., III, A. H. Orsi, S.-J. Kim, W. D. Nowlin, and Jr. R. A. Locarnini (1985). "Water Masses and Mixing Near the Antarctic Slope Front." In: *Ocean, Ice, and Atmosphere: Interactions at the Antarctic Continental Margin*, pp. 1–27. DOI: [10.1029/AR075p0001](https://doi.org/10.1029/AR075p0001). URL: <https://agupubs.onlinelibrary.wiley.com/doi/abs/10.1029/AR075p0001>.
- Zhou, Q., T. Hattermann, O. A. Nøst, M. Biuw, K. M. Kovacs, and C. Lydersen (2014). "Wind-driven spreading of fresh surface water beneath ice shelves in the Eastern Weddell Sea." In: *Journal of Geophysical Research: Oceans* 119.6, pp. 3818–3833. ISSN: 2169-9291. DOI: [10.1002/2013JC009556](https://doi.org/10.1002/2013JC009556). URL: <http://dx.doi.org/10.1002/2013JC009556>.
- Årthun, Marius, Keith W. Nicholls, Keith Makinson, Michael A. Fedak, and Lars Boehme (2012). "Seasonal inflow of warm water onto the southern Weddell Sea continental shelf, Antarctica." In: *Geophysical Research Letters* 39.17, n/a–n/a. ISSN: 1944-8007. DOI: [10.1029/2012GL052856](https://doi.org/10.1029/2012GL052856). URL: <http://dx.doi.org/10.1029/2012GL052856>.

**D e c l a r a t i o n p u r s u a n t t o § 7 ( 2 )**

I herewith declare, that I

1. have formulated the thesis myself and without the help of others,
2. have not used sources and tools other than those indicated nor aids other than those permissible,
3. have marked the literal or textual taken part of the used works.

Date: \_\_\_\_\_

Signature: \_\_\_\_\_